

POLITECNICO DI TORINO

M.Sc. in Electronic Engineering

Master's Degree Thesis

**Numerical Investigation on Graphene Based
Mantle Cloaking of a PEC Cylinder**



Advisor:

Prof. Ladislau Matekovits

Candidate:

Carola Rizza

ACADEMIC YEAR 2018-2019

Contents

1	Introduction	2
1.1	Background and thesis aim	2
1.2	State of the art	2
1.3	Thesis outline	3
2	Theoretical introduction	5
2.1	Cloaking	5
2.2	Graphene	7
2.2.1	Surface conductivity	7
2.2.2	Surface impedance	9
2.2.3	Chemical potential tuning and limit values	16
2.2.4	Biasing of the graphene	16
3	Planar structure and Radar Cross Section	18
3.1	Preliminary simulations	18
3.2	Radar cross section definition and Maximum RCS computation	22
3.2.1	RCS computed on a point behind the cylinder	22
4	Simulation of the bare cylinder and of the different cloaked structures	27
4.1	Study of the bare cylinder behaviour	27
4.1.1	Computation of the Maximum Radar Cross Section	27
4.1.2	Electric field distribution in the normal plane to the cylinder	27
4.1.3	Study of the RCS computed using a probe behind the cylinder	27
4.2	Study to find the cloaking structure dimensions	36
4.2.1	Thickness of the dielectric	36
4.2.2	Width of the rectangular strips	36
4.3	Study of the behaviour of cloaked cylinder with rectangular strips	39
4.3.1	Computation of the Maximum Radar Cross Section	39
4.3.2	Electric field distribution in the normal plane to the cylinder	39
4.3.3	Study of the RCS computed using a probe behind the cylinder	39
4.4	Study of the behaviour of cloaked cylinder with modulated strips of maximum amplitude $1.5 \mu\text{m}$	49
4.4.1	Computation of the Maximum Radar Cross Section	49
4.4.2	Electric field distribution in the normal plane to the cylinder	49
4.4.3	Study of the RCS computed using a probe behind the cylinder	49
4.5	Study of the behaviour of cloaked cylinder with modulated strips of mean amplitude $1.5 \mu\text{m}$	54
4.5.1	Computation of the Maximum Radar Cross Section	54
4.5.2	Electric field distribution in the normal plane to the cylinder	54
4.5.3	Study of the RCS computed using a probe behind the cylinder	54
4.6	Study of the behaviour of cloaked cylinder with modulated strips of mean amplitude $1.5 \mu\text{m}$ and dielectric thickness $10.5 \mu\text{m}$	59
4.6.1	Computation of the Maximum Radar Cross Section	59
4.6.2	Electric field distribution in the normal plane to the cylinder	59
4.6.3	Study of the RCS computed using a probe behind the cylinder	59

5	Variations on the structure and settings of Section 4.6	64
5.1	Study of the behaviour of the structure of Section 4.6 varying the number of modulated strips	64
5.1.1	Case $\mu_c = 0$ eV	64
5.1.2	Case $\mu_c = 1$ eV	64
5.2	Study of the behaviour of the structure of Section 4.6 with different polarizations .	67
5.2.1	Polarization with electric field orthogonal to the cylinder	67
5.2.2	Polarization with oblique incidence	67
5.3	Study of the behaviour of the structure of Section 4.6 changing the material of the inner cylinder	71
5.3.1	Case of inner cylinder made of silver	71
5.3.2	Case of inner cylinder made by an external layer of graphene and, inside, vacuum	71
5.4	Study of the behaviour of the structure of Section 4.6 varying gradually the chemical potential in different strips	75
5.4.1	Case of starting $\mu_c = 0$ eV	75
5.4.2	Case of starting $\mu_c = 1$ eV	75

List of Figures

1.1	The figure shows an horn antenna with three cylinders. Since the cylinders are cloaked, they do not create perturbation of the electromagnetic waves radiated by the antenna [7].	4
1.2	Chinese fight aircrafts on which particular cloaking coats are tested in order to evade radars [4].	4
2.1	a) Impinging wave on an object covered by a structure (metamaterial) in order to avoid scattering [8]; b) waves pass around the object thanks to the use of the cloak [10].	6
2.2	Illustration of the plasmonic cloaking [9]. A spherical dielectric object with electric permittivity higher than the surrounding medium is covered by a dielectric shell with electric permittivity smaller than the surrounding medium. Choosing a particular value of the shell diameter, it is possible to obtain that the scattering of the object and of the shell cancel each other.	6
2.3	Real and imaginary part of the surface conductivity of graphene with respect to frequency, varying the chemical potential. Case computed with eq. (2.1).	10
2.4	Real and imaginary part of the surface conductivity of graphene with respect to frequency, varying the chemical potential. Case Kubo formula (eq. (2.3)).	11
2.5	Behaviour of the first integrand function dfe of the surface conductivity formula (eq. (2.1)).	12
2.6	Surface resistance and reactance of graphene computed from Kubo formula (eq (2.3)).	13
2.7	Surface resistance and reactance of graphene computed by CST.	14
2.8	Surface resistance and reactance of graphene computed by CST when the chemical potential μ_c is 0 eV.	15
2.9	Connection of a bias voltage to a structure done by a graphene layer, a substrate and the ground plane in order to change the chemical potential. In this figure, the ground plane is uneven in order to obtain different chemical potentials in different parts of the structure adopting the same voltage but changing the thickness of the substrate [18].	17
2.10	Illumination of <i>graphene</i> strips over a substrate with laser lights at different frequency.	17
3.1	Planar structure of 5 parallel microstrip lines simulated in CST.	19
3.2	Boundary conditions and background properties set for the simulation of the planar structure in CST.	19
3.3	Time domain solver parameters and mesh properties set for the simulation of the planar structure in CST.	20
3.4	S_{11} (top) and S_{31} (bottom) for the two structures with microstrips of different chemical potential for the graphene: chemical potential 0 (green) and chemical potential 1 (red).	21
3.5	Frequency settings for the simulation of the cylinder made of PEC in CST.	23
3.6	Boundary conditions and background properties set for the simulation of the cylinder made of PEC in CST.	24
3.7	Time domain solver parameters and plane wave settings for the simulation of the cylinder made of PEC in CST.	25
3.8	Mesh properties for the simulation of the vacuum cylinder in CST.	26
3.9	Probe settings in CST.	26

4.1	CST model of the illumination of a PEC cylinder	29
4.2	Frequency interval set for the simulation of the bare cylinder in CST.	29
4.3	Background settings for the simulation of the bare cylinder in CST.	30
4.4	Boundary conditions set for the simulation of the bare cylinder in CST.	30
4.5	Solver settings for the simulation of the bare cylinder in CST.	31
4.6	Mesh properties and cells statistics set for the simulation of the bare cylinder in CST.	32
4.7	Maximum RCS of the bare cylinder and its -3dB- shifted version.	33
4.8	Electric field in the plane normal to the cylinder, at 3THz.	33
4.9	Electric field in the plane normal to the cylinder in case of no obstacles, at f_0	34
4.10	Mesh properties and cells statistics set for the simulation of the case of the bare cylinder in CST.	34
4.11	RCS for the cylinder of PEC.	35
4.12	Maximum RCS for a cloaking structure with variable dielectric thickness h and rectangular strips of width $5 \mu\text{m}$	37
4.13	Maximum RCS for a cloaking structure with dielectric thickness $h = 5.56 \mu\text{m}$ and variable rectangular strips width.	38
4.14	Zoom around the minimum of the curves of Fig. 4.13.	38
4.15	Cloaked cylinder with a dielectric of $h = 5.56 \mu\text{m}$ and 14 rectangular strips.	40
4.16	Cloaked cylinder of Fig. 4.15 with underlined spacing of the strips.	40
4.17	Rectangular strips separated by a spacing δx where a capacity is generated.	41
4.18	Mesh properties and cells statistics set for the simulation of the cloaking structure of Fig. 4.15 in CST.	43
4.19	Maximum RCS for the cloaking structure with $h = 5.56 \mu\text{m}$ and rectangular strips $w = 1.5 \mu\text{m}$ varying the chemical potential μ_c	43
4.20	Electric field in the plane normal to the cloaked cylinder (with rectangular strips with $\mu_c = 0 \text{ eV}$), at 6.5 THz.	44
4.21	Electric field in the plane normal to the cloaked cylinder (with rectangular strips with $\mu_c = 1 \text{ eV}$), at 6.5 THz.	45
4.22	Electric field in the plane normal to the cloaked cylinder (with rectangular strips with $\mu_c = 0 \text{ eV}$), at 7 THz.	45
4.23	Electric field in the plane normal to the cloaked cylinder (with rectangular strips with $\mu_c = 1 \text{ eV}$), at 7 THz.	46
4.24	Electric field in the plane normal to the bare cylinder, at 6.5THz.	46
4.25	Electric field in the plane normal to the bare cylinder, at 7THz	47
4.26	RCS in case of the cloaked structure of Fig. 4.15 where all the strips are made of graphene with $\mu_c = 0 \text{ eV}$, compared to the RCS of the bare cylinder.	47
4.27	RCS in case of the cloaked structure of Fig. 4.15 where the strips are made of graphene with $\mu_c = 1 \text{ eV}$, compared to the RCS of the bare cylinder.	48
4.28	Cloaked cylinder with a dielectric of $h = 5.56 \mu\text{m}$ and 14 modulated strips with maximum amplitude $1.5 \mu\text{m}$	50
4.29	Mesh properties and cells statistics set for the simulation of the cloaking structure of Fig. 4.28 with $\mu_c = 0 \text{ eV}$ in CST.	50
4.30	Maximum RCS for the cloaking structure with $h = 5.56 \mu\text{m}$ and modulated strips with maximum amplitude $w = 1.5 \mu\text{m}$, varying the chemical potential μ_c	51
4.31	Electric field in the plane normal to the cloaked cylinder of Fig. 4.28 with $\mu_c = 0 \text{ eV}$, at 6.5 THz.	52
4.32	Electric field in the plane normal to the cloaked cylinder of Fig. 4.28 with $\mu_c = 1 \text{ eV}$, at 6.8 THz	52
4.33	RCS in case of the cloaked structure of Fig. 4.28 where the strips are made of graphene with $\mu_c = 0 \text{ eV}$, compared to the RCS of the bare cylinder.	53
4.34	RCS in case of the cloaked structure of Fig. 4.28 where the strip are made of graphene with $\mu_c = 1 \text{ eV}$, compared to the RCS of the bare cylinder.	53
4.35	Cloaked cylinder with a dielectric of $h = 5.56 \mu\text{m}$ and 14 modulated strips with mean amplitude $1.5 \mu\text{m}$	55
4.36	Mesh properties and cells statistics set for the simulation of the cloaking structure of Fig. 4.35 with any μ_c in CST.	55
4.37	Maximum RCS for the cloaking structure with $h = 5.56 \mu\text{m}$ and modulated strips with mean amplitude $w = 1.5 \mu\text{m}$, varying the chemical potential μ_c	56

4.38	Electric field in the plane normal to the cloaked cylinder of Fig. 4.35 with $\mu_c = 0$ eV, at 6.5 THz.	57
4.39	Electric field in the plane normal to the cloaked cylinder of Fig. 4.35 with $\mu_c = 1$ eV, at 7.2 THz	57
4.40	RCS in case of the cloaked structure of Fig. 4.35 where the strips have $\mu_c = 0$ eV, compared to the RCS of the bare cylinder.	58
4.41	RCS in case of the cloaked structure of Fig. 4.35 where the strips have $\mu_c = 1$ eV, compared to the RCS of the bare cylinder.	58
4.42	Cloaked cylinder with a dielectric of $h = 10.5 \mu\text{m}$ and 14 modulated strips with mean amplitude $1.5 \mu\text{m}$	60
4.43	Mesh properties and cells statistics set for the simulation of the cloaking structure of Fig. 4.42 with any μ_c in CST.	60
4.44	Maximum RCS for the cloaking structure with $h = 10.5 \mu\text{m}$ and modulated strips with mean amplitude $w = 1.5 \mu\text{m}$, varying the chemical potential μ_c	61
4.45	Electric field in the plane normal to the cloaked cylinder of Fig. 4.42 with $\mu_c = 0$ eV, at 3 THz.	62
4.46	Electric field in the plane normal to the cloaked cylinder of Fig. 4.42 with $\mu_c = 0.8$ eV, at 3.8 THz	62
4.47	RCS in case of the cloaked structure of Fig. 4.42 where the strips have $\mu_c = 0$ eV, compared to the RCS of the bare cylinder.	63
4.48	RCS in case of the cloaked structure of Fig. 4.42 where the strips have $\mu_c = 1$ eV, compared to the RCS of the bare cylinder.	63
5.1	Maximum RCS for the cloaking structure with $h = 10.5 \mu\text{m}$ and modulated strips with mean amplitude $w = 1.5 \mu\text{m}$ and $\mu_c = 0$ eV, varying the number of strips n	65
5.2	Variation of the Maximum RCS increasing the number of strips n , in case of $\mu_c = 0$ eV.	65
5.3	Maximum RCS for the cloaking structure with $h = 10.5 \mu\text{m}$ and modulated strips with mean amplitude $w = 1.5 \mu\text{m}$ and $\mu_c = 1$ eV, varying the number of strips n	66
5.4	Variation of the Maximum RCS increasing the number of strips n , in case of $\mu_c = 1$ eV.	66
5.5	Cloaked cylinder with a dielectric of $h = 10.5 \mu\text{m}$ and 14 modulated strips with mean amplitude $1.5 \mu\text{m}$. The plane wave has the magnetic field parallel to the object and the electric one orthogonal to it.	68
5.6	Maximum RCS for the structure and polarization of Fig. 5.5.	68
5.7	Cloaked cylinder with a dielectric of $h = 10.5 \mu\text{m}$ and 14 modulated strips with mean amplitude $1.5 \mu\text{m}$. The plane wave has a sloped direction with respect to the object.	69
5.8	X-component of the Maximum RCS for the structure and polarization of Fig. 5.7.	69
5.9	Y-component of the Maximum RCS for the structure and polarization of Fig. 5.7.	70
5.10	Z-component of the Maximum RCS for the structure and polarization of Fig. 5.7.	70
5.11	Cylinder made of silver, covered by the coat of Section 13.	72
5.12	Maximum RCS for the cloaking structure with $h = 10.5 \mu\text{m}$ and modulated strips with mean amplitude $w = 1.5 \mu\text{m}$ and $\mu_c = 0$ eV.	72
5.13	Electric field in the plane normal to the cloaked cylinder of Fig. 5.11 with $\mu_c = 0$ eV, at 3 THz	73
5.14	Cylinder made of vacuum and by an external layer of graphene with $\mu_c = 0$ eV, covered by the coat of Section 13.	73
5.15	Maximum RCS for the cloaking structure with $h = 10.5 \mu\text{m}$ and modulated strips with mean amplitude $w = 1.5 \mu\text{m}$ and $\mu_c = 0$ eV.	74
5.16	Electric field in the plane normal to the cloaked cylinder of Fig. 5.14 with $\mu_c = 0$ eV, at 3 THz	74
5.17	Maximum RCS for the structure of Section 4.6 where μ_c is varied progressively from 0 eV.	76
5.18	Electric field in the plane normal to the cloaked cylinder of Section 4.6 with progressing varying μ_c from 0 eV, at 3 THz.	76
5.19	Maximum RCS for the structure of Section 4.6 where μ_c is varied progressively from 1 eV.	77

5.20 Electric field in the plane normal to the cloaked cylinder of Section 4.6 with progressing varying μ_c from 1 eV, at 3.5 THz. 78

List of Tables

2.1	Table containing the electronic and mechanical properties of <i>graphene</i> [16].	8
4.1	Minimum frequencies and the bandwidths of the Maximum RCS curves of Fig. 4.19 changing the chemical potential μ_c	44
4.2	Minimum frequencies and the bandwidths of the Maximum RCS curves of Fig. 4.30 changing the chemical potential μ_c	51
4.3	Minimum frequencies and the bandwidths of the Maximum RCS curves of Fig. 4.37 changing the chemical potential μ_c	56
4.4	Table containing the minimum frequencies and the bandwidths of the Maximum RCS curves of Fig. 4.44 changing the chemical potential μ_c	61
5.1	Minimum frequencies and the bandwidths of the Maximum RCS curves of Fig. 5.17 according to the chemical potential μ_c	77
5.2	Minimum frequencies and the bandwidths of the Maximum RCS curves of Fig. 5.19 according to the chemical potential μ_c	77

Abstract

The *mantle cloaking* issue and its application in the Terahertz frequencies on a metallic cylinder is investigated. Graphene is adopted in order to reach the cloaking of the object, so an overview on this material and on its surface impedance is presented in the beginning. The cloaking coat for the cylinder is realized starting from a dielectric layer covering the object to hide, over which a certain number of modulated strips of graphene are laid. Several combinations of the values of the available parameters (chemical potential of graphene μ_c , dielectric constant ϵ , dielectric thickness h , number of modulated strips n and variation of width of each strip $w(z)$) are used in the simulations in order to find the best solution to cloak the cylinder. The most suitable cloak is adopted also for cylinders of different material in order to study the behaviour of the coat over different objects. Besides, the best cloaking solution obtained for the metallic cylinder illuminated by a linearly polarized field, and having the electric field orthogonal to the cylinder axis, is further used for the study of the behaviour for differently polarized incident fields on the same cylinder to observe the effect of the cloaking coat in case of diverse illumination conditions. Finally, starting from the coat with the best parameters for the cloaking of the considered object, the chemical potential μ_c is varied gradually among near strips. In order to quantify the cloaking at the desired frequency f_0 , the Maximum Radar Cross Section is computed and compared among the various structures.

Acronyms and notation

BW	Cloaking bandwidth [THz]
e	Electron charge [C]
E_s	Scattered electric field [V/m]
E_z^{inc}	Z -component of the incident electric field [V/m]
E_z	Z -component of the total electric field [V/m]
$f_d(\epsilon)$	Fermi-Dirac distribution
f_0	Cloaking frequency [THz]
h	Dielectric thickness [μm]
\hbar	Reduced Plank's constant [eV ps]
k_b	Boltzmann constant [eV K ⁻¹]
MaxRCS	Maximum Radar Cross Section
MaxRCS _{dB}	Maximum Radar Cross Section in decibel [dB]
PEC	Perfect Electric Conductor
R	Distance [m]
RCS	Radar Cross Section [m ²]
T	Temperature [K]
TO	Transformation Optics
w	Rectangular strip width [μm]
x	Spacing [μm]
Γ	Scattering rate of <i>graphene</i> [ps ⁻¹]
ϵ_r	Dielectric constant
λ_0	Wavelength at the cloaking frequency [μm]
μ_c	Chemical potential of the <i>graphene</i> [eV]
σ	Surface conductivity of <i>graphene</i> [C ² / (eV ps)]
σ^{inter}	Inter-band contribution of the surface conductivity of <i>graphene</i> [C ² / (eV ps)]
σ^{intra}	Intra-band contribution of the surface conductivity of <i>graphene</i> [C ² / (eV ps)]
τ	Relaxation time of <i>graphene</i> [ps]
ω	Angular frequency [ps ⁻¹]

Chapter 1

Introduction

1.1 Background and thesis aim

Cloaking has reached an important role during the last years in different fields: reducing mutual coupling among nearby antennas, reaching invisibility from radars in the military field, increasing view during a surgery or in the means-of-transport field.

Among the various techniques, there is *mantle cloaking*. It adopts a patterned surface around the object to be cloaked in order to generate proper surface currents when that surface is irradiated by an external field. The role of the mantle cloak is to cancel the scattered field from the object.

In this discussion, *graphene* is used in the patterned metallic surface working as cloaking coat. It has extraordinary properties, such as the tunability of the surface conductivity varying the chemical potential μ_c . So, the surface impedance of *graphene* can be easily modified, allowing to generate different surface currents when this material is illuminated by a wave.

In this thesis, the description of cloaking, focusing on *mantle cloaking*, and of the *graphene* properties is carried out and how to cloak a cylinder of PEC is investigated, looking for the parameters values that allow to reach the maximum scattering reduction. In order to measure the performances of each cloaking structure, the Radar Cross Section is employed. The Radar Cross Section of the uncloaked cylinder, downshifted by 3dB, is taken as limit that separates the cloaked region from the uncloaked one.

1.2 State of the art

As already said, *mantle cloaking* can be applied in many fields.

One of the applications is the possibility of placing many transmitting antennas, each one working at a different resonant frequency, electrically close each other. In case of two antennas, it is possible to reduce the mutual blockage effect by covering each antenna with a particular coating at the resonant frequency of the other one. This allows to restore the original antenna performances, as the radiators were in free space. Besides, since the cloak works at a different resonant frequency from the antenna's one on which it is applied, the cloak does not affect the antenna operation [1] [2].

Another possibility is reducing the interference due to obstacles placed near an antenna. This happens in a similar way to the previous case, coating the obstacles with specific cloaks [1] (Fig. 1.2).

Mantle cloaking can be applied also in case of sensors/receiving antennas. The cloaking, in this case, is realized on the antenna/sensor of which a reduction of scattered power is required [1]. It is necessary to suppress the scattered waves because they disturb the probed field and so also the measurement. Moreover, they make the sensor detectable to its surroundings and this could not be convenient for certain applications.

Potential applications of the cloaking of objects are in the means-of-transport field and in the medical one. Making the cockpit floor of an aircraft or the rear of a car transparent are examples of the first case. The visibility range of the pilot is strongly increased, improving security and

avoiding accidents. As regards the medical field, surgeons could see the tissue under their hands and instruments, limiting the possibility of committing errors during the operation [3].

Also military applications are possible. Covering military jets with specific coats allows to become invisible to human eye or to evade radar detection. Some Countries like China and USA have already developed and tested some solutions [4] [5] (Fig. 1.2).

1.3 Thesis outline

This thesis consists of 4 chapters:

- In the Chapter 1 an introduction of the topic of thesis and a discussion on the most relevant applications are given.
- In the Chapter 2 cloaking is presented focusing on *mantle cloaking*. Moreover, *graphene's* properties are discussed, highlighting surface conductivity, surface impedance, tuning of the chemical potential and biasing of *graphene*.
- In the Chapter 3 the simulation settings and results of a planar structure, made of the same materials of the cylinder to be cloaked and of the coat, are presented. Besides, the Radar Cross Section is defined and the simulation settings to compute it are shown.
- In the Chapter 4 all the simulated structures and the respective results are shown and discussed.
- Finally, in the Chapter 5 some variations of the best cloaked solution about the structure and the settings are carried on.

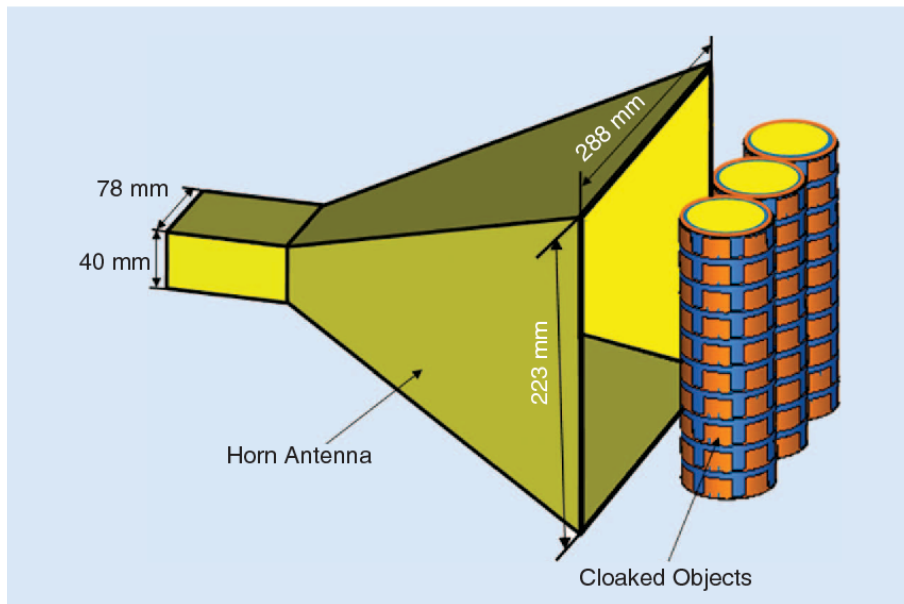


Figure 1.1: The figure shows an horn antenna with three cylinders. Since the cylinders are cloaked, they do not create perturbation of the electromagnetic waves radiated by the antenna [7].



Figure 1.2: Chinese fight aircrafts on which particular cloaking coats are tested in order to evade radars [4].

Chapter 2

Theoretical introduction

2.1 Cloaking

Cloaking is the cancellation of the scattered electromagnetic field from an arbitrarily shaped object. This is realized by employing a cover that surrounds the object, which causes the total scattering suppression for some or all the observation angles in near- and/or far-field [7] (Fig. 2.1a). This phenomenon can be seen also in another way: a light ray traveling through the cloak must arrive to the observer at the same time instant as a ray that would have passed through an empty space (Fig. 2.1b). Since the diverted light takes a longer path, it should exceed the speed of light in vacuum. But this would violate the Einstein's theory of special relativity. There is no violation of the theory only if the cloak works over an extremely narrow bandwidth [10].

Several approaches allow to obtain cloaking. Among them :

- *transformation optics* (TO): based on the manipulation of the electromagnetic wave propagation in such a way that the cloak bends the wave around the object [7] (Fig. 2.1b);
- *plasmonic cloaking*: uses an homogeneous layer with negative or near-zero dielectric constant to cancel the polarization currents of the object to hide [11] (Fig. 2.2);
- *mantle cloaking*: consists in achieving the compensation of the scattering of a given object using artificial materials (metasurfaces) with proper values of the surface impedance [1].

Mantle cloaking is the approach adopted in the following. More precisely, in this case the scattering cancellation is achieved by inducing suitable surface currents on the cloak surface. The surface current induced by the impinging wave radiates scattered fields that are in "anti-phase" with respect to those ones due to the object to be cloaked. This causes a strong reduction of the overall visibility of the system [12].

The cloak surface adopted in this case is a patterned metallic surface. Changing the pattern, it is possible to vary the surface impedance of the layer, and so also the associated surface currents. In this discussion the object is wanted to be cloaked at 3 THz.

The performance of a cloak is usually evaluated comparing the total scattering cross-sections of the bare and the cloaked object.

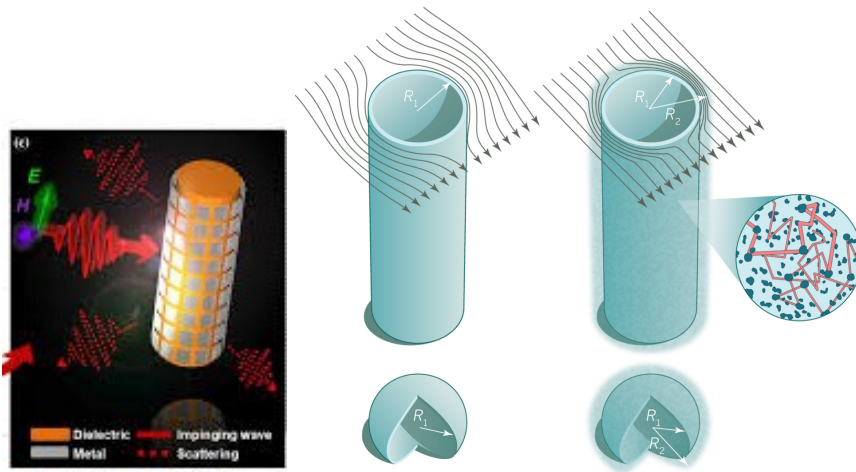


Figure 2.1: a) Impinging wave on an object covered by a structure (metamaterial) in order to avoid scattering [8]; b) waves pass around the object thanks to the use of the cloak [10].

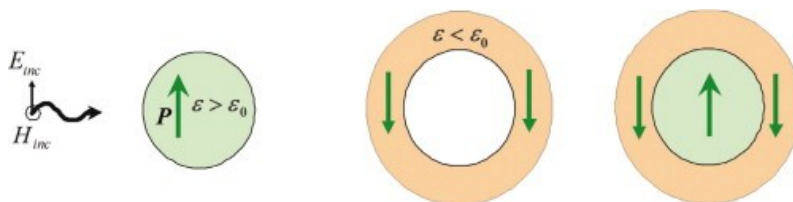


Figure 2.2: Illustration of the plasmonic cloaking [9]. A spherical dielectric object with electric permittivity higher than the surrounding medium is covered by a dielectric shell with electric permittivity smaller than the surrounding medium. Choosing a particular value of the shell diameter, it is possible to obtain that the scattering of the object and of the shell cancel each other.

2.2 Graphene

The material adopted in this discussion in order to obtain the cloaking of an object in the low frequencies of the Terahertz range is *graphene*. *Graphene* is a two-dimensional hexagonal lattice of carbon atoms [13]. Since its discovery in 2004, it has gained a huge interest for its stable thermal and mechanical properties and for some extraordinary electronic properties, such as high carrier mobility and Fermi velocity ($v_f \cong 10^8 \text{ cm}\cdot\text{s}^{-1}$), mechanical flexibility, robustness [14, 15]. Some numerical values of these properties are reported in Tab. 2.1.

2.2.1 Surface conductivity

Another relevant characteristic of the *graphene* is the possibility to tune its surface conductivity, and so also the surface impedance, by varying its chemical potential. The complete formula of the *graphene* surface conductivity σ is shown in (2.1) [17]:

$$\sigma(\omega, \mu_c, \mathbf{\Gamma}, \mathbf{T}) = \frac{j e^2 (\omega - j2\mathbf{\Gamma})}{\pi \hbar^2} \left[\frac{1}{(\omega - j2\mathbf{\Gamma})^2} \int_0^\infty \epsilon \left(\frac{\partial \mathbf{f}_d(\epsilon)}{\partial \epsilon} - \frac{\partial \mathbf{f}_d(-\epsilon)}{\partial \epsilon} \right) \mathbf{d}\epsilon - \int_0^\infty \frac{\mathbf{f}_d(-\epsilon) - \mathbf{f}_d(\epsilon)}{(\omega - j2\mathbf{\Gamma})^2 - 4(\epsilon/\hbar)^2} \mathbf{d}\epsilon \right] \quad (2.1)$$

where k_b is the Boltzmann constant, e is the electron charge, \mathbf{T} is the temperature (in Kelvin), ω is the angular frequency, $\mathbf{\Gamma}$ is the scattering rate of the *graphene*, \hbar is the reduced Plank's constant, μ_c is the chemical potential and $\mathbf{f}_d(\epsilon)$ is the Fermi-Dirac distribution.

$$\mathbf{f}_d(\epsilon) = (e^{\frac{\epsilon - \mu_c}{k_b T}} + 1)^{-1} \quad (2.2)$$

Equation (2.1) describing the conductivity can be rewritten in a closed-form obtaining the *Kubo formula* [17]. This latter shows two contributions: the *intra-band* and the *inter-band* one. The difference between the two contributions stays in the excited state by the carrier (electron or hole): if it is a state of the same band in which the carrier was, the contribution is called *intra-band*, otherwise it is named *inter-band*.

$$\sigma(\omega, \mu_c, \mathbf{\Gamma}, \mathbf{T}) = \sigma_{\text{intra}}(\omega, \mu_c, \mathbf{\Gamma}, \mathbf{T}) + \sigma_{\text{inter}}(\omega, \mu_c, \mathbf{\Gamma}, \mathbf{T}) \quad (2.3)$$

$$\sigma_{\text{intra}}(\omega, \mu_c, \mathbf{\Gamma}, \mathbf{T}) = -j \frac{k_b e^2 T}{\pi \hbar^2 (\omega - j2\mathbf{\Gamma})} \left(\frac{\mu_c}{T k_b} + 2 \ln \left(e^{-\frac{\mu_c}{T k_b}} + 1 \right) \right) \quad (2.4)$$

$$\sigma_{\text{inter}}(\omega, \mu_c, \mathbf{\Gamma}) = j \frac{e^2}{\pi 2 \hbar} \ln \left(\frac{2|\mu_c| - (\omega - j2\mathbf{\Gamma})\hbar}{2|\mu_c| + (\omega - j2\mathbf{\Gamma})\hbar} \right) \quad (2.5)$$

Using eqs. (2.1) and (2.3), the surface conductivity has been computed on Matlab as function of the chemical potential μ_c and of the frequency. To do the computations, parameters have been fixed to particular values, as follows:

- $T = 293 \text{ K}$;
- $\tau = 0.1 \text{ ps}$.

From the relaxation time τ , the scattering rate $\mathbf{\Gamma}$ is computed as function of the chemical potential μ_c (see eq. (2.6)):

$$\mathbf{\Gamma} = \frac{1}{2\tau} \quad (2.6)$$

The evaluated frequency range is from 0 to 20 THz. As regards the chemical potential, it is varied from 0.1 eV to 1 eV. The case 0 eV has not been computed because the considered formulas do not allow to do it. The resulting graphs are shown in Figs. 2.3 and 2.4. The behaviour of the surface conductivity is identical using the two formulas, the exact one (2.1) and the approximated one (2.3). The real part, always positive, has a decreasing behaviour until 1 THz that increases raising the chemical potential and, then, it remains constant. The imaginary part, instead, is negative and reduces until 1 THz (there is more reduction increasing the chemical potential) and, then, increases, converging to 0 (the convergence is faster for low μ_c).

Table 2.1: Table containing the electronic and mechanical properties of *graphene* [16].

Electronic mobility	up to $200000 \text{ cm}^2 \text{ V}^{-1} \text{ s}^{-1}$
(In-plane) thermal conductivity	$3000\text{-}5000 \text{ W m}^{-1} \text{ K}^{-1}$
Tensile strength	$1.3 \cdot 10^{11} \text{ Pa}$
Weight per m^2	0.77 mg m^{-2}
Spring constant	$1\text{-}5 \text{ N m}^{-1}$
Young 's modulus	0.5 TPa

As regards the open-form formula (eq. (2.1)), the first integral has been computed between 0 and 14, instead of the range $(0, \infty)$. This choice has been taken because computing the integral until ∞ doesn't allow to obtain any results: actually the result would be ∞ since from the right side the integrand function dfe (eq. (2.7)) never reaches the 0 value. Looking at all the behaviors of the integrand function, it is possible to notice that the value of the function is always very small (of the order of 10^{-4}) from 14 on, so the contribution of the function after index 14 can be neglected. At Fig. 2.5, the extreme behaviour of the integrand function dfe is shown.

$$\mathbf{dfe} = \epsilon \left(\frac{\partial \mathbf{f}_d(\epsilon)}{\partial \epsilon} - \frac{\partial \mathbf{f}_d(-\epsilon)}{\partial \epsilon} \right) \quad (2.7)$$

2.2.2 Surface impedance

From the obtained surface conductivity, the surface impedance of the *graphene* has been computed. Actually, only the inverse of the conductivity has been computed that is proportional to the impedance, since also the cross section area and the length are needed to compute the impedance (Fig. 2.6).

The behaviour of the surface impedance is the same to that one provided by CST Microwave Studio [20], only the scale changes (Fig. 2.7). The resistance has a monotonic increase for low chemical potentials, that reduces with higher potentials reaching a flat behaviour. As regards, instead, the reactance, it increases almost linearly with frequency. Both components are positive and the higher values are reached for low μ_c .

CST Microwave Studio provides also the behaviour of the graphene surface impedance with respect to frequency when the chemical potential μ is 0 eV (Fig. 2.8). It is completely different from the cases with other values of the chemical potential, since both the resistance and the reactance have an almost sinusoidal behaviour.

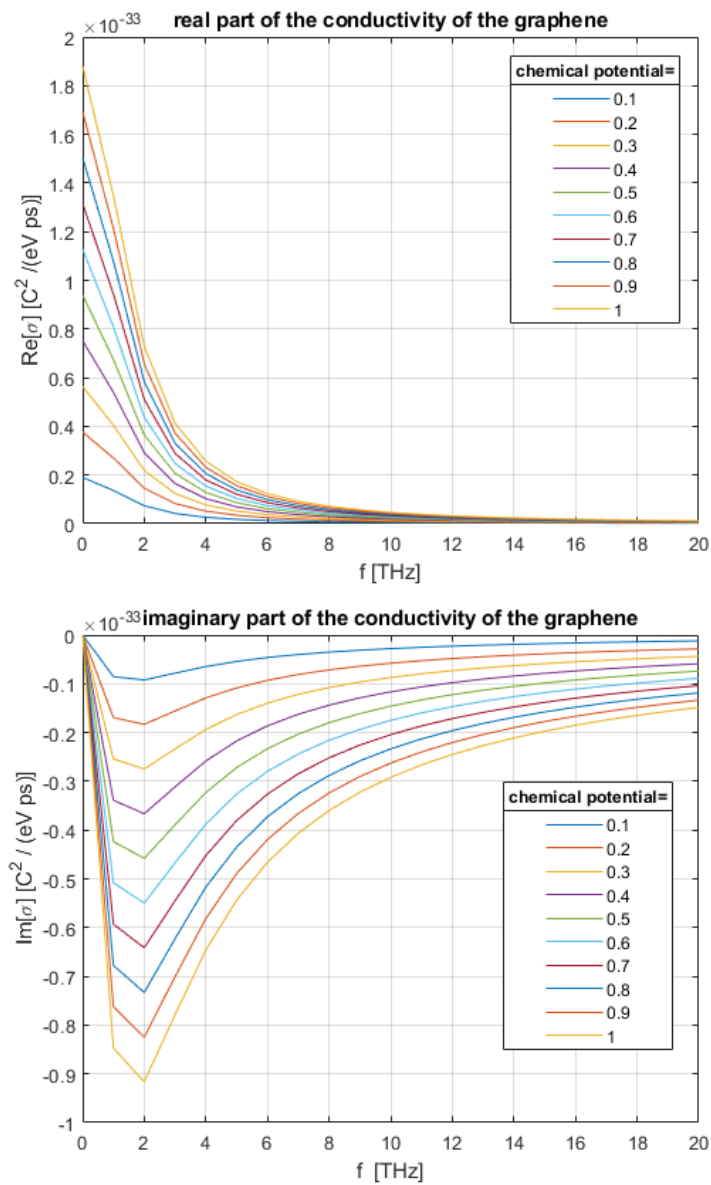


Figure 2.3: Real and imaginary part of the surface conductivity of graphene with respect to frequency, varying the chemical potential. Case computed with eq. (2.1).

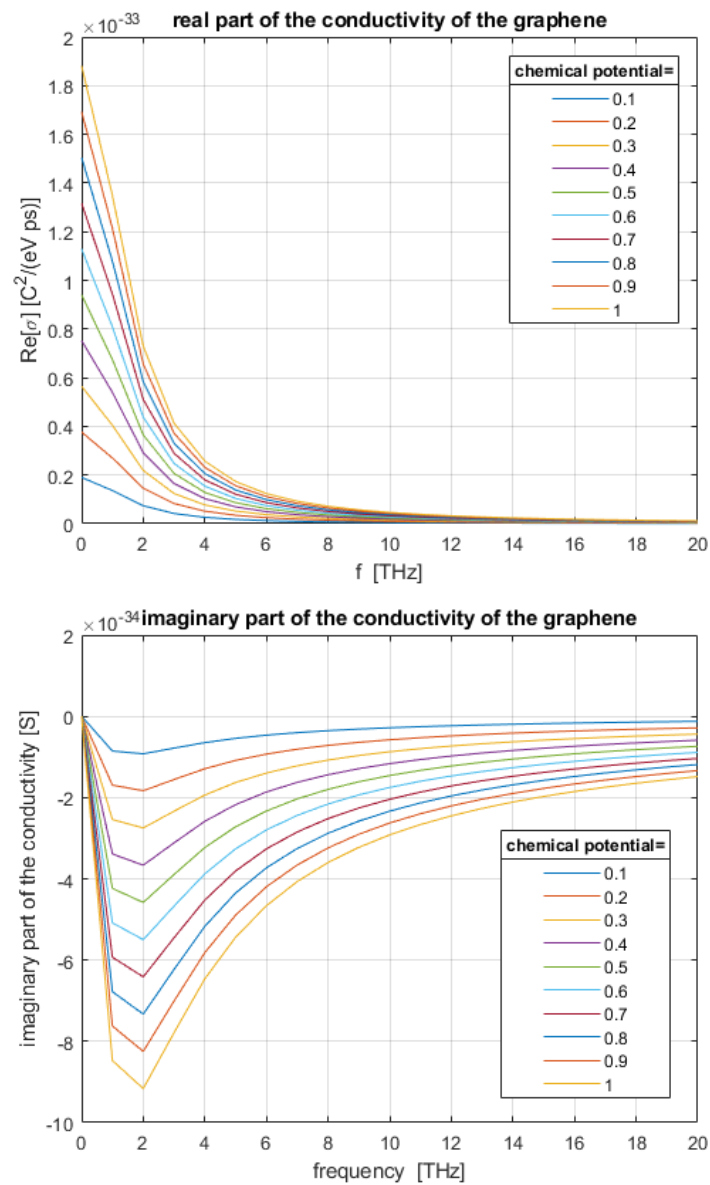


Figure 2.4: Real and imaginary part of the surface conductivity of graphene with respect to frequency, varying the chemical potential. Case Kubo formula (eq. (2.3)).

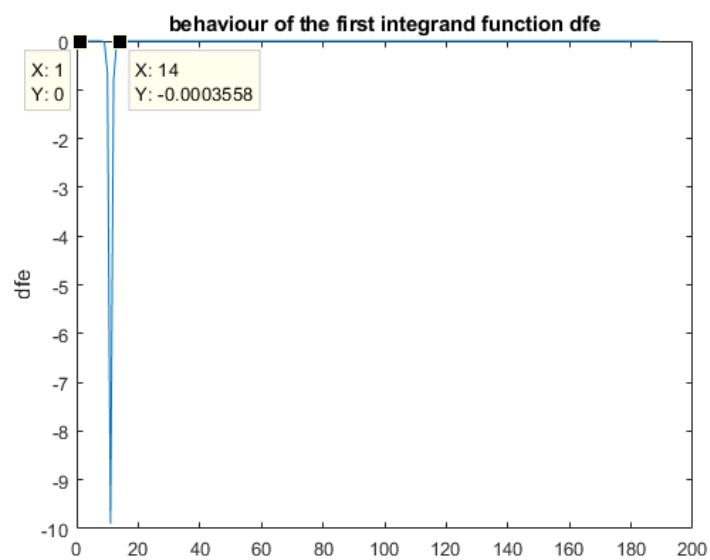


Figure 2.5: Behaviour of the first integrand function dfe of the surface conductivity formula (eq. (2.1)).

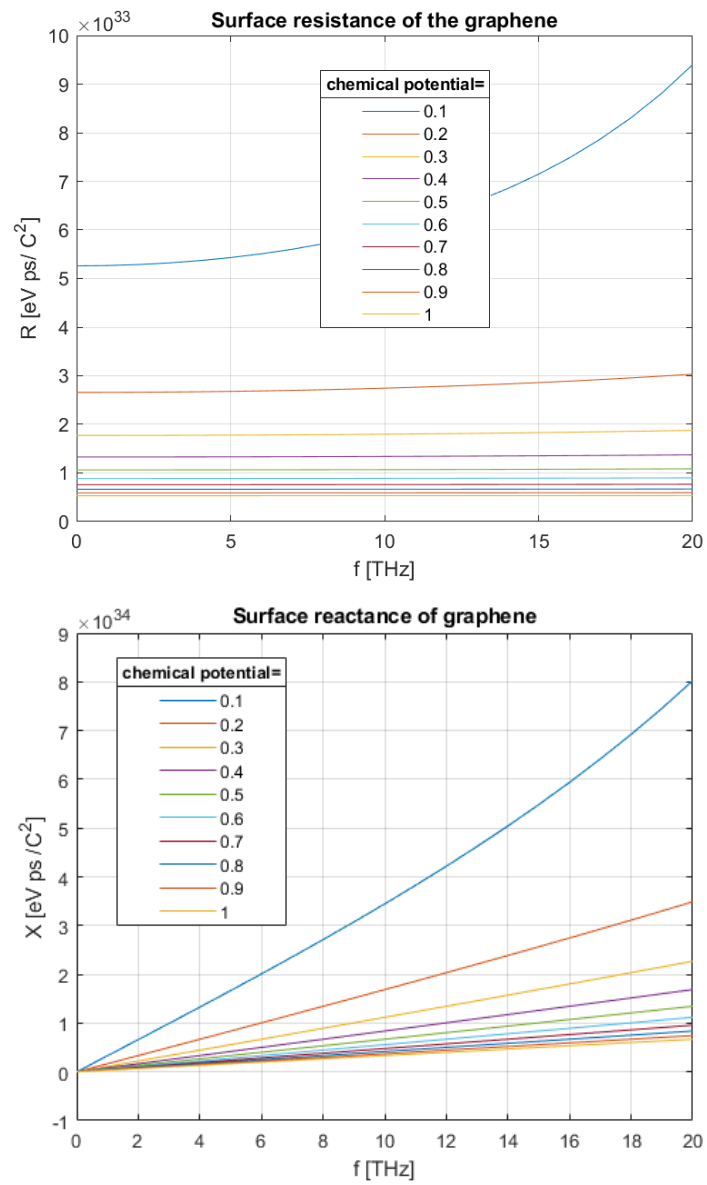


Figure 2.6: Surface resistance and reactance of graphene computed from Kubo formula (eq (2.3)).

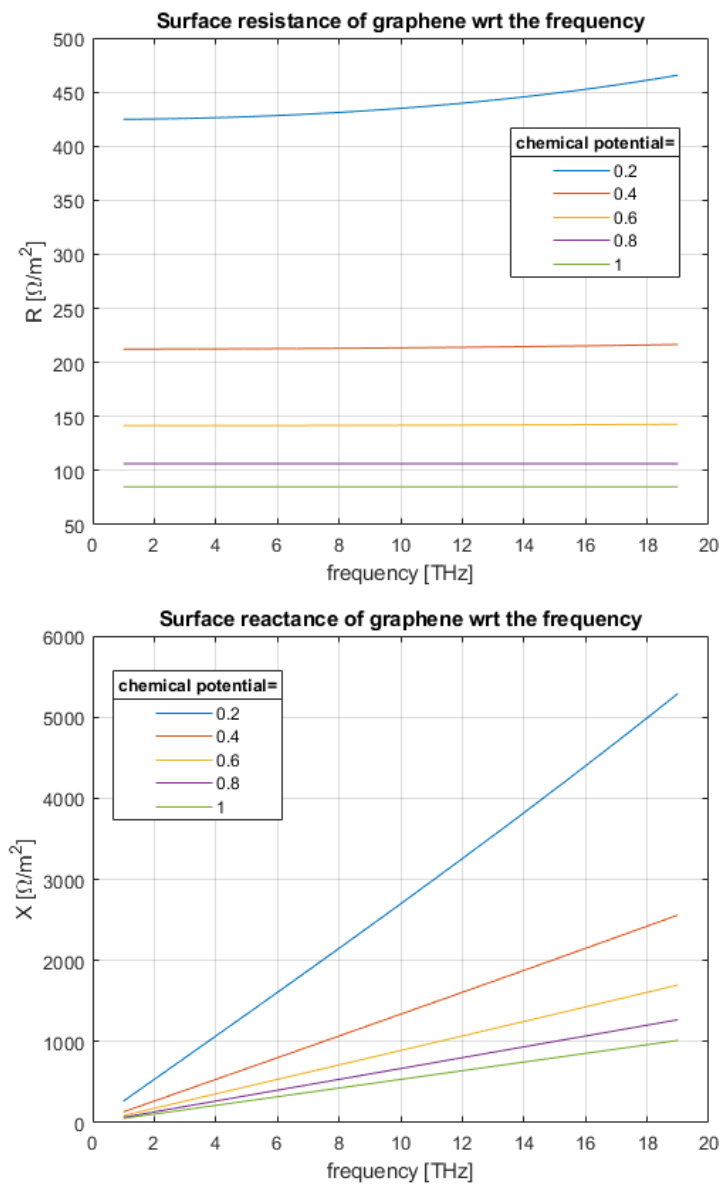


Figure 2.7: Surface resistance and reactance of graphene computed by CST.

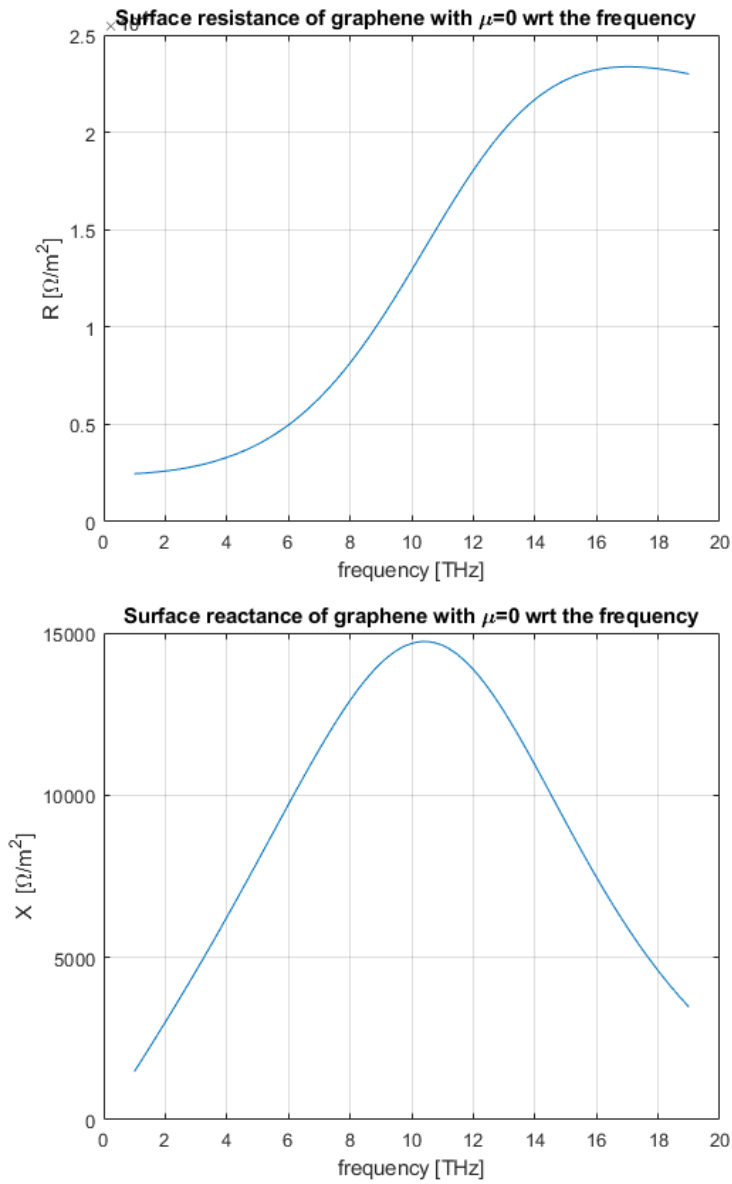


Figure 2.8: Surface resistance and reactance of graphene computed by CST when the chemical potential μ_c is 0 eV.

2.2.3 Chemical potential tuning and limit values

The chemical potential of *graphene* can be tuned in various ways. Among them [21]:

- by applying an external gate voltage;
- by photo-induced doping;
- by the presence of carrier impurities;
- by structural corrugations;
- by molecular doping.

Regarding the first case, applying an external gate voltage generates an electrostatic field. It is not possible to apply fields of any strength because at a certain value the breakdown effect occurs in the substrate destroying the material. Usually only shifts in the chemical potential of the order of the meV can be reached.

To reach shifts of the order of the eV, it is necessary to adopt materials, like Silicon Dioxide SiO₂, since they contain charged impurities, and to employ them both above and below the *graphene* layer [21].

2.2.4 Biasing of the graphene

As said before, the chemical potential of the *graphene* can be tuned using a bias voltage. The bias voltage is applied between the sheet of *graphene* and a ground plate running parallel to the sheet. Usually, in cloaking applications, there is an external sheet of *graphene*, an inner substrate made by a dielectric and a metallic (or quasi-metallic) layer. The potential is applied to a gate electrode. The gate is usually located to the top of the substrate, underneath the *graphene* layer. From the other side, the voltage is connected to the metallic (or quasi-metallic) layer [18] (Fig. 2.9).

The chemical potential of the *graphene* can be varied also by illuminating it with a laser light (Fig. 2.10). In fact, this method tunes the charge carrier density of the *graphene*. According to the frequency of the light that impinges on *graphene*, a different μ_c is obtained. But, it is necessary to take care of the power of the laser irradiation: if the laser power is not enough low, the *graphene* will be irreversibly damaged (good values of laser power are of the order of the μW) [19]. This technique is useful mostly when vertical strips of *graphene* are required to have different chemical potentials, since in this case the bias voltage method cannot be applied.

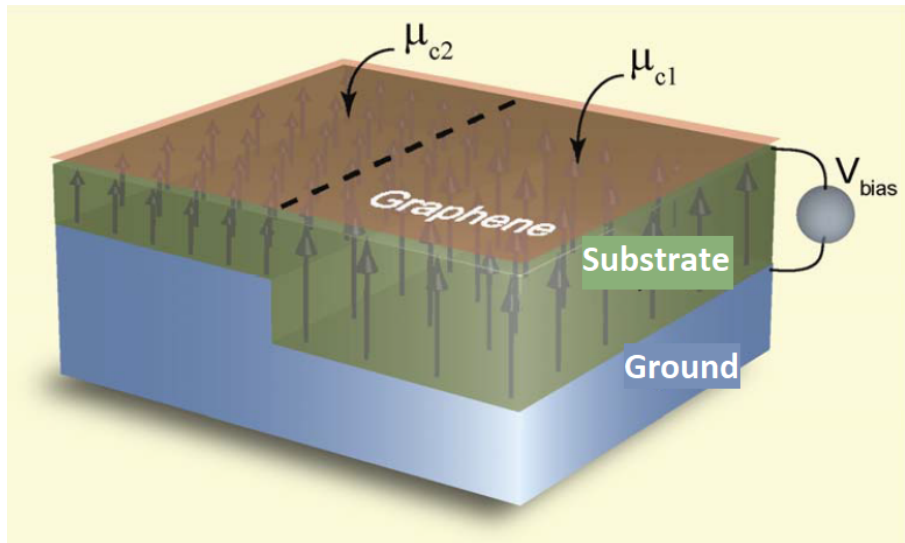


Figure 2.9: Connection of a bias voltage to a structure done by a graphene layer, a substrate and the ground plane in order to change the chemical potential. In this figure, the ground plane is uneven in order to obtain different chemical potentials in different parts of the structure adopting the same voltage but changing the thickness of the substrate [18].

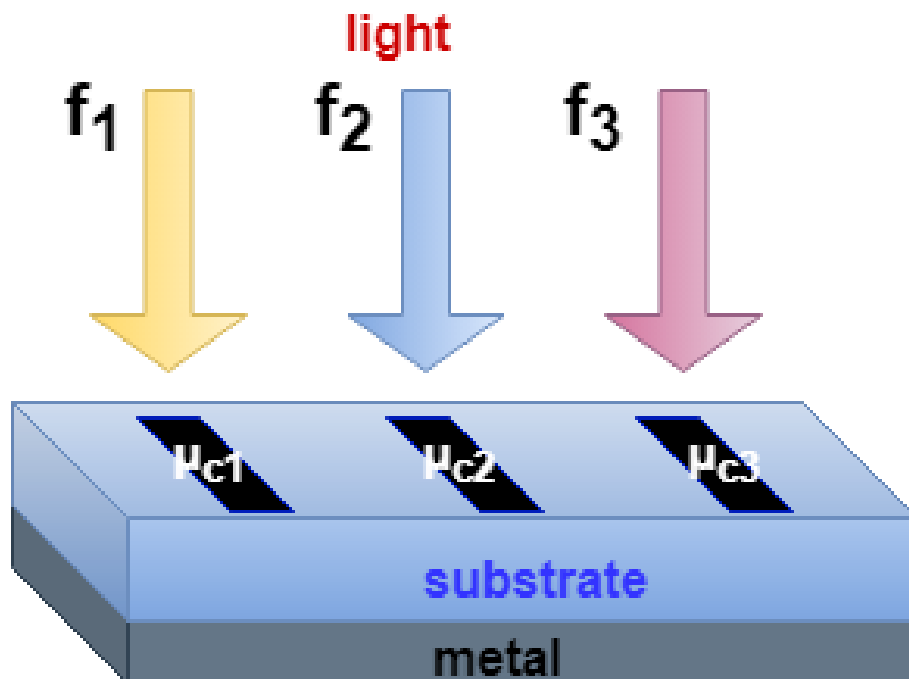


Figure 2.10: Illumination of *graphene* strips over a substrate with laser lights at different frequency.

Chapter 3

Planar structure and Radar Cross Section

3.1 Preliminary simulations

Before of doing simulations on the interested structure, few simulations have been done on planar structures, made by the same materials of the cylindrical one. In particular, a structure with ground plane, dielectric in the middle and equally spaced microstrips is considered (Fig. 3.1). The ground plane is made of PEC. For the dielectric, the Silicon Nitride Si_3N_4 (whose electric dispersion is fitted for the considered frequency range, obtaining an $\epsilon_r=3.89$) is used. Microstrip lines are realized with *graphene*, with different chemical potential. Here only the two extreme cases have been evaluated, one with $\mu_c=0$ eV and the other with $\mu_c=1$ eV. The structure is not realized by hand but writing a VBA macro in CST. The S-parameters are computed in the range 1 THz - 19 THz.

The adopted simulation settings are reported in Fig. 3.2 and Fig. 3.3.

Looking at Fig. 3.4, it is possible to notice that the scattering parameters change varying the chemical potential of the *graphene*. The S_{11} , in fact, is -2.635 dB at $f_0=3$ THz in case of 0 chemical potential, while it reduces to -9.19 dB in the other case. As regards the S_{31} parameter (that represents the amount of coupling among two close strips), the value for 0 chemical potential, at 3 THz, is -39.8 dB, while in the other case it is -46.76 dB. So, at f_0 the reflected power and the coupling among the strips is low at high chemical potentials. Considering the whole frequency range, the S_{11} at $\mu_c=0$ eV is higher than the case with $\mu_c=1$ eV until 14 THz, then the behaviour is inverted. As regards S_{31} , at $\mu_c=0$ eV the behaviour is almost always higher than the case with $\mu_c=1$ eV.

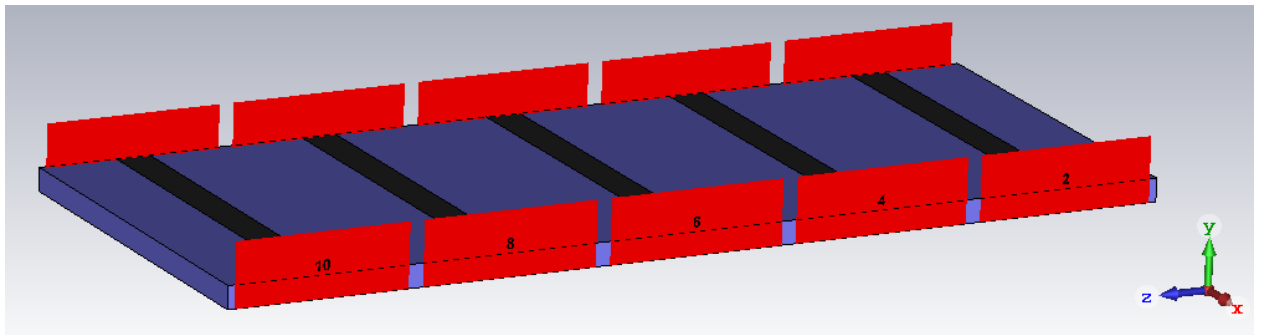


Figure 3.1: Planar structure of 5 parallel microstrip lines simulated in CST.

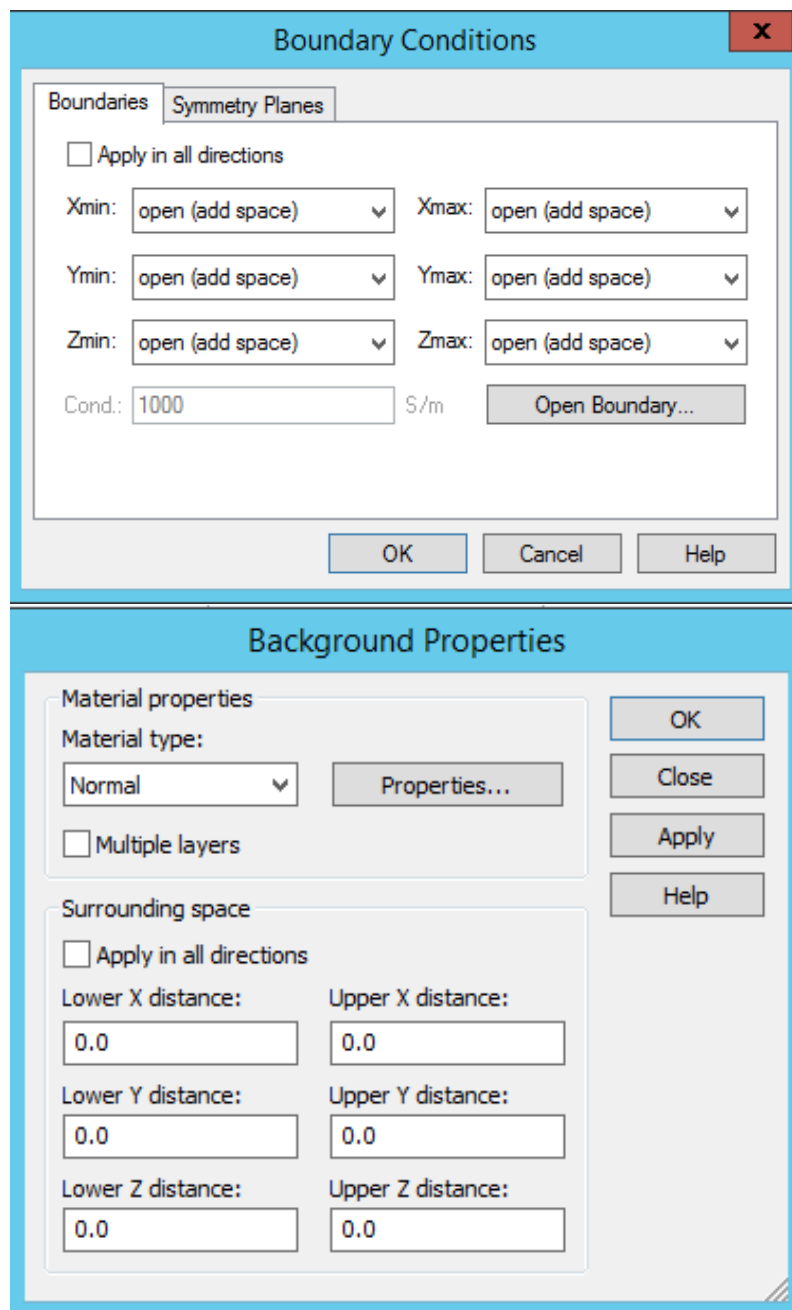


Figure 3.2: Boundary conditions and background properties set for the simulation of the planar structure in CST.

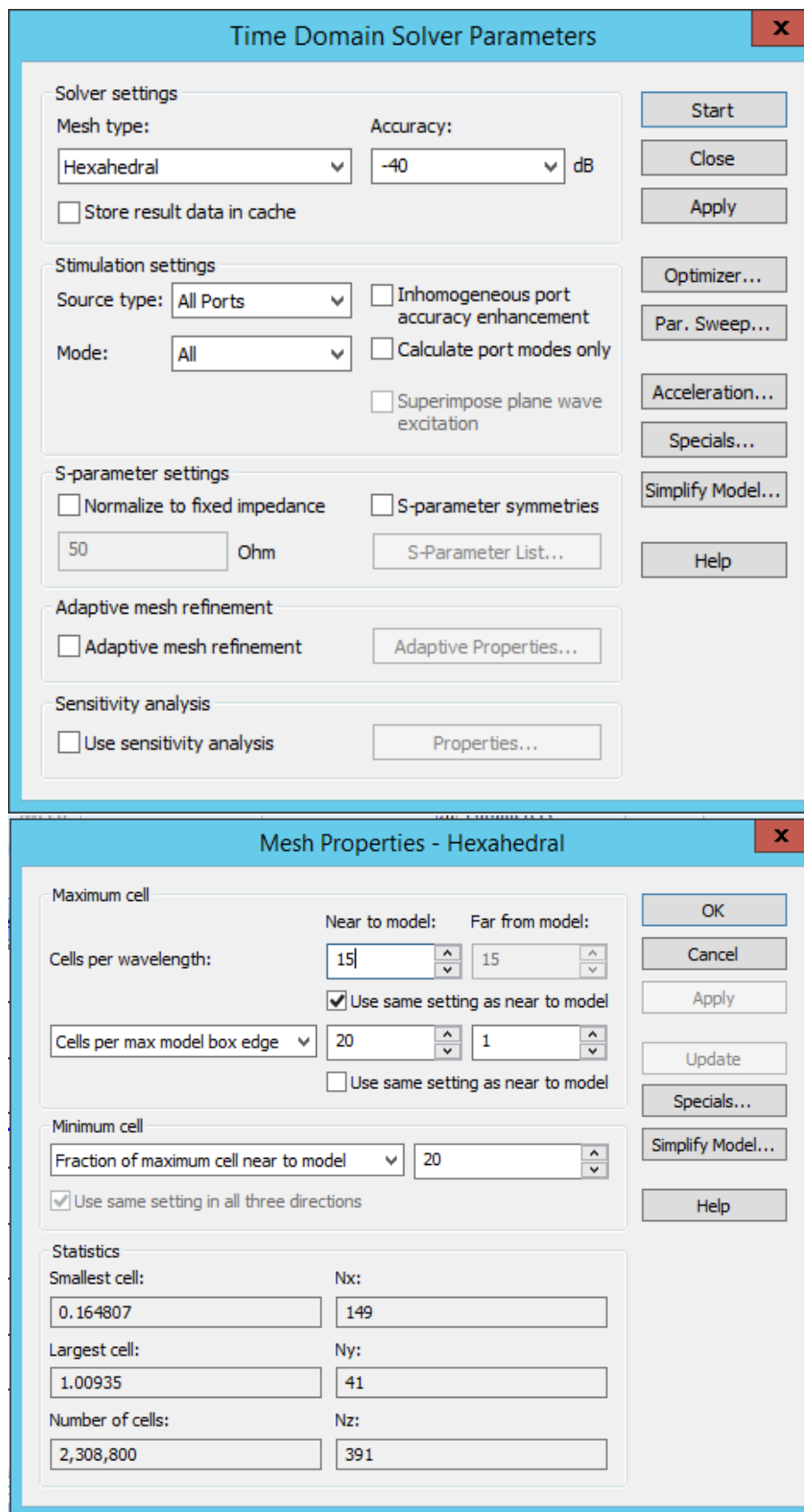


Figure 3.3: Time domain solver parameters and mesh properties set for the simulation of the planar structure in CST.

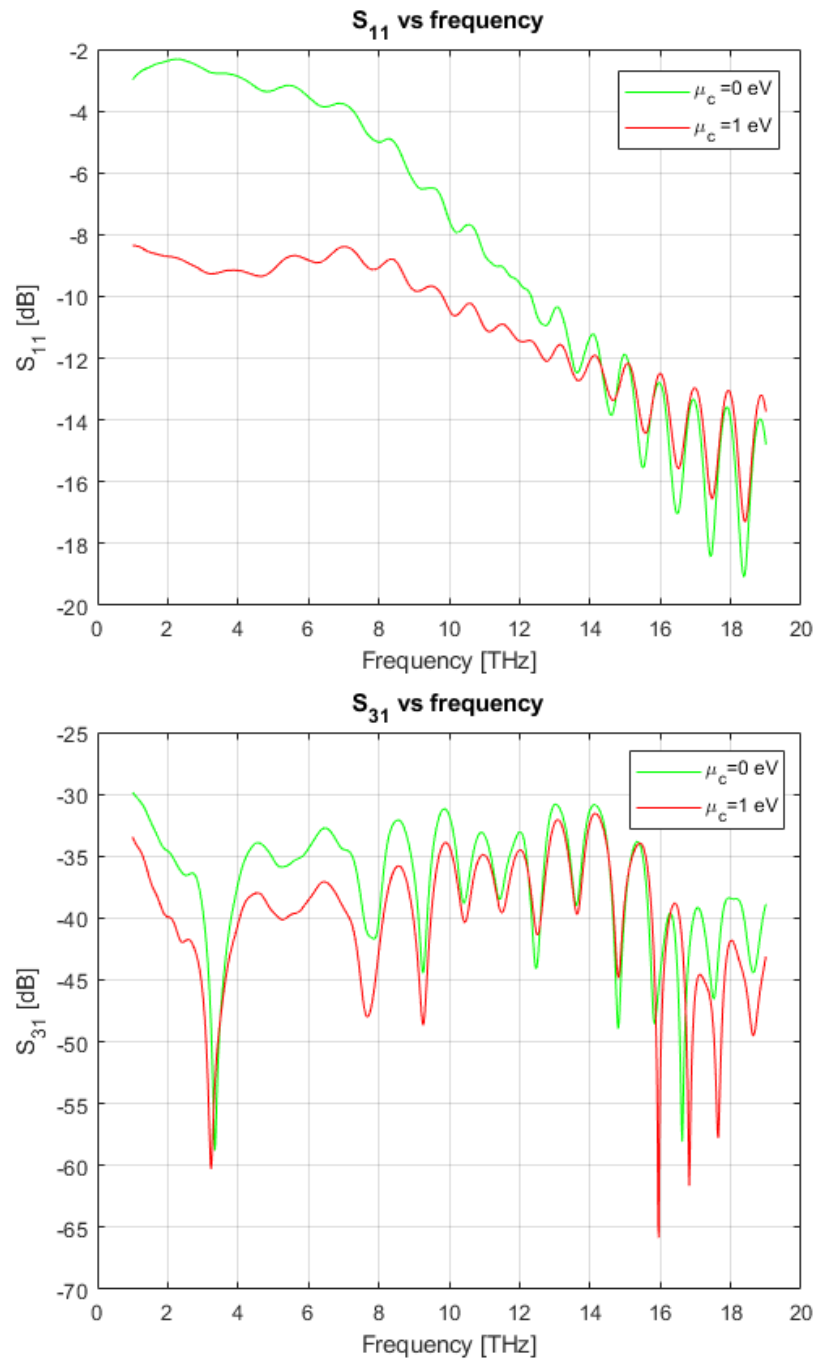


Figure 3.4: S_{11} (top) and S_{31} (bottom) for the two structures with microstrips of different chemical potential for the graphene: chemical potential 0 (green) and chemical potential 1 (red).

3.2 Radar cross section definition and Maximum RCS computation

The *radar cross section* (RCS) allows to compute the intensity of the electromagnetic waves scattered by an object, after being irradiated, towards the direction of the receiving antenna. It is measured in m^2 and its definition is reported in the following eq. (3.1):

$$\text{RCS} = \lim_{R \rightarrow \infty} 4\pi R^2 \frac{|\mathbf{E}_s|^2}{|\mathbf{E}_i|^2} \quad (3.1)$$

where \mathbf{E}_i is the incident field and \mathbf{E}_s is the scattered field by the object towards the receiver positioned at a distance R . The limit is used to mean that the measurement of RCS is done in far field.

The RCS is computed for different structures. To do this in CST, it is necessary to generate a plane wave incident on the object in the present study. A plane wave with linear polarization is adopted, with electric field parallel to the z -axis, with the same direction, (so also to the length of the cylinder) and with the direction of propagation normal to the cylinder (Fig. 3.7). The electric field is computed all around the cylinder in the plane $z=0$ at a distance that is at least five times the dimension of the cylinder in order to satisfy the far field condition. For this reason, $60 \mu\text{m}$ is chosen as distance from the center of the cylinder. This is made on CST in post-processing using a particular *Result templates*. Also the incident electric field is required to compute the RCS. So, a cylinder made of vacuum is simulated and the electric field is computed in the same way of the previous case. Now the resulting electric field is only the incident one, since there is no actual obstacle to the wave. The simulation settings of the cylinder of PEC are shown in the Figs. 3.5, 3.6 and 3.7. The total simulation time is 14s. The simulation settings for the cylinder of vacuum are the same (but, as expected, the simulation time is smaller).

The RCS, for a fixed frequency, is computed for 3771 points around the cylinder (where the electric field has been computed) and the maximum among them is considered for each frequency:

$$\text{MaxRCS} = \max_{\phi} \frac{|\text{Re}\{\mathbf{E}_z\} + j \text{Im}\{\mathbf{E}_z\} - (\text{Re}\{\mathbf{E}_{z \text{ inc}}\} + j \text{Im}\{\mathbf{E}_{z \text{ inc}}\})|^2}{|\text{Re}\{\mathbf{E}_{z \text{ inc}}\} + j \text{Im}\{\mathbf{E}_{z \text{ inc}}\}|^2} \Bigg|_{\phi} \quad (3.2)$$

where \mathbf{E}_z is the total (scattered and incident) electric field at a given frequency, while $\mathbf{E}_{z \text{ inc}}$ is the incident electric field at the same frequency. The obtained RCS has, in this case, no measuring unit because it has no dimension. It is also possible to convert the RCS in dB:

$$\text{MaxRCS}_{\text{dB}} = 10 \log \text{MaxRCS} \quad (3.3)$$

3.2.1 RCS computed on a point behind the cylinder

It is possible to compute a less accurate version of the RCS taking into account only the electric field in a point exactly behind the object with respect to the direction of illumination. A probe is positioned opposite to the plane wave source, quite far from the object (at the coordinates $50,0,0 \mu\text{m}$), in order to compute the electric field in that point for all the three orientations (Fig. 3.9). The plane wave polarization is the same of the one adopted to compute the Maximum RCS. Only the field in the same direction of the electric field generated by the plane wave is taken into account, since in the other directions the electric field is zero for the used plane wave. In order to obtain only the scattered field by the cylinder behind it, it is required to compute also the incident electric field using a probe in the same place as before and changing the material of the whole object to vacuum. The incident electric field is, then, subtracted from the total electric field computed for the cylinder, getting as result the scattered field by the cloaked object in that point. Actually, then the so-obtained electric field is normalized with respect to the incident one, getting an a-dimensioned result. The settings for the simulation of the behaviour of the cylinder are the same as before, so only the definition of the probe is shown (Fig. 3.9). Looking at the *log file* of this simulation in CST, it is possible to notice that the total simulation time is 9s.

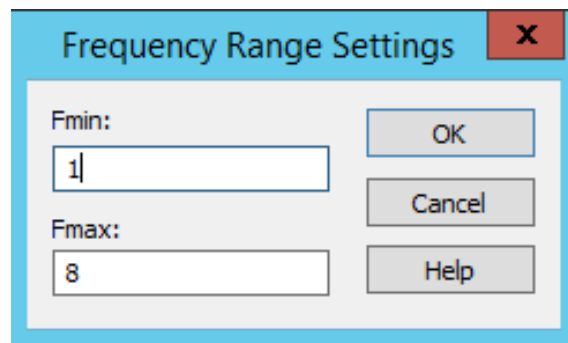


Figure 3.5: Frequency settings for the simulation of the cylinder made of PEC in CST.

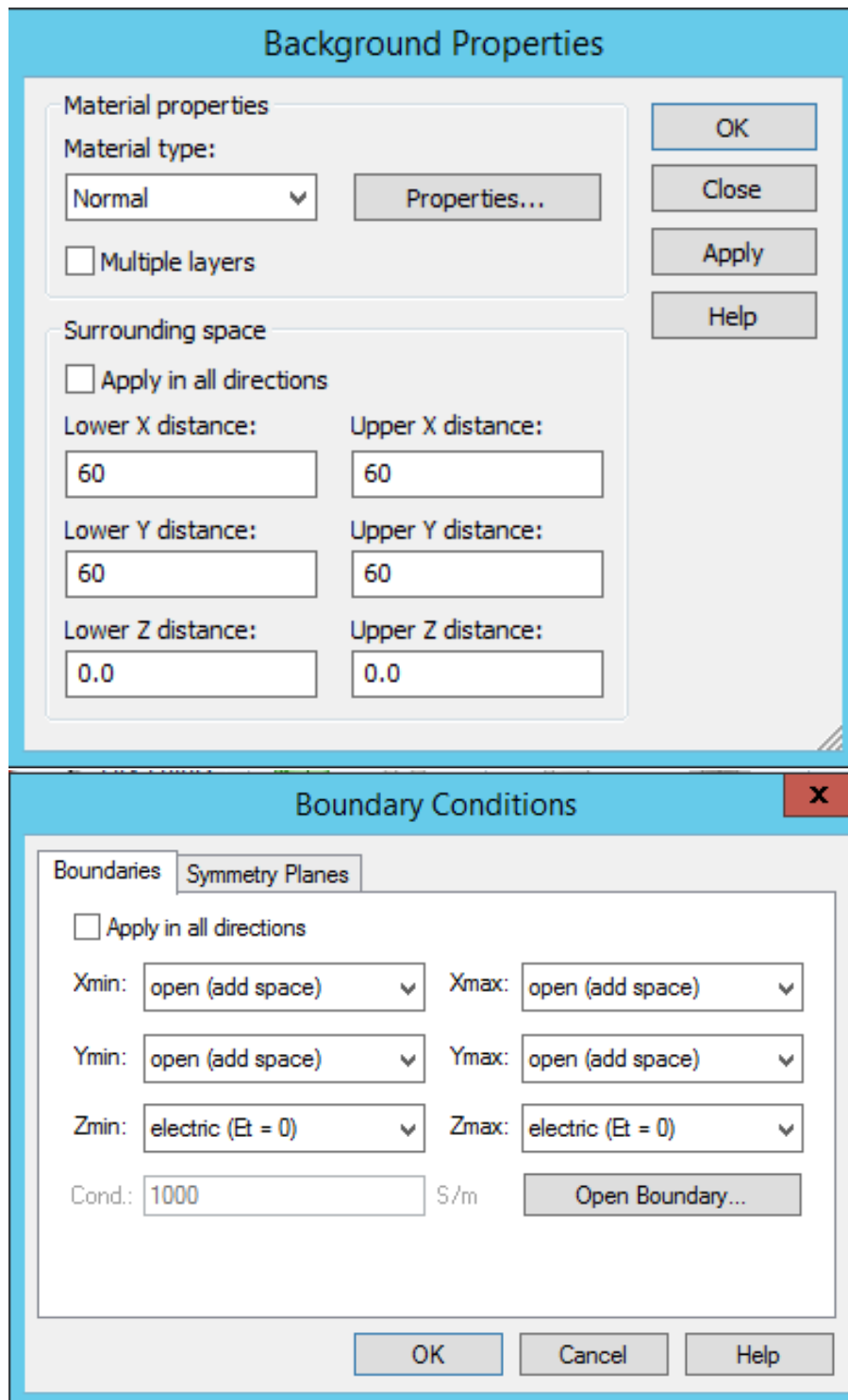


Figure 3.6: Boundary conditions and background properties set for the simulation of the cylinder made of PEC in CST.

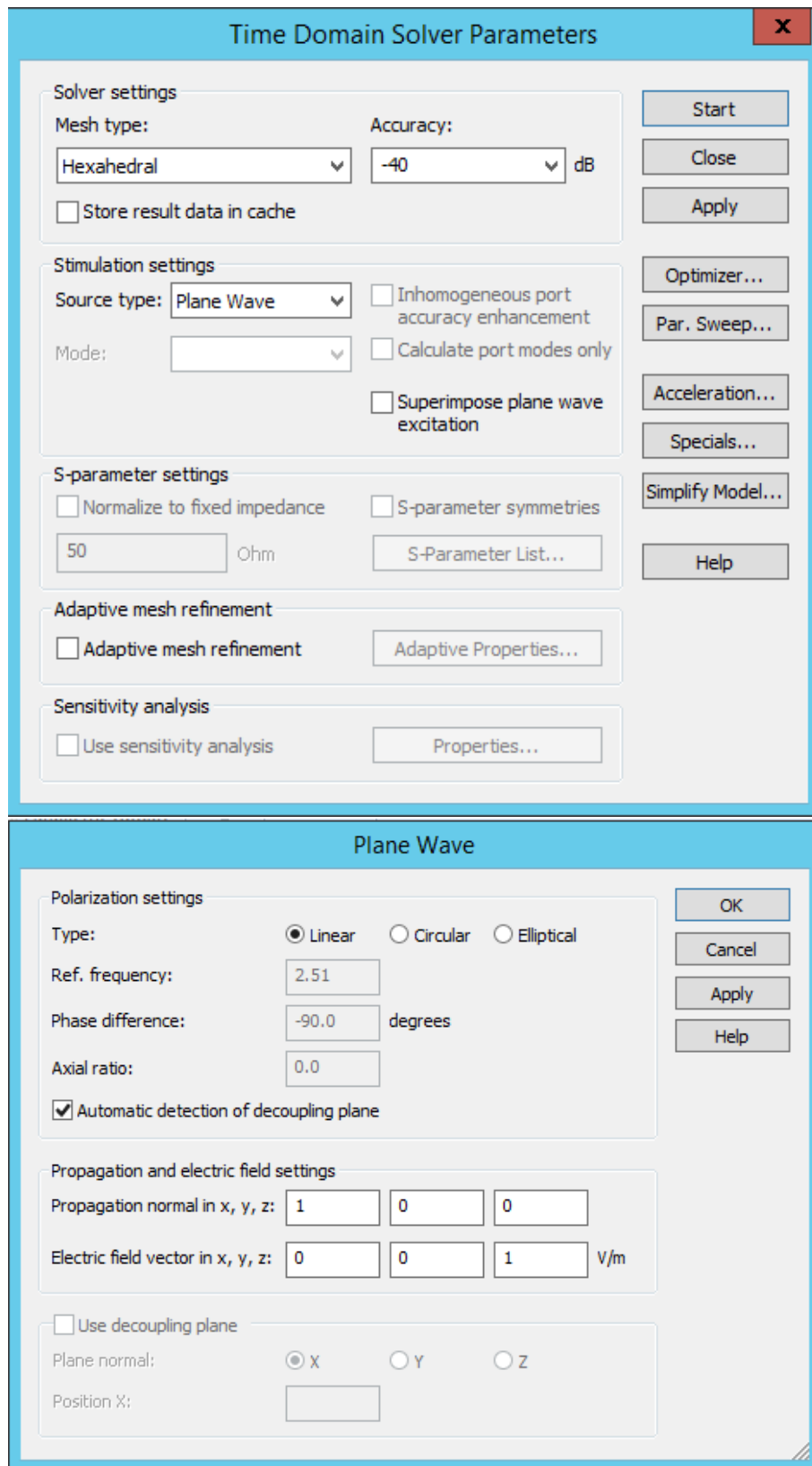


Figure 3.7: Time domain solver parameters and plane wave settings for the simulation of the cylinder made of PEC in CST.

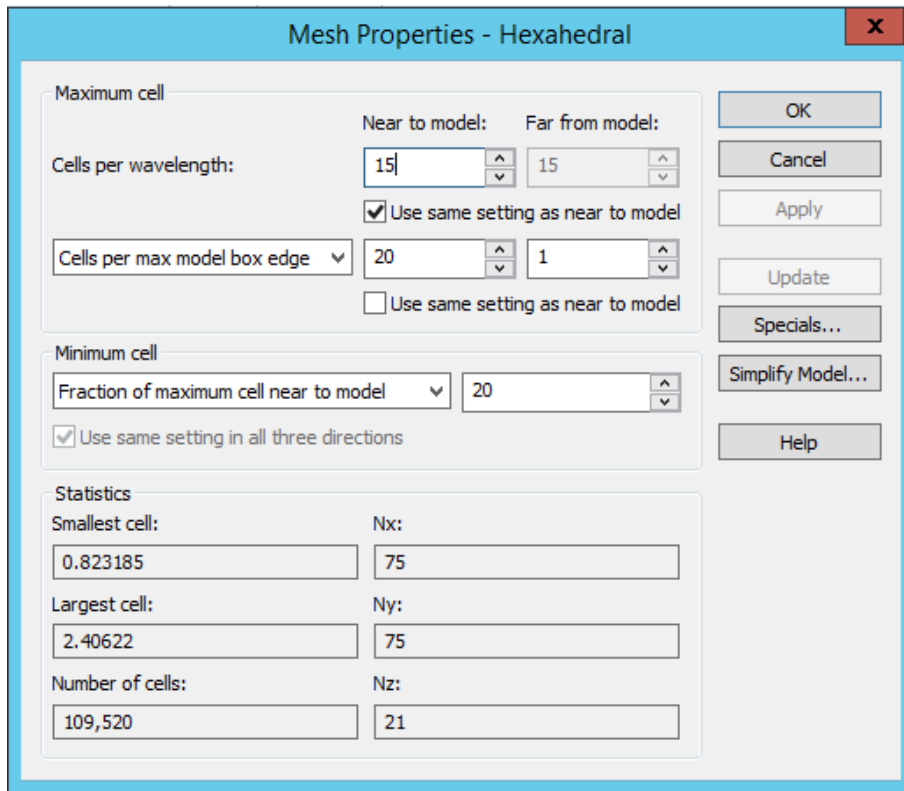


Figure 3.8: Mesh properties for the simulation of the vacuum cylinder in CST.

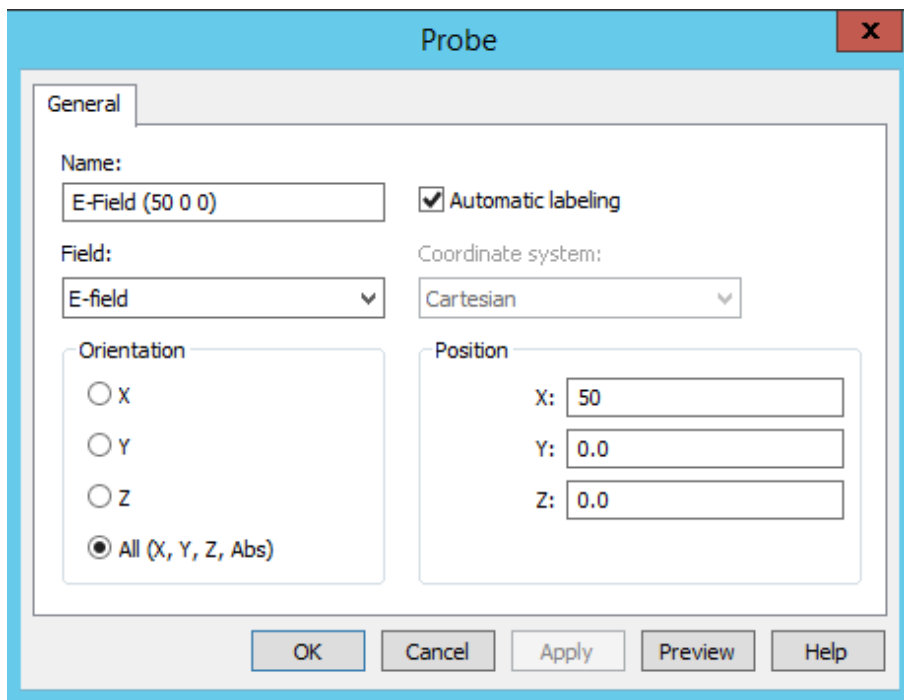


Figure 3.9: Probe settings in CST.

Chapter 4

Simulation of the bare cylinder and of the different cloaked structures

4.1 Study of the bare cylinder behaviour

First, the case of a cylinder made of PEC is considered (Fig. 4.1). This cylinder has a radius of $\lambda_0/12 \mu\text{m}$ and a length of $\lambda_0/6 \mu\text{m}$ (even if for the adopted boundary conditions the cylinder is simulated as if it was infinitely long), where $\lambda_0 = 100 \mu\text{m}$ because it is computed considering $f_0 = 3 \text{ THz}$ (the frequency in which the cloaking is desired). Its Maximum RCS is adopted in order to find the bandwidth in which the cloaking effect is reached.

4.1.1 Computation of the Maximum Radar Cross Section

In order to compute the RCS of the metallic cylinder, the simulation settings are the ones showed 4.6 have been used. The total simulation time is 82s.

The Maximum RCS of the bare cylinder (Fig. 4.7) has an oscillating and increasing behaviour in the considered frequency range (1-8 THz). It starts from -6.5 dB, reaches almost -7 dB in some intermediate frequencies and finally increases up to -5.1 dB. This RCS is translated down of 3 dB in order to create a sort of limit for the maximum RCSs of the cloaked structures: if the last-mentioned ones go down the -3 dB curve for some frequencies, in those frequencies there is the cloaking of the cylinder.

4.1.2 Electric field distribution in the normal plane to the cylinder

The Fig. 4.8 shows the distribution of the electric field in the plane normal to the cylinder ($z = 0$) at 3 THz. It is possible to notice that there is high scattered field due to the metallic object, since the field lines are not straight but very curved. Moreover, there is a very low field just behind the object (shadow cone). This means that the plane wave is highly distorted and, so, that the cylinder is completely visible at the considered frequency. All this can be verified comparing that electric field distribution to the one obtained for the case of cylinder made of vacuum (or no cylinder) (Fig. 4.9). In the last case, the field lines are straight because there is no scattering, since there is no obstacle. Furthermore, behind the cylinder of vacuum there is an high field, just like in front of the cylinder, so the incoming wave is not distorted at all, as it should be.

4.1.3 Study of the RCS computed using a probe behind the cylinder

In order to compute the scattered field, the electric field behind the object is measured using a probe positioned quite far from the cylinder (see Section 7). The simulation settings are the same of the previous cases. Only the number of mesh cells changes slightly (Fig. 4.10). For this configuration the total simulation time is 81s.

The behaviour of the RCS with respect to frequency in the position of the probe is shown in Fig. 4.11. The RCS has an oscillating and, mostly, an increasing behaviour. It is almost the same of

the correspondent Maximum RCS (Fig. 4.7). It will be used in the next to compare this RCS to the one in case of a cloaked structure.

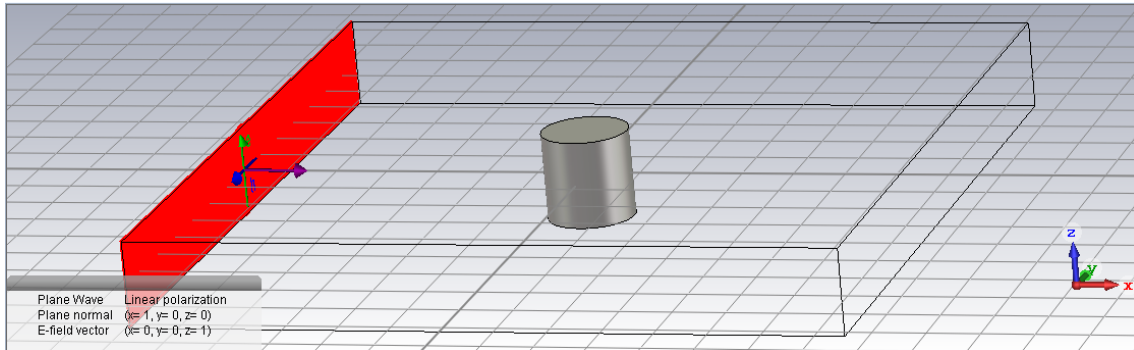


Figure 4.1: CST model of the illumination of a PEC cylinder

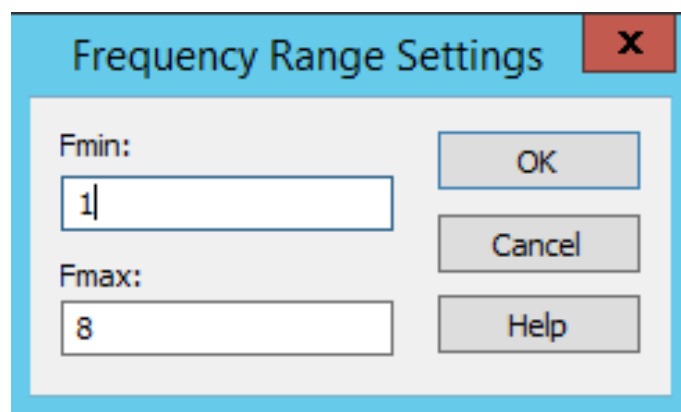


Figure 4.2: Frequency interval set for the simulation of the bare cylinder in CST.

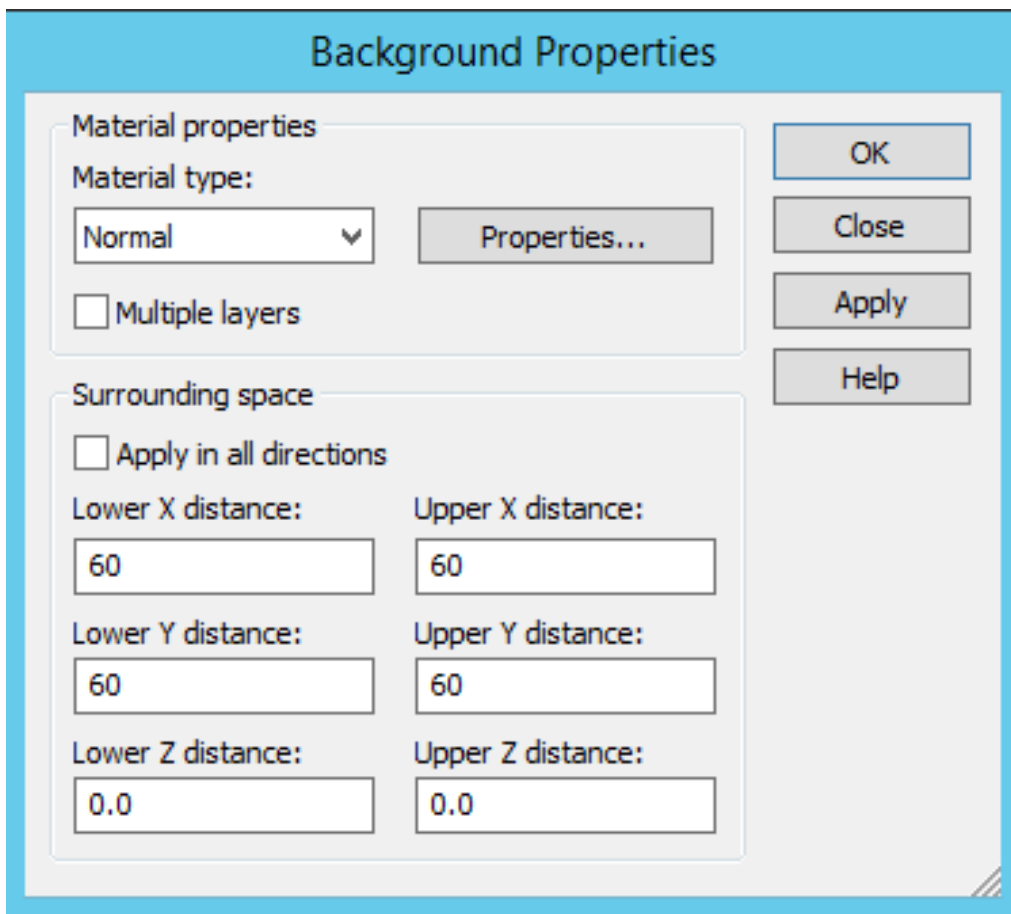


Figure 4.3: Background settings for the simulation of the bare cylinder in CST.

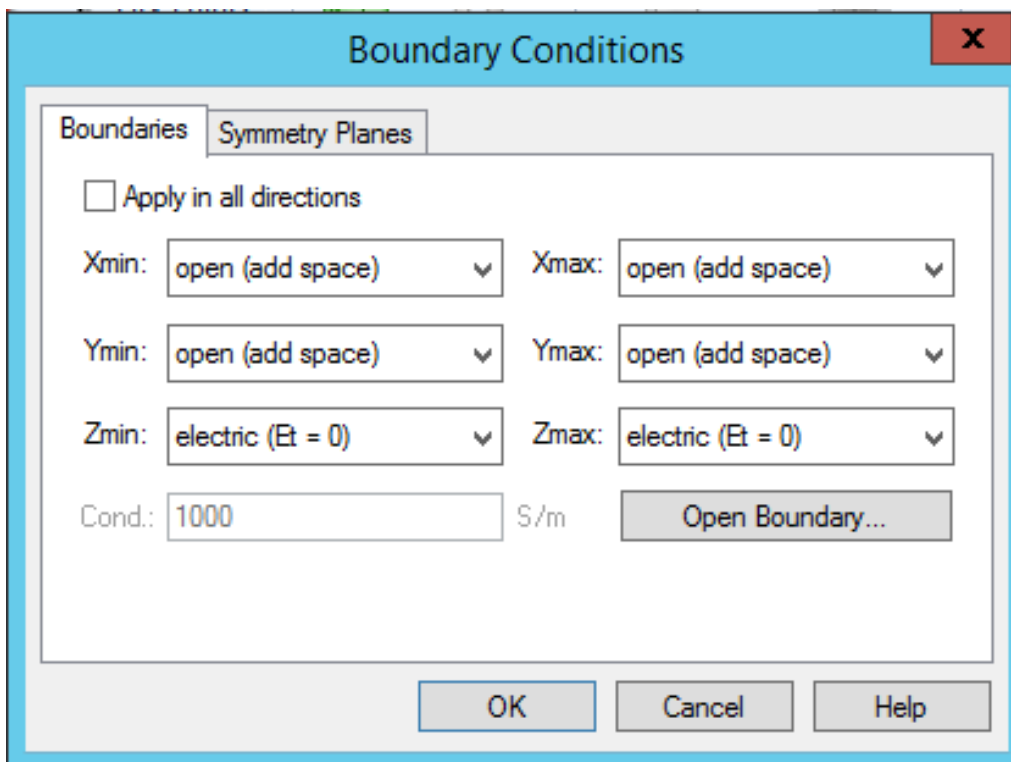


Figure 4.4: Boundary conditions set for the simulation of the bare cylinder in CST.

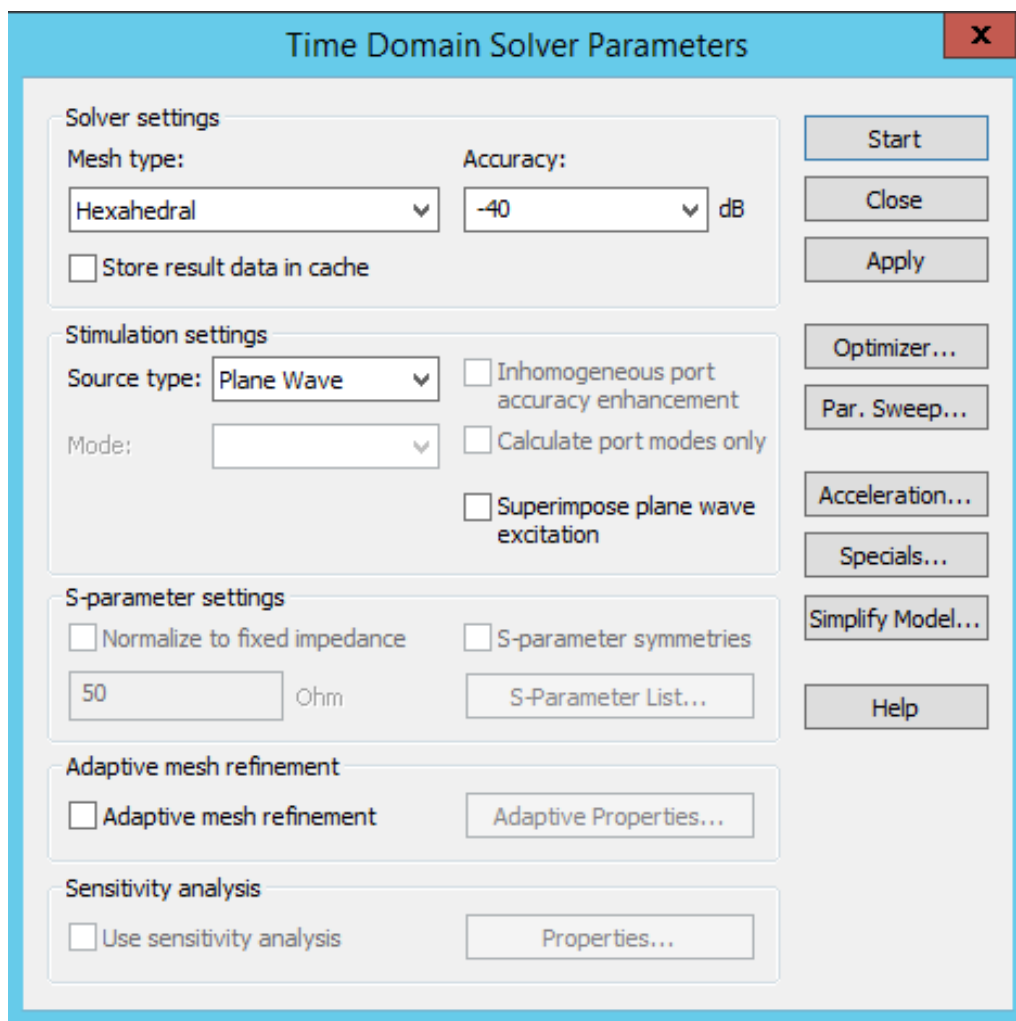


Figure 4.5: Solver settings for the simulation of the bare cylinder in CST.

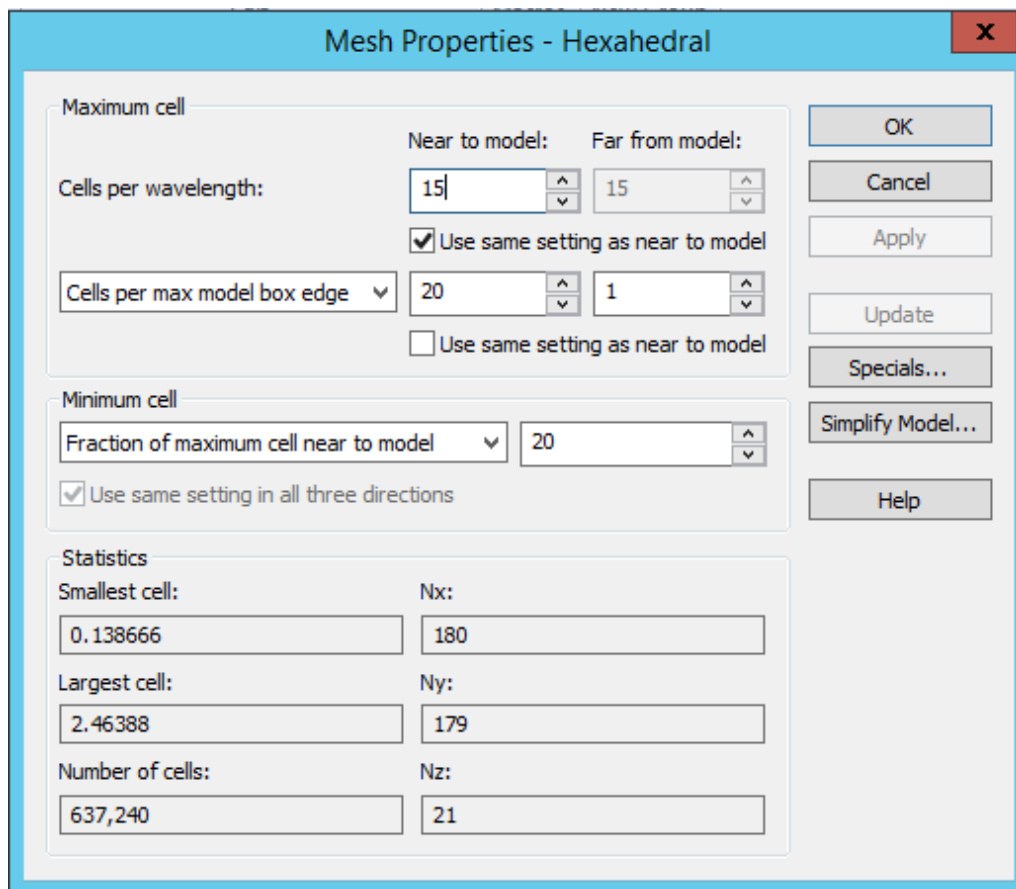


Figure 4.6: Mesh properties and cells statistics set for the simulation of the bare cylinder in CST.

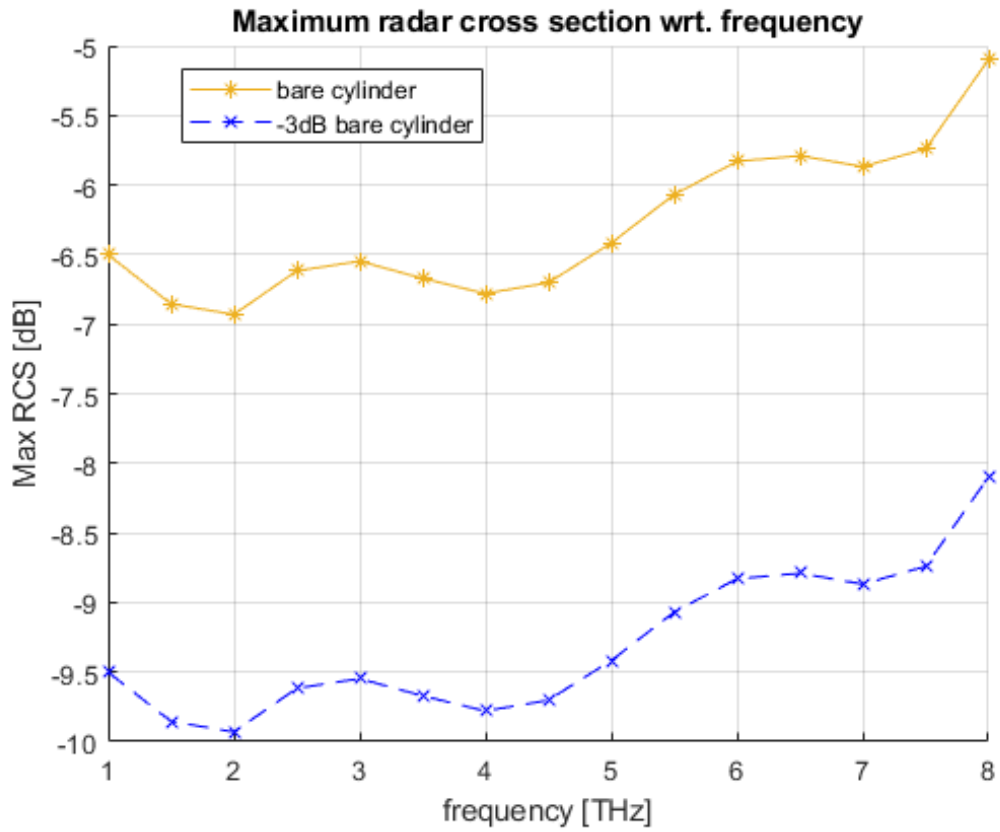


Figure 4.7: Maximum RCS of the bare cylinder and its -3dB- shifted version.

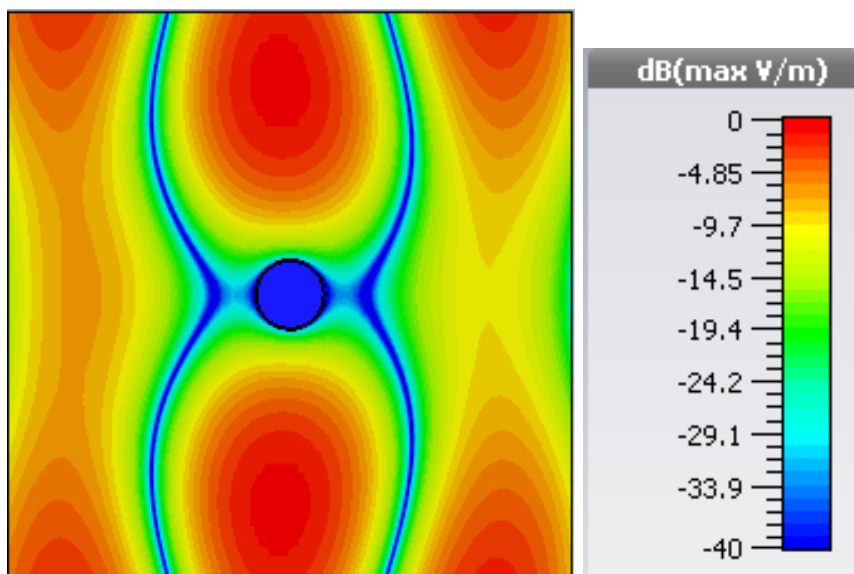


Figure 4.8: Electric field in the plane normal to the cylinder, at 3THz.

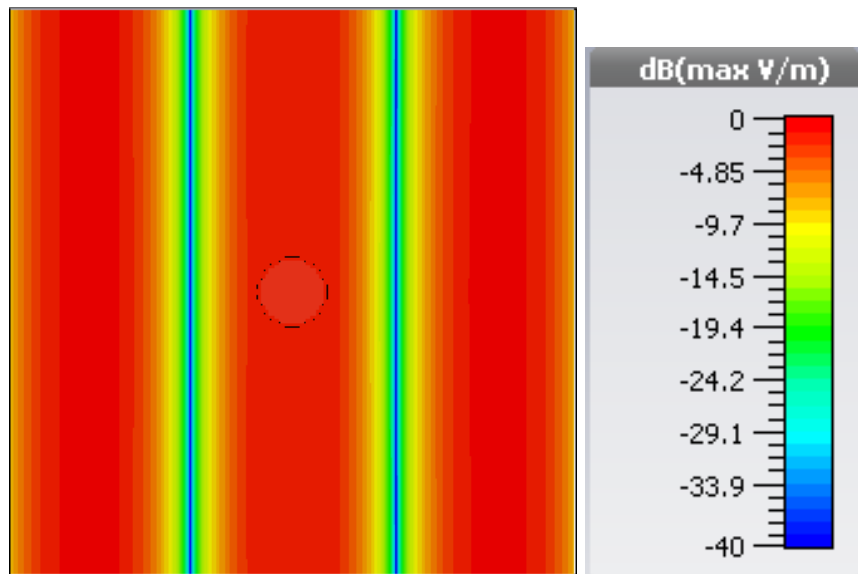


Figure 4.9: Electric field in the plane normal to the cylinder in case of no obstacles, at f_0 .

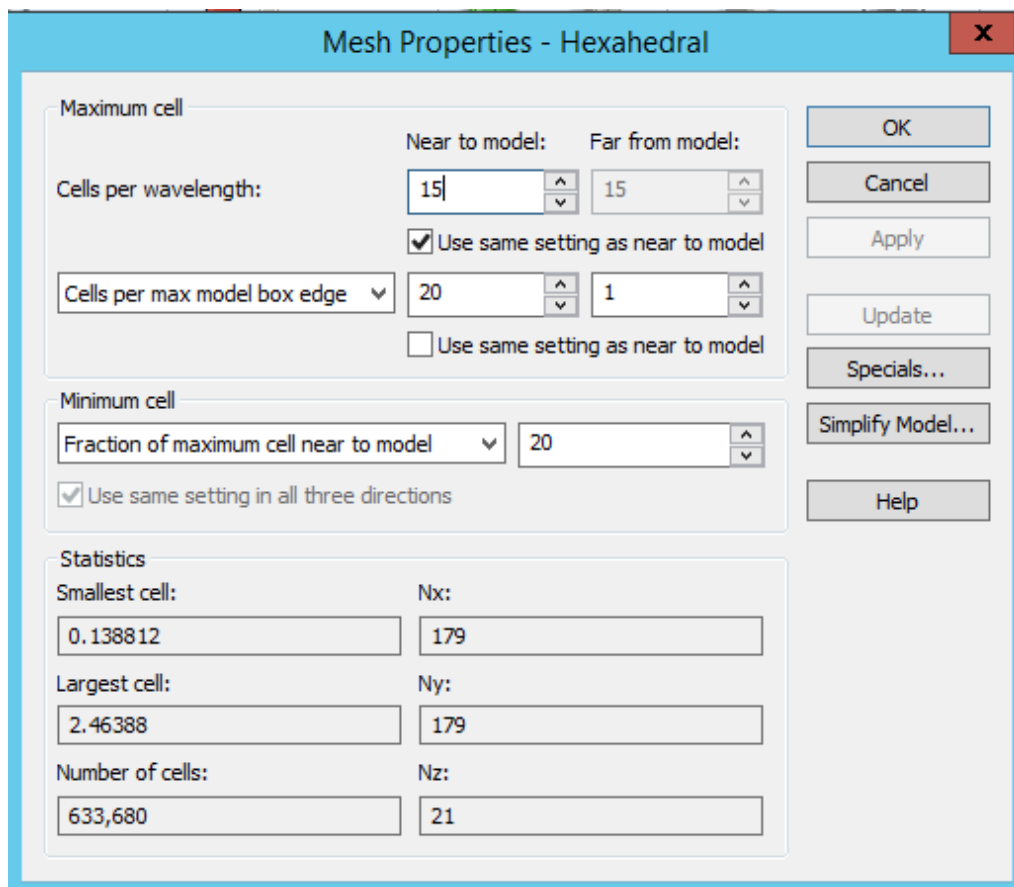


Figure 4.10: Mesh properties and cells statistics set for the simulation of the case of the bare cylinder in CST.

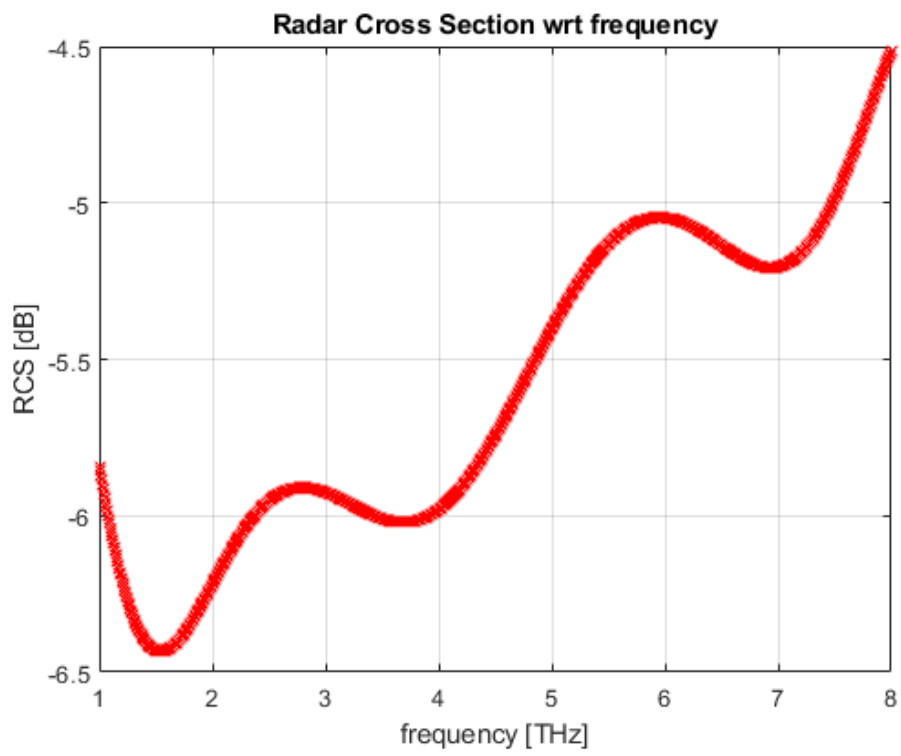


Figure 4.11: RCS for the cylinder of PEC.

4.2 Study to find the cloaking structure dimensions

In this section the thickness of the dielectric and the amplitude of the strips are treated in order to find the best values to reach the cloaking of the considered object. The considered structure is composed of the cylinder made of PEC (with the same dimensions as in Sec. 8), by a dielectric layer (made of Silicon Nitride) that covers perfectly the underlying cylinder and by rectangular and vertical strips (made of graphene at $\mu_c = 0$ eV) a bit shorter than the length of the cylinder of an amount $\delta x = 0.2 \mu\text{m}$ from both the sides.

4.2.1 Thickness of the dielectric

First, the thickness of the dielectric that allows to reach the lowest value of the Maximum RCS is found for a frequency inside the frequency interval 1-8 THz. To do so, the Maximum RCS is computed for the previously discussed structure, varying the thickness of the dielectric. In this case, the number of rectangular strips is fixed to 14 and the width of each of them to $5 \mu\text{m}$. Fig. 4.12 shows the maximum RCS changing the thickness of the dielectric h . It is possible to notice that, increasing h , the minimum of the curves is shifted towards smaller frequencies. At $h = 5.56 \mu\text{m}$, the minimum RCS happens at 6.5 THz; instead for $h = 10.5 \mu\text{m}$ the minimum is located at 3 THz, just the frequency in which the cloaking is wanted.

4.2.2 Width of the rectangular strips

Now, the same structure as before has been adopted, fixing the dielectric thickness to $5.56 \mu\text{m}$ and varying the width of the strips w . As Fig. 4.14 shows, reducing the width the minimum of the Maximum RCS is decreased. Actually, this happens until $w = 1.5 \mu\text{m}$. In fact, at $w = 1 \mu\text{m}$, the minimum is higher than the case with $w = 1.5 \mu\text{m}$.

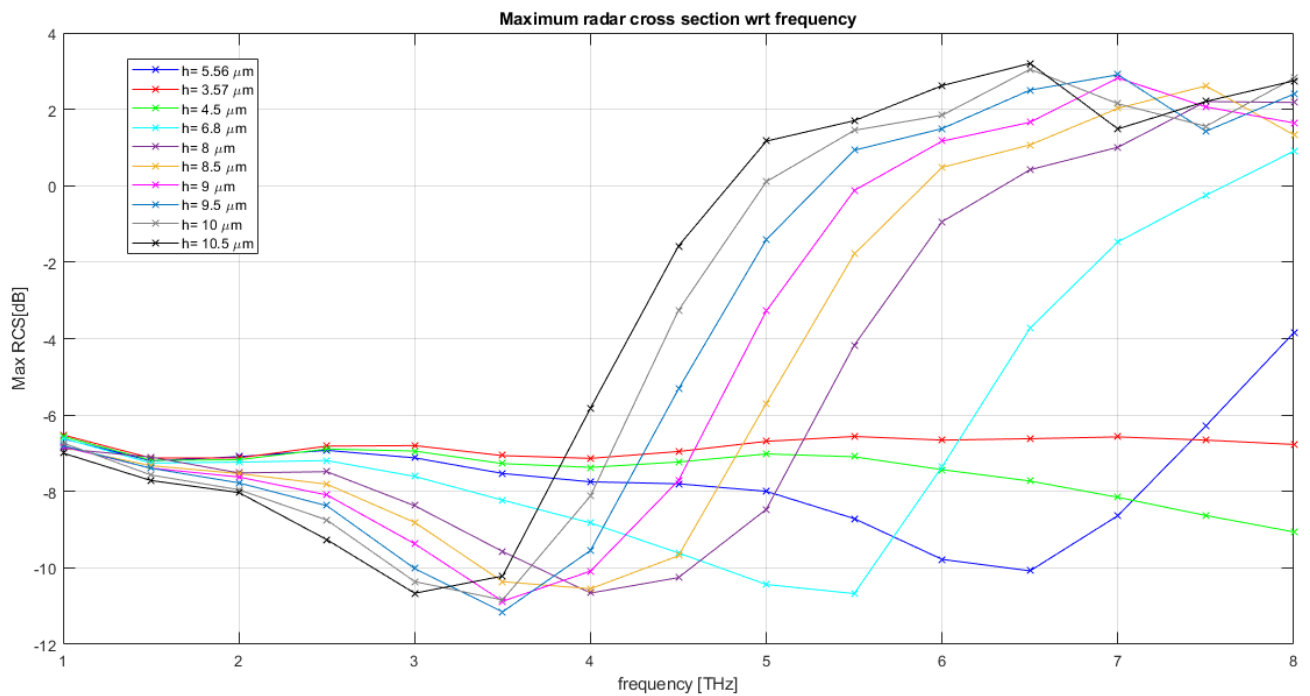


Figure 4.12: Maximum RCS for a cloaking structure with variable dielectric thickness h and rectangular strips of width $5 \mu\text{m}$.

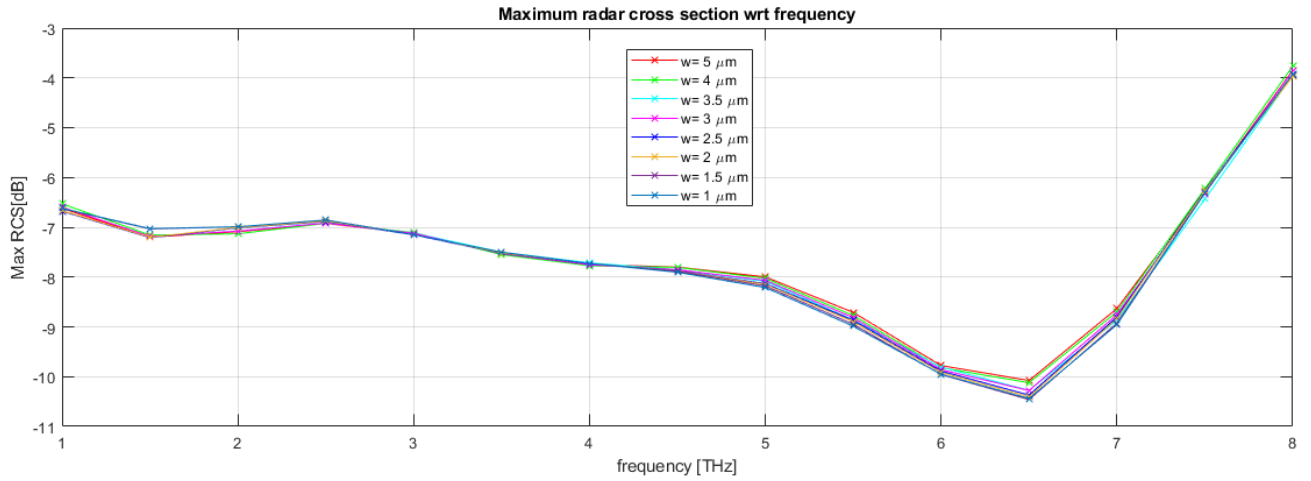


Figure 4.13: Maximum RCS for a cloaking structure with dielectric thickness h $5.56 \mu\text{m}$ and variable rectangular strips width.

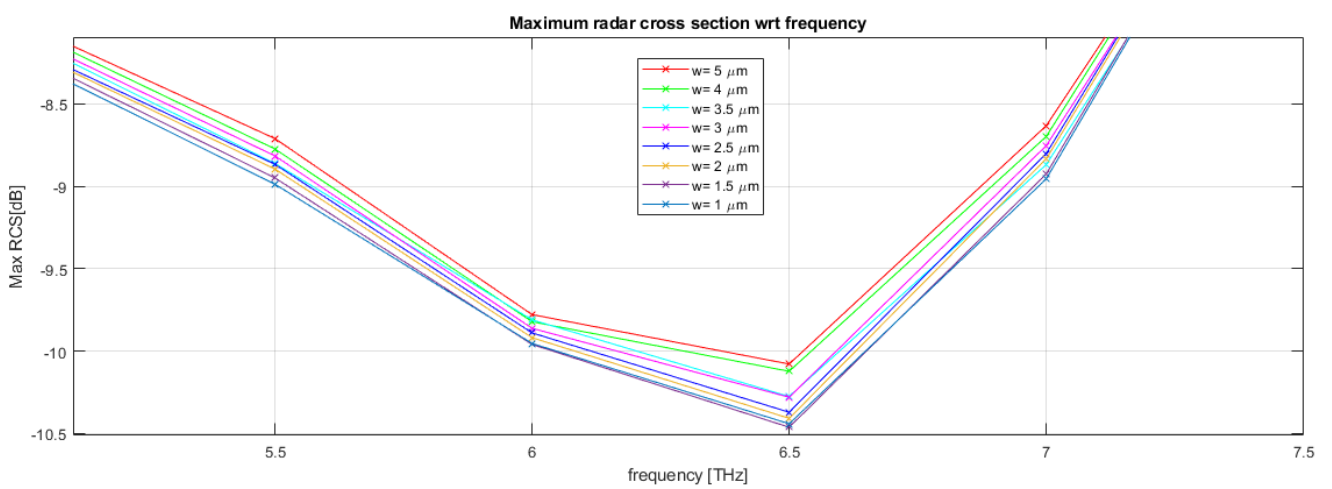


Figure 4.14: Zoom around the minimum of the curves of Fig. 4.13.

4.3 Study of the behaviour of cloaked cylinder with rectangular strips

As the next step, the structure considered in the previous Section is simulated, fixing $w = 1.5 \mu\text{m}$ and $h = 5.56 \mu\text{m}$ ($\lambda_0/17.99$ in terms of wavelength) (Fig. 4.15). Figure 4.16 highlights the spacing left from both sides of the dielectric layer for the extension of the vertical strips. This little spacing is needed in order to get correct results during the simulation on CST. In fact, the boundary conditions in the z direction (the one parallel to the axis of the cylinder) are set to *electric* in order to extend the length of the coated cylinder infinitely. If no spacing is left between the borders of the dielectric layer and the ones of the strips, the *electric* boundary condition would generate a short circuit. This spacing does not break the continuity among the strips and the upper and latter ones (generated by the set boundary conditions) because a capacity is generated in the space among two strips in the z direction (Fig. 4.17). The δx of the figure corresponds to $0.4 \mu\text{m}$ in the simulated case. This trick is adopted also for the modulated strips, that are treated in the following Sections.

4.3.1 Computation of the Maximum Radar Cross Section

For the computation of the Maximum RCS of the considered structure, settings for the simulation of the bare cylinder have been adopted. Mesh properties are shown in Fig. 4.18. The total simulation time varies slightly with the chemical potential, but they are all around 215 s.

Graph of Fig. 4.19 shows the variation of the Maximum RCS increasing the chemical potential. It is worth noticing that, raising μ_c , the minimum of the RCS curve is shifted towards right and also that its value is increased, implying the reduction of the cloaking bandwidth. Table 4.1 lists the frequencies of the minima of the curves and the cloaking bandwidths for each chemical potential. The bandwidth reduces a lot from 0 eV to 1 eV. As regards f_0 , it varies from 6.5 THz to 7 THz.

4.3.2 Electric field distribution in the normal plane to the cylinder

For sake of brevity, only the cases with $\mu_c = 0$ eV and 1 eV are considered for the electric field distribution. Figures 4.20 and 4.21 show the field distributions at 6.5 THz. At $\mu_c = 0$ eV, the field behind the cloaked object is practically identical to the one in front of it. This behaviour reflects the one of the correspondent Maximum RCS, that is cloaked at that frequency. Instead, as regard the following figure (Fig. 4.21), the field behind the cloaked cylinder is less than the one in front of it. In fact, at $\mu_c = 1$ eV, the Maximum RCS curve shows that there is no cloaking of the cylinder at that frequency.

At 7 THz, instead both the cases ($\mu_c = 0$ eV and $\mu_c = 1$ eV) are cloaked. In case of chemical potential 0 eV, there is a little bit more field behind the cloaking structure with respect to in front of it (Fig. 4.22). In the other case, indeed, there is a bit less field (about -5 dB) just behind it (Fig. 4.23). Comparing the fields of the structures at their cloaking frequency (Figs. 4.20 and 4.23) with the fields in case of bare cylinder at the same frequencies (Figs. 4.24 and 4.25), it is possible to notice that in the cloaking cases there is less scattered field and also more field behind the object with respect to the case of the bare cylinder.

4.3.3 Study of the RCS computed using a probe behind the cylinder

The RCSs computed using the probe (Figs. 4.26 and 4.27), so considering only a point behind the object, are, also in this case, quite similar to the respective Maximum RCSs (computed taking into account the points of a circumference around the object). So the cloaking bandwidths are quite similar to those listed in the table 4.1: for $\mu_c = 0$ eV, BW = 1.498 THz (vs. 1.45 THz of the one of the table); instead, for $\mu_c = 1$ eV, BW = 0.343 THz (vs. 0.299 THz). Actually, in Fig. 4.26, the minimum of the curve happens at $f_0 = 6.36$ THz, while in the curve representing the Maximum RCS of the same structure f_0 corresponds to 6.5 THz. Besides, both curves show a bit higher values (of an amount of about 0.6 dB). The bandwidth enlargement and the shift of the cloaking frequency may be only apparent and due to the higher accuracy of the calculation of the RCS using a probe. In fact when a probe is adopted, the electric field is measured in a large amount of frequency points, so the RCS computation is accurate at more frequencies. Instead, to compute the Maximum RCS it is necessary to set a field monitor on CST for each wanted frequency, so, in

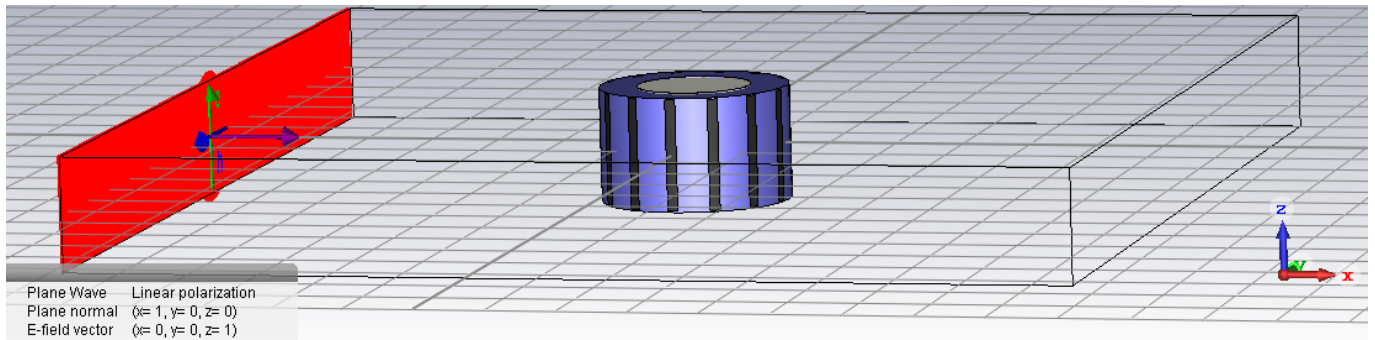


Figure 4.15: Cloaked cylinder with a dielectric of $h= 5.56 \mu\text{m}$ and 14 rectangular strips.

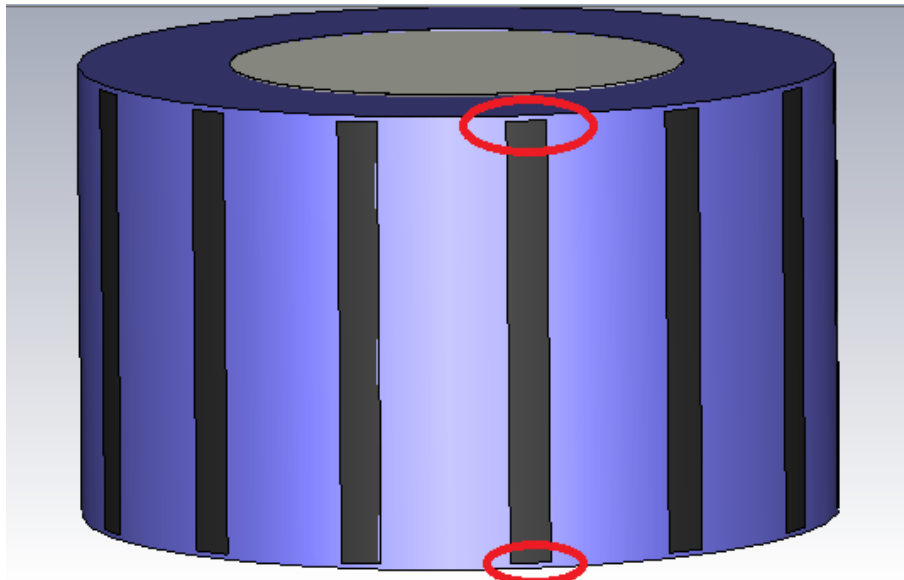


Figure 4.16: Cloaked cylinder of Fig. 4.15 with underlined spacing of the strips.

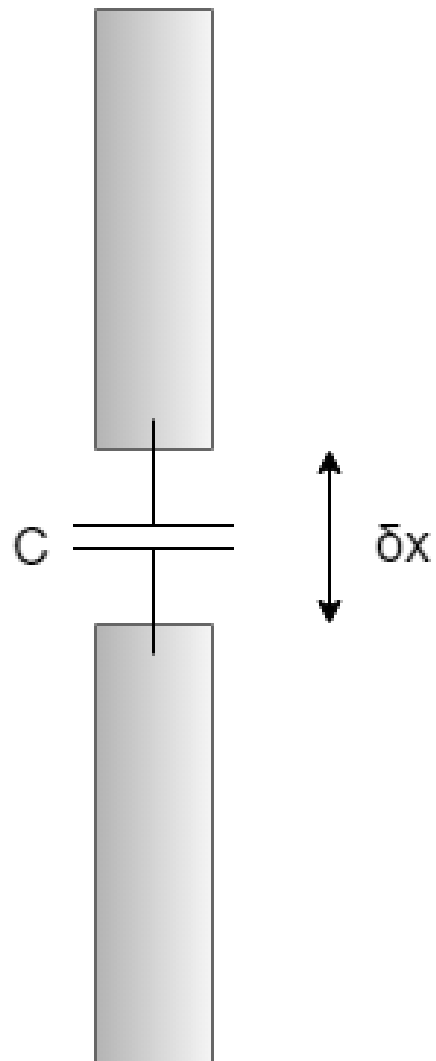


Figure 4.17: Rectangular strips separated by a spacing δx where a capacity is generated.

order to reduce simulation times and computation complexity, less frequency points are considered and, accordingly, less accuracy is obtained in the graph. This discussion is also valid for the next considered cases.

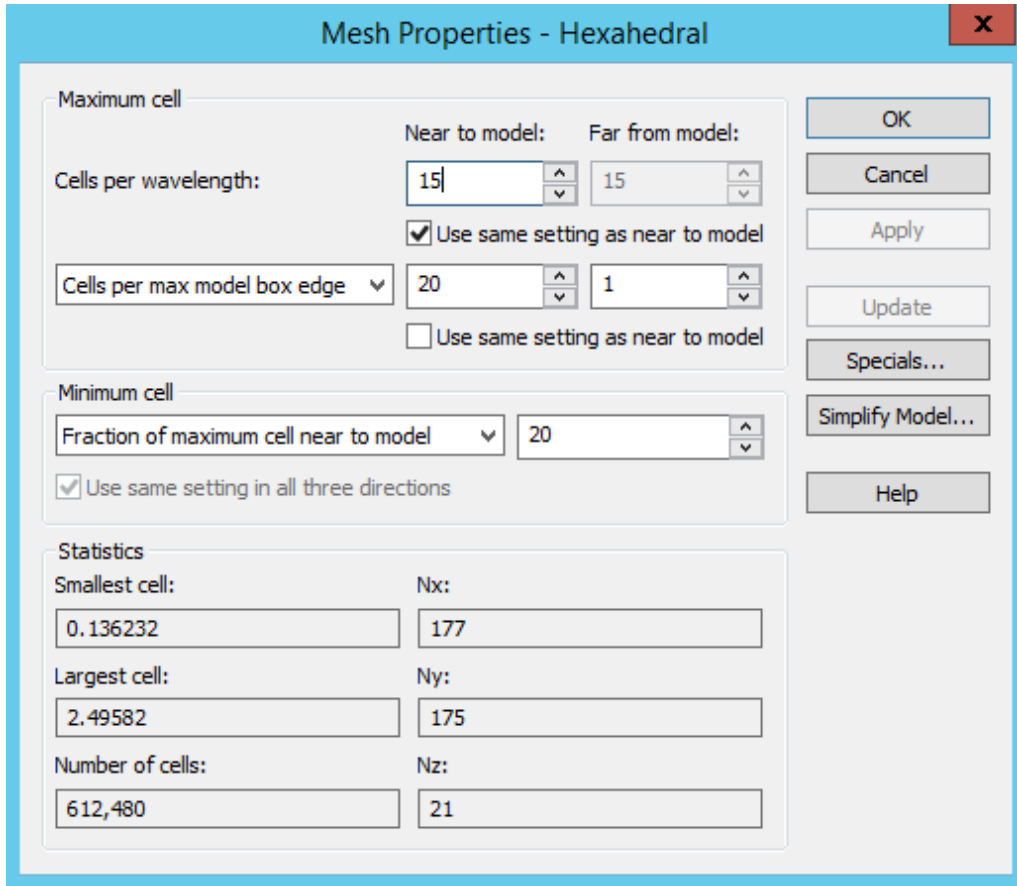


Figure 4.18: Mesh properties and cells statistics set for the simulation of the cloaking structure of Fig. 4.15 in CST.

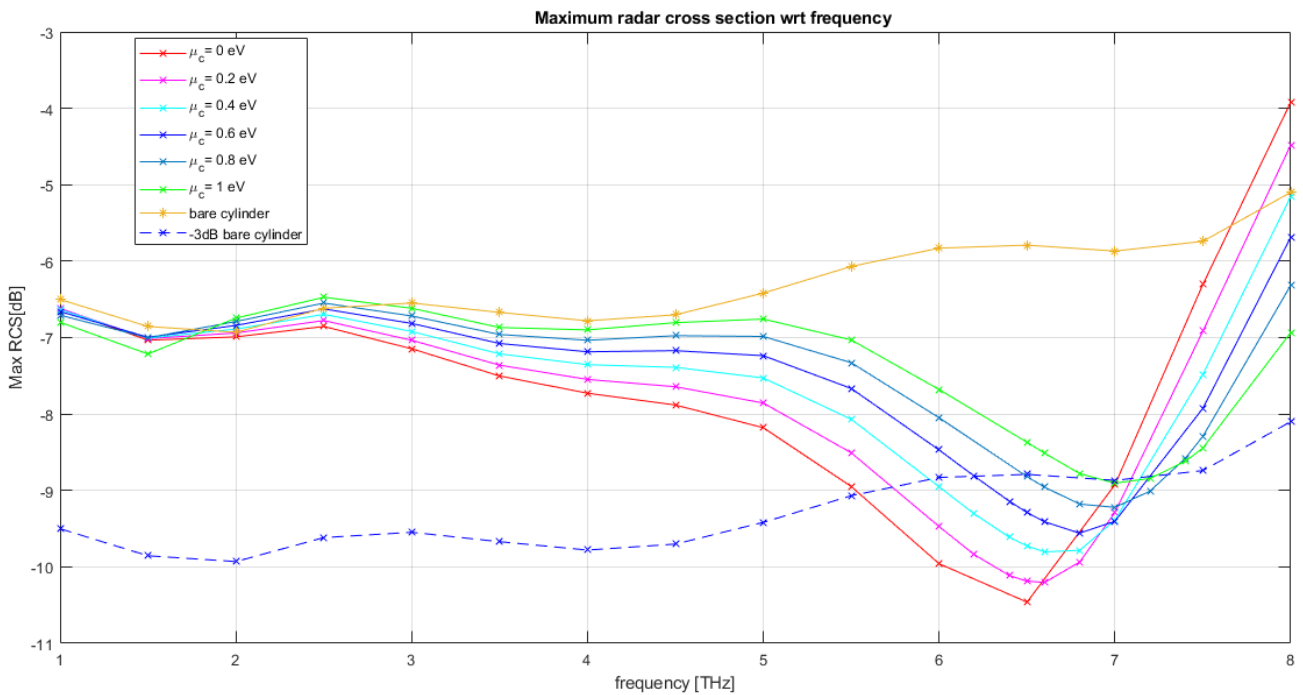
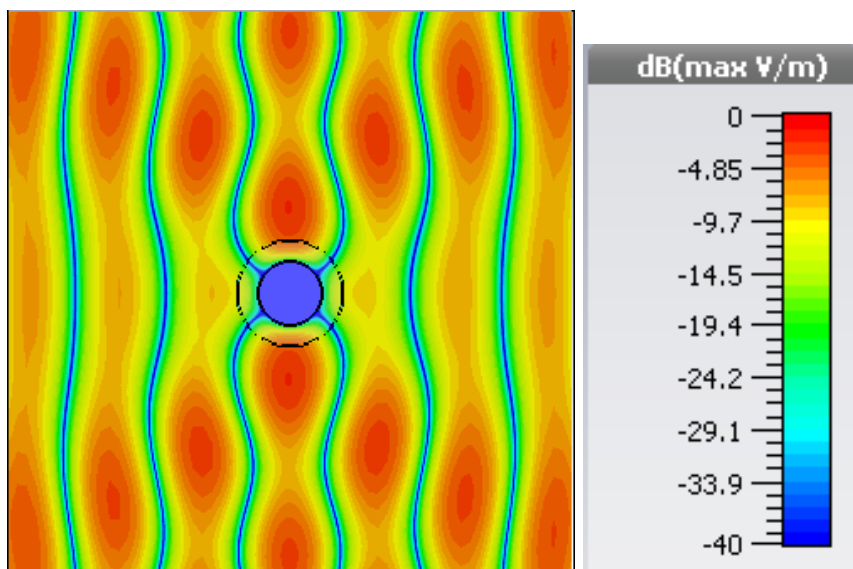


Figure 4.19: Maximum RCS for the cloaking structure with $h=5.56 \mu\text{m}$ and rectangular strips $w=1.5 \mu\text{m}$ varying the chemical potential μ_c .

Table 4.1: Minimum frequencies and the bandwidths of the Maximum RCS curves of Fig. 4.19 changing the chemical potential μ_c .

μ_c [eV]	f_0 [THz]	BW [THz]
0	6.5	1.45
0.2	6.6	1.349
0.4	6.6	1.184
0.6	6.8	0.983
0.8	7	0.804
1	7	0.299

Figure 4.20: Electric field in the plane normal to the cloaked cylinder (with rectangular strips with $\mu_c=0$ eV), at 6.5 THz.

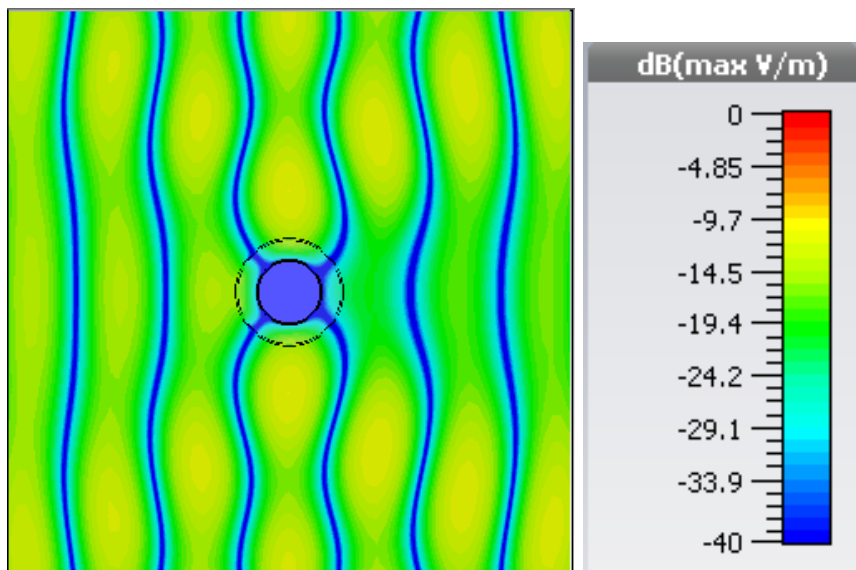


Figure 4.21: Electric field in the plane normal to the cloaked cylinder (with rectangular strips with $\mu_c=1$ eV), at 6.5 THz.

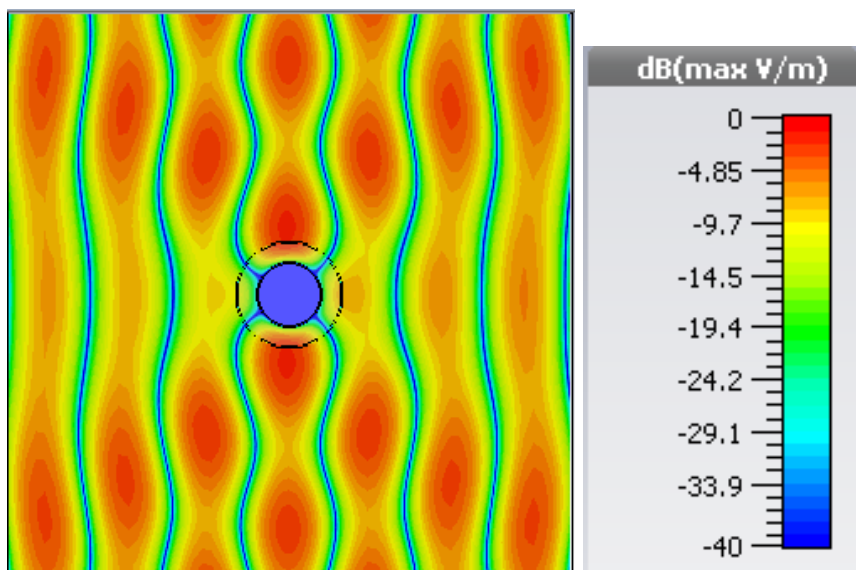


Figure 4.22: Electric field in the plane normal to the cloaked cylinder (with rectangular strips with $\mu_c=0$ eV), at 7 THz.

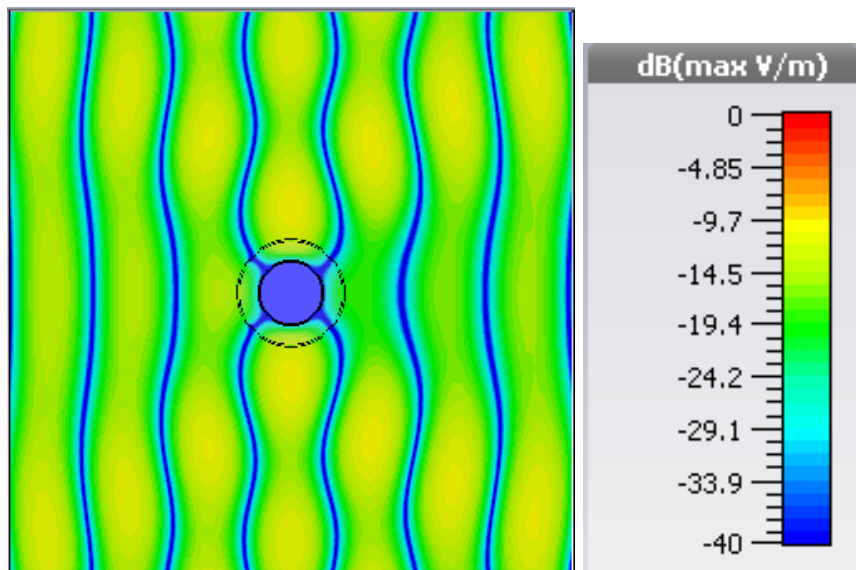


Figure 4.23: Electric field in the plane normal to the cloaked cylinder (with rectangular strips with $\mu_c=1$ eV), at 7 THz.

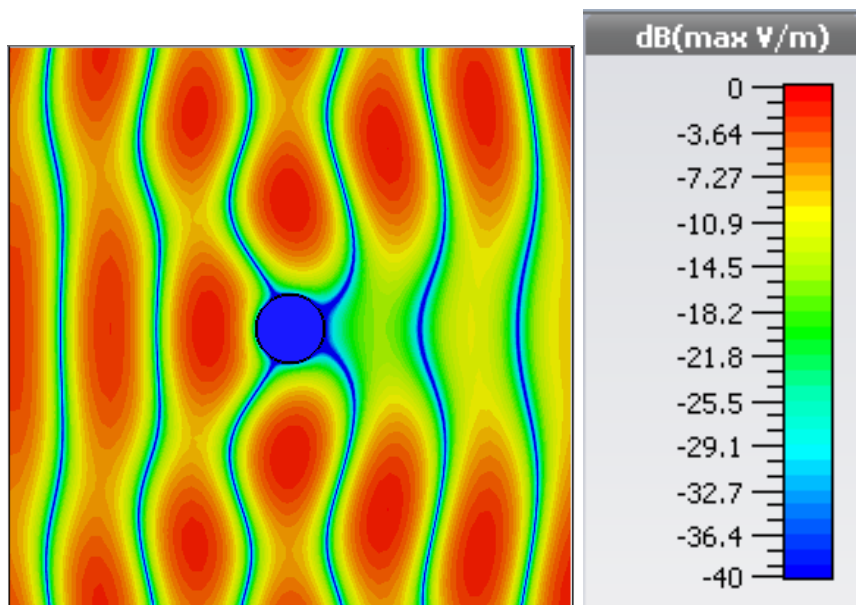


Figure 4.24: Electric field in the plane normal to the bare cylinder, at 6.5THz.

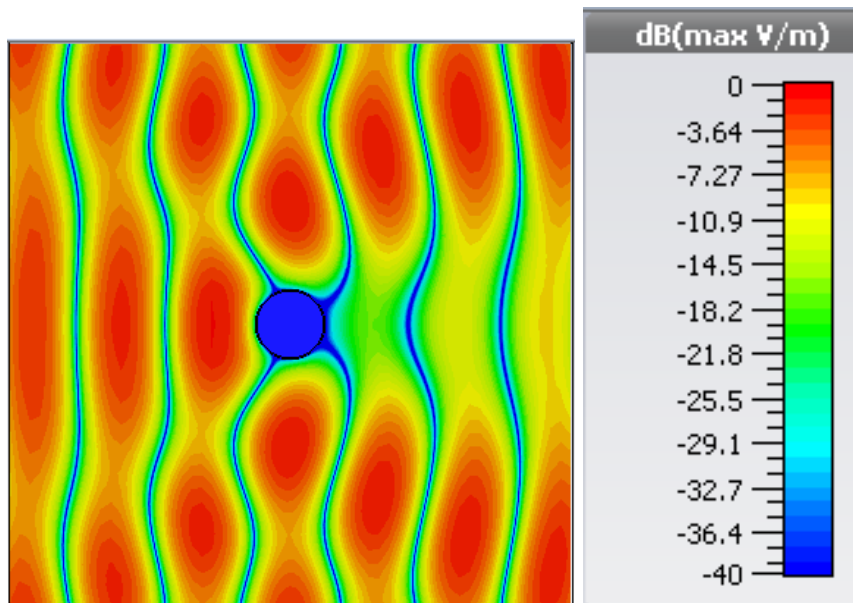


Figure 4.25: Electric field in the plane normal to the bare cylinder, at 7THz

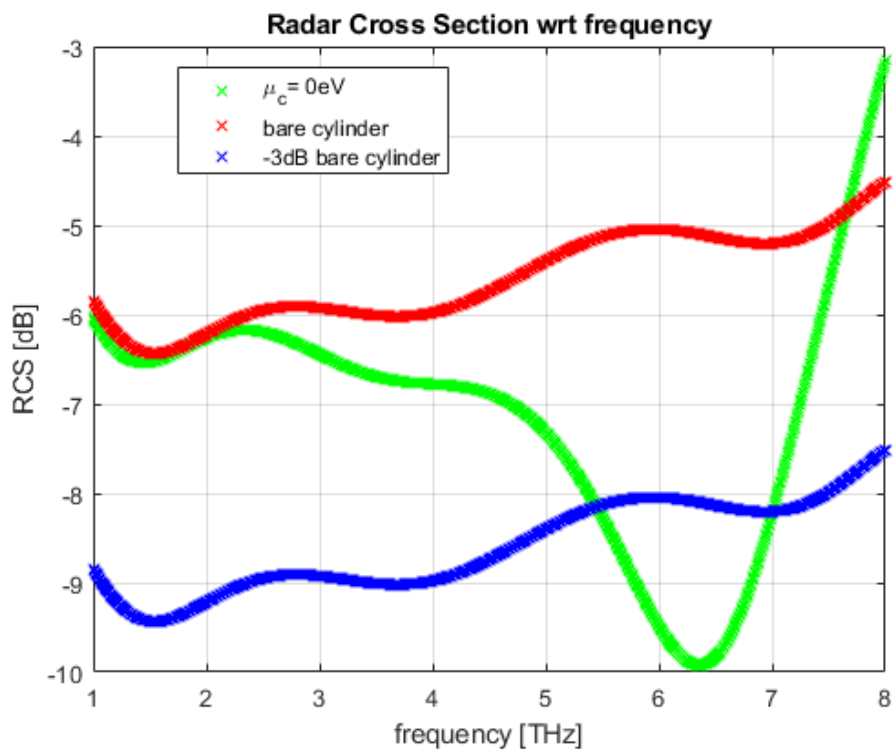


Figure 4.26: RCS in case of the cloaked structure of Fig. 4.15 where all the strips are made of graphene with $\mu_c = 0\text{ eV}$, compared to the RCS of the bare cylinder.

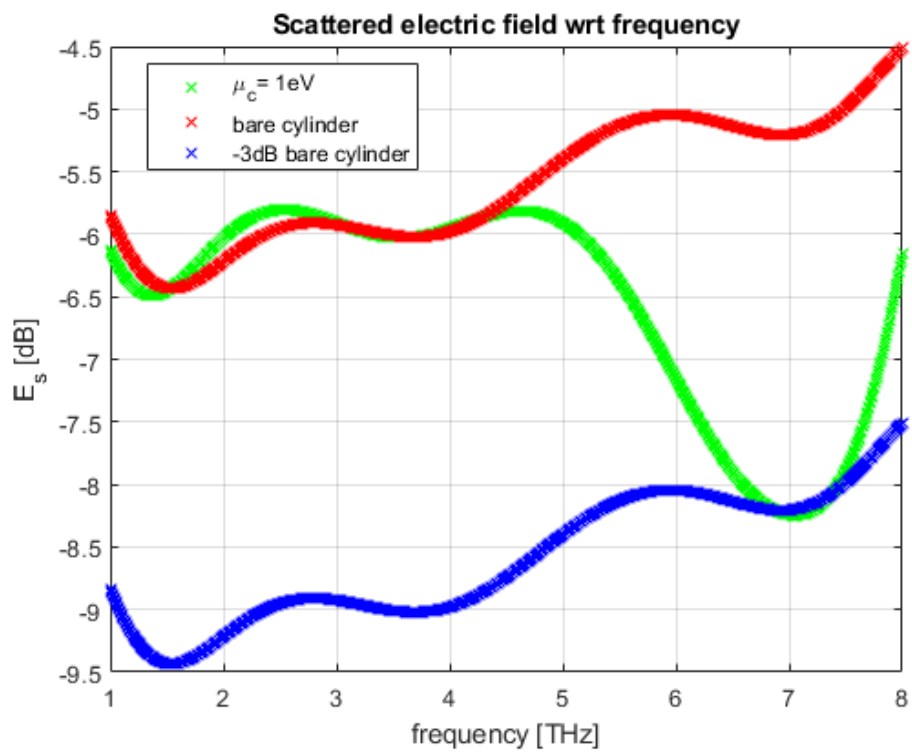


Figure 4.27: RCS in case of the cloaked structure of Fig. 4.15 where the strips are made of graphene with $\mu_c = 1\text{ eV}$, compared to the RCS of the bare cylinder.

4.4 Study of the behaviour of cloaked cylinder with modulated strips of maximum amplitude $1.5 \mu\text{m}$

In the following study the previous structure is adopted, but now, the vertical strips are modulated with a shape of sinusoidal type (Fig. 4.28) in order to reach a maximum amplitude $w = 1.5 \mu\text{m}$ (that happens at the center of the strips). The minimum amplitude of each strip, instead, is $w_{\min} = 0.5 \mu\text{m}$ (that corresponds to the extremities of the strips). The spacing among the border of the dielectric layer and the one of the strips is maintained. This choice has been adopted to avoid discontinuities at the unit cell borders ([?]).

4.4.1 Computation of the Maximum Radar Cross Section

The simulation settings to compute the electric field and the Maximum RCS are the same as before. Only the number of mesh cells changes: in Fig. 4.29 it is possible to notice that the number of mesh cells is significantly increased with respect to the previous case. Besides, here the number of cells has a small variation changing the chemical potential. The total simulation time is around 960 s for the simulations where only μ_c of the strips is changed. The behaviour of the Maximum RCS varying the chemical potential is similar to the previous case (with rectangular strips): there is the reduction of cloaking bandwidth and the shift towards right of the minimum of the curve increasing μ_c (Fig. 4.30). But looking at the table 4.2, it is possible to notice that in this case the shift of the minimum is smaller, since at $\mu_c = 1 \text{ eV}$ f_0 corresponds to 6.8 THz (while in the previous case it was 7 THz). Moreover, the cloaking bandwidth at high chemical potentials is wider than the case with the rectangular strips: at 1 eV, the bandwidth is 0.956 THz, while before it was 0.299 THz.

4.4.2 Electric field distribution in the normal plane to the cylinder

The electric field distribution is similar to the one of the previous structure (Section 10). In case of $\mu_c = 0 \text{ eV}$ the field behind the object is identical to the one in front of it, at its correspondent f_0 (6.5 THz) (Fig. 4.31); as regards the structure with $\mu_c = 1 \text{ eV}$ (Fig. 4.32), instead, the field after the cloaked cylinder is a bit less than before it at its cloaking frequency, as for the structure with rectangular strips.

4.4.3 Study of the RCS computed using a probe behind the cylinder

Also for this structure, the RCS (Fig. 4.33 and Fig. 4.34) have the same behaviour of the correspondent Maximum RCSs. There is only a reduced shift upwards of the curves and a small enlargement of the cloaking bandwidths (for $\mu_c = 0 \text{ eV}$, $B = 1.498 \text{ THz}$, while for $\mu_c = 1 \text{ eV}$, $BW = 1.064 \text{ THz}$). There is also a small shift of the f_0 , especially in case of $\mu_c = 0$: in this case, the cloaking frequency becomes 6.35 THz.

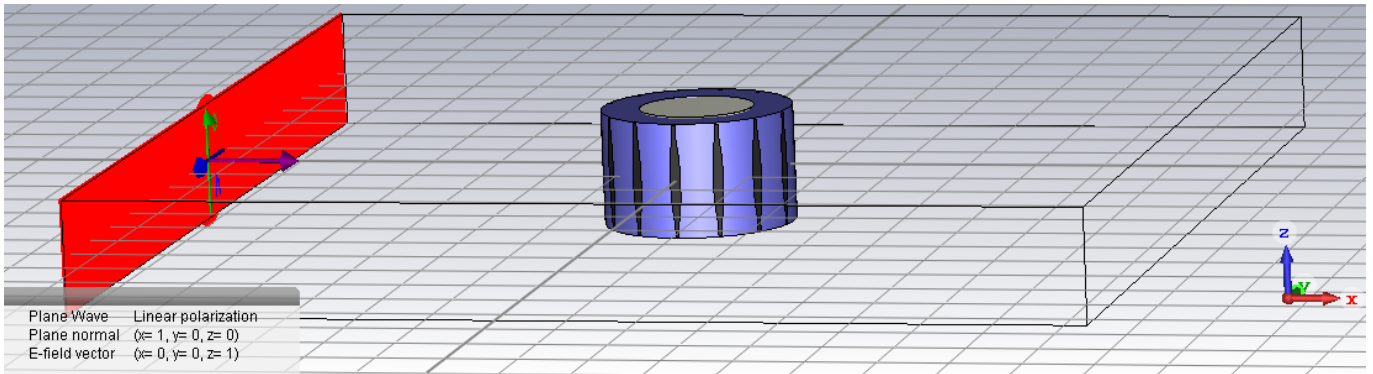


Figure 4.28: Cloaked cylinder with a dielectric of $h=5.56 \mu\text{m}$ and 14 modulated strips with maximum amplitude $1.5 \mu\text{m}$.

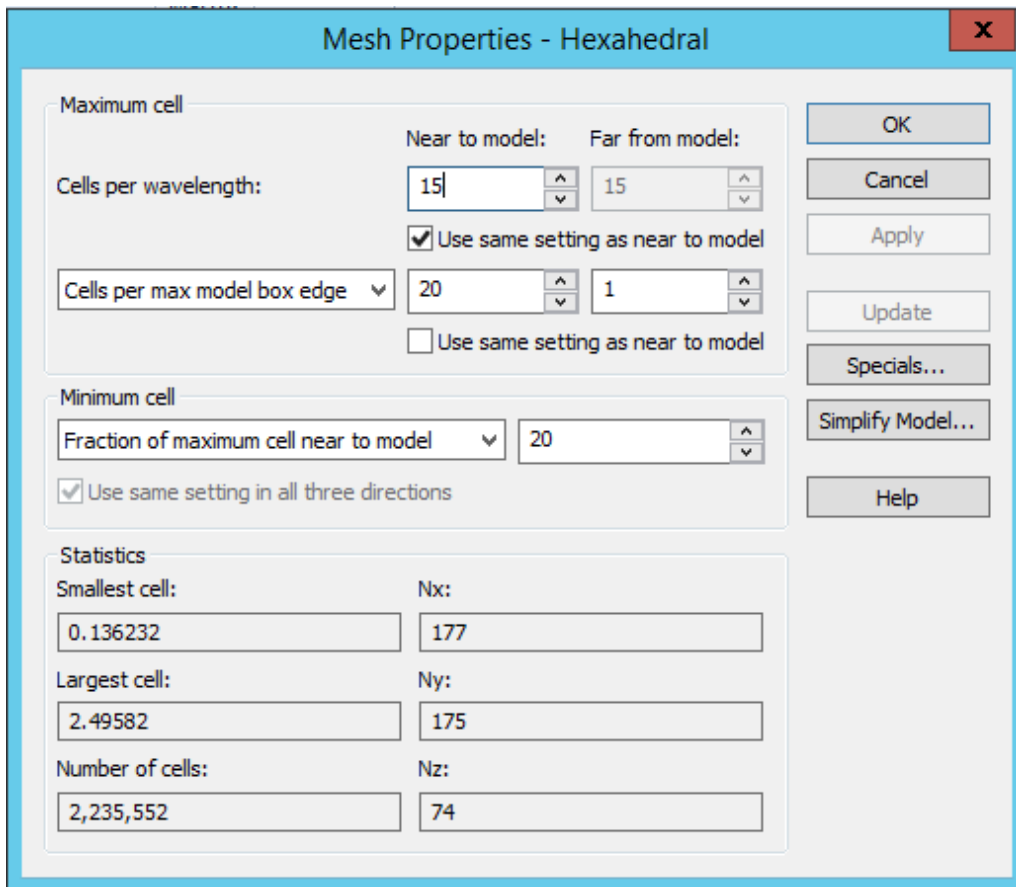


Figure 4.29: Mesh properties and cells statistics set for the simulation of the cloaking structure of Fig. 4.28 with $\mu_c = 0 \text{ eV}$ in CST.

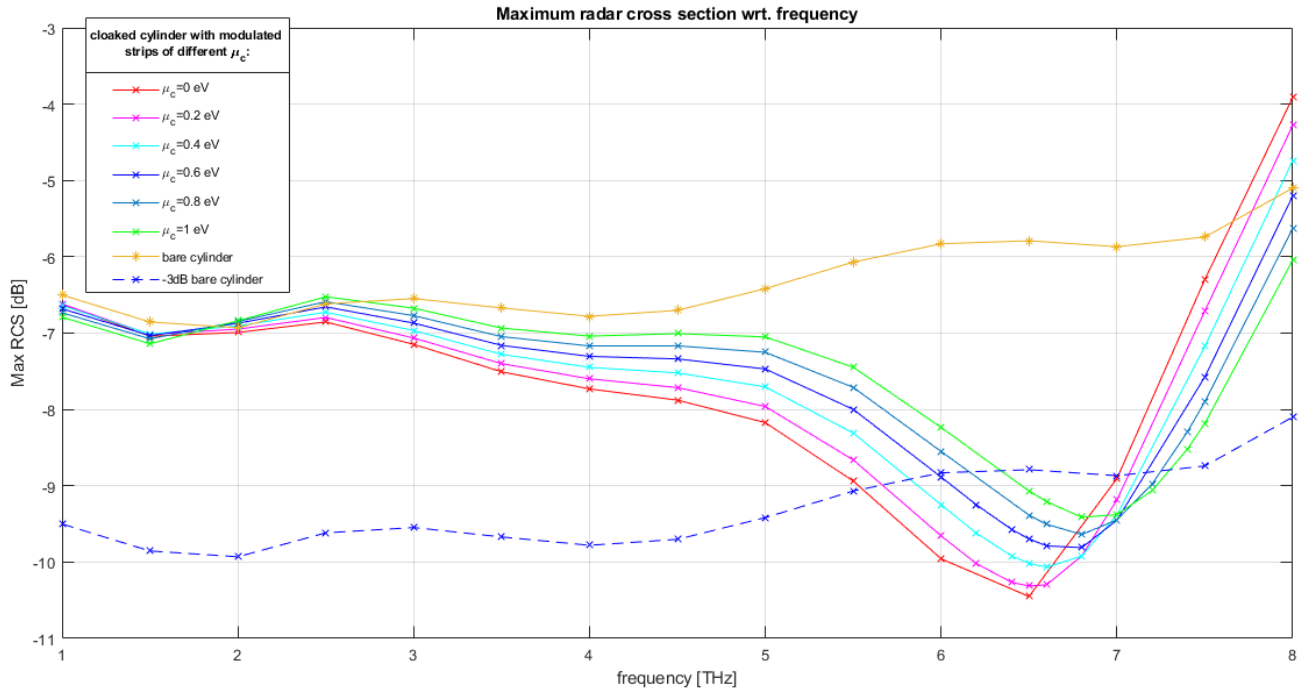


Figure 4.30: Maximum RCS for the cloaking structure with $h = 5.56 \mu\text{m}$ and modulated strips with maximum amplitude $w = 1.5 \mu\text{m}$, varying the chemical potential μ_c .

Table 4.2: Minimum frequencies and the bandwidths of the Maximum RCS curves of Fig. 4.30 changing the chemical potential μ_c .

μ_c [eV]	f_0 [THz]	BW [THz]
0	6.5	1.456
0.2	6.5	1.399
0.4	6.6	1.3
0.6	6.8	1.188
0.8	6.8	1.088
1	6.8	0.956

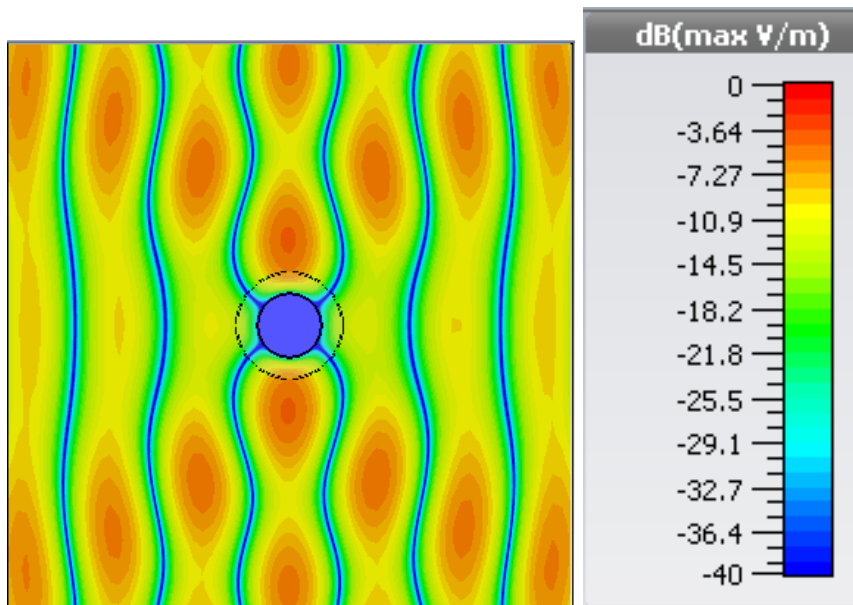


Figure 4.31: Electric field in the plane normal to the cloaked cylinder of Fig. 4.28 with $\mu_c = 0$ eV, at 6.5 THz.

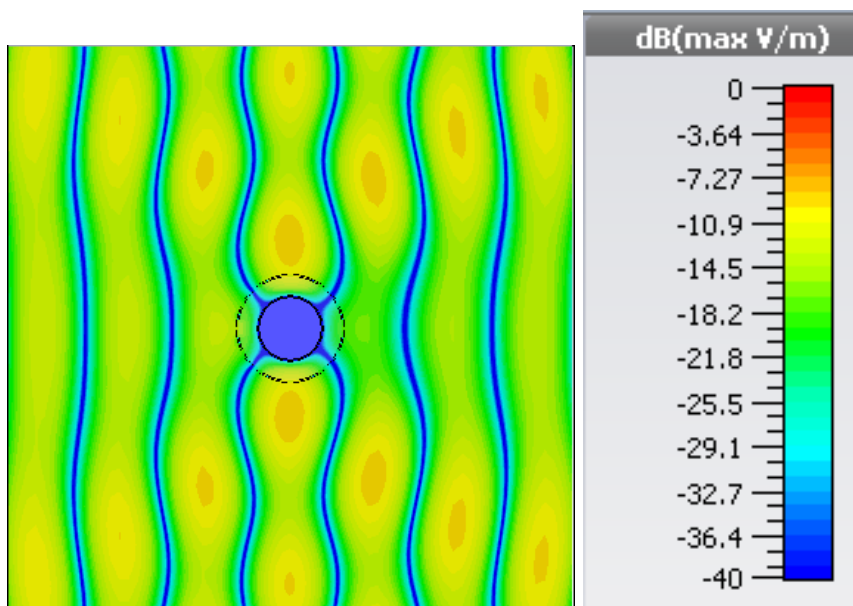


Figure 4.32: Electric field in the plane normal to the cloaked cylinder of Fig. 4.28 with $\mu_c = 1$ eV, at 6.8 THz

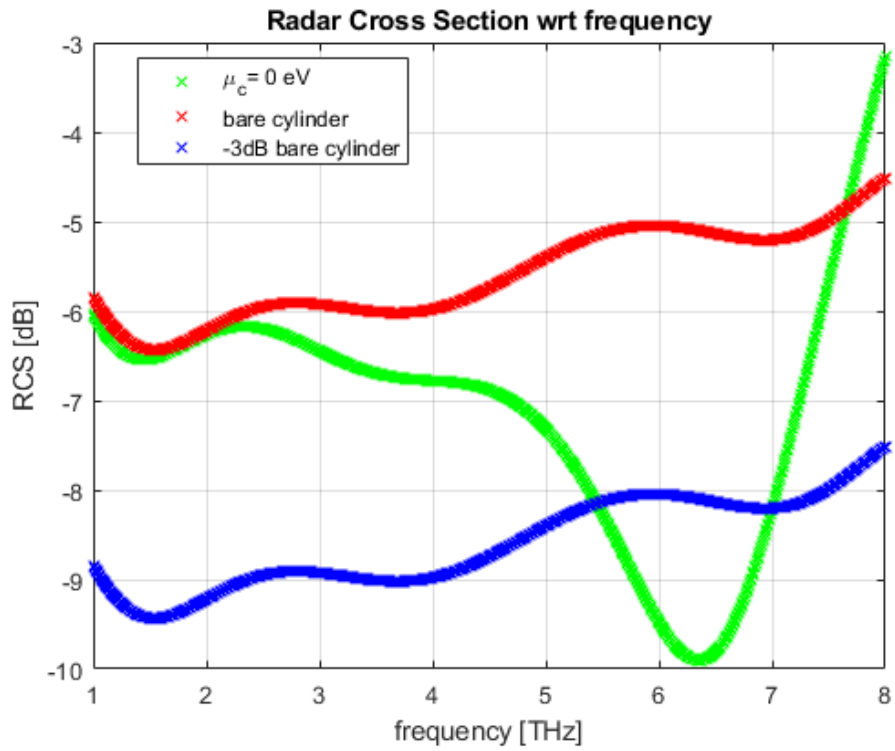


Figure 4.33: RCS in case of the cloaked structure of Fig. 4.28 where the strips are made of graphene with $\mu_c = 0$ eV, compared to the RCS of the bare cylinder.

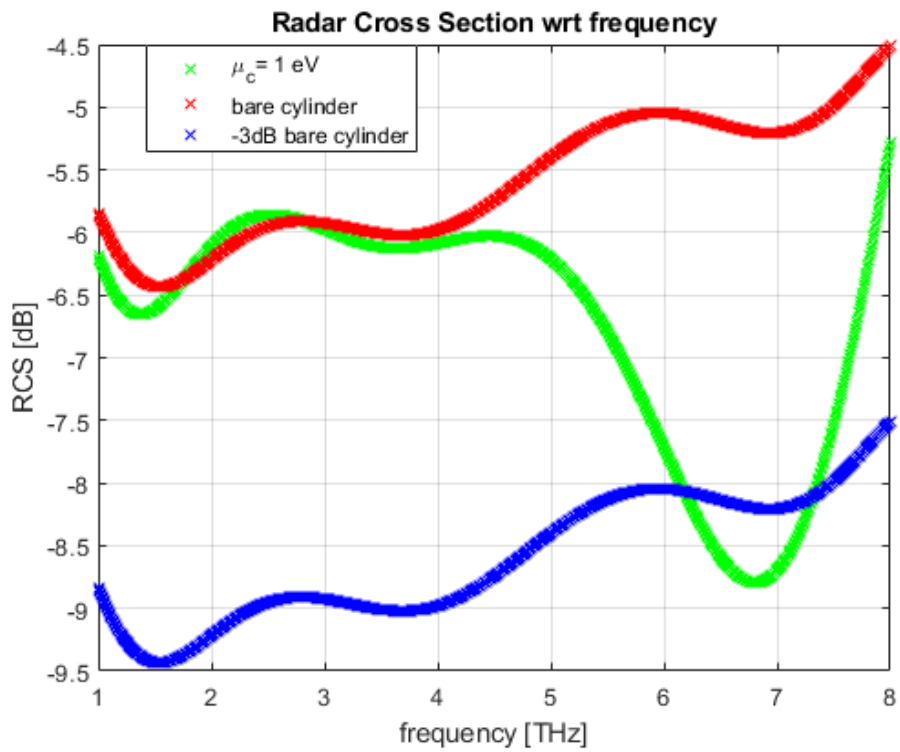


Figure 4.34: RCS in case of the cloaked structure of Fig. 4.28 where the strip are made of graphene with $\mu_c = 1$ eV, compared to the RCS of the bare cylinder.

4.5 Study of the behaviour of cloaked cylinder with modulated strips of mean amplitude $1.5 \mu\text{m}$

Now, the amplitude of the modulated strips is increased a bit in order to reach a mean amplitude equal to $1.5 \mu\text{m}$ (Fig. 4.35). The minimum amplitude of the strips remains $0.5 \mu\text{m}$ while the maximum amplitude becomes $2.5 \mu\text{m}$.

4.5.1 Computation of the Maximum Radar Cross Section

The simulation settings are the same of the previous cases (Sec. 4.3 and 4.4), but the number of mesh cells changes using this structure (Fig. 4.36); instead, varying μ_c the number of mesh cells doesn't change in this case. The total simulation time varies a bit according to the chemical potential as well, and its value is around 550 s.

The Maximum RCS (Fig. 4.37) has the same behaviour of the other cases varying the chemical potential. More precisely, it is very similar to the case of the cloaking structure with rectangular strips of Section 10. Comparing the minimum frequencies and the cloaking bandwidths, it is possible to notice that f_0 varies a few for only some μ_c , while the bandwidths in this cases are a bit smaller except for $\mu_c = 1 \text{ eV}$, for which the band is practically 0 THz.

4.5.2 Electric field distribution in the normal plane to the cylinder

The electric field distributions at the previously-obtained cloaking frequencies are very similar to the previous case. For $\mu_c = 0 \text{ eV}$, at the cloaking frequency 6.5 THz there is only a bit more field than the case of Section 11 (Fig. 4.45). The same happens for the case with $\mu_c = 0 \text{ eV}$ at its cloaking frequency 7.2 THz (Fig. 4.46). The scattered field, instead, doesn't change from the previous cloaked cases.

4.5.3 Study of the RCS computed using a probe behind the cylinder

As the previous case, there is a low shift upwards of the RCSs and an enlargement of the cloaking bandwidths (Fig. 4.45 and 4.46). Now, for $\mu_c = 0 \text{ eV}$ $B = 1.512 \text{ THz}$ (with respect to 1.399 THz of the correspondent Maximum RCS), while for $\mu_c = 1 \text{ eV}$ $B = 0.476 \text{ THz}$ (with respect to 0.038 THz of the correspondent Maximum RCS). Besides, the cloaking frequencies are a bit shifted: for $\mu_c = 0 \text{ eV}$, $f_0 = 6.34 \text{ THz}$ (with respect to 6.5 of the Maximum RCS); instead, for $\mu_c = 1 \text{ eV}$ $f_0 = 7.17 \text{ THz}$ (with respect to 7.2 of the Maximum RCS).

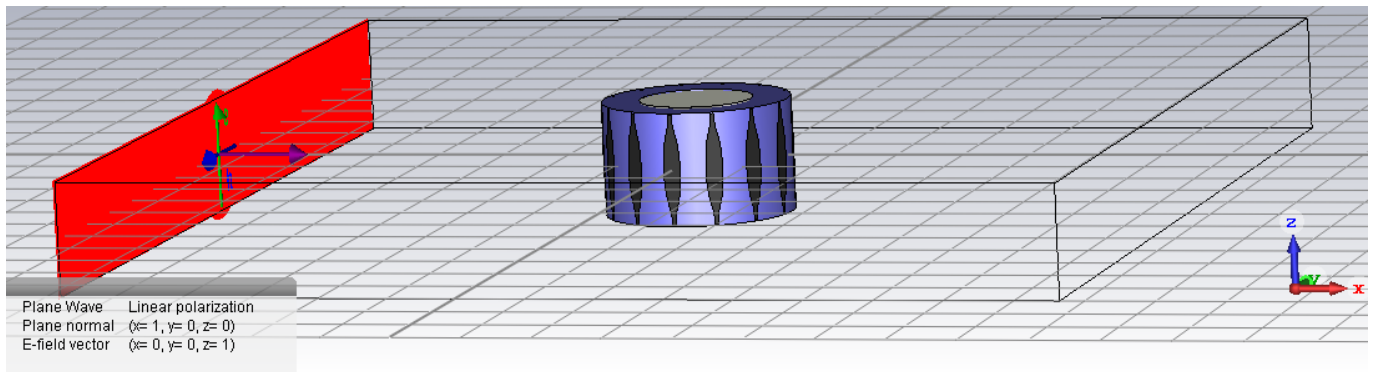


Figure 4.35: Cloaked cylinder with a dielectric of $h=5.56 \mu\text{m}$ and 14 modulated strips with mean amplitude $1.5 \mu\text{m}$.

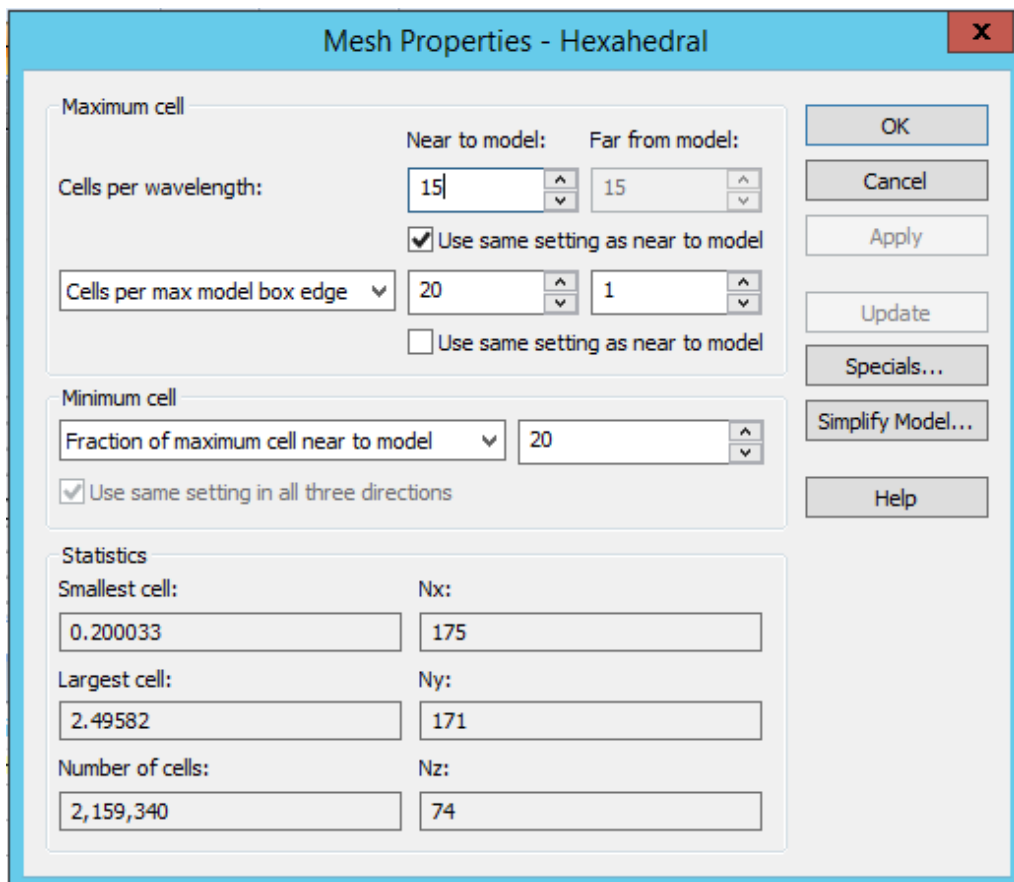


Figure 4.36: Mesh properties and cells statistics set for the simulation of the cloaking structure of Fig. 4.35 with any μ_c in CST.

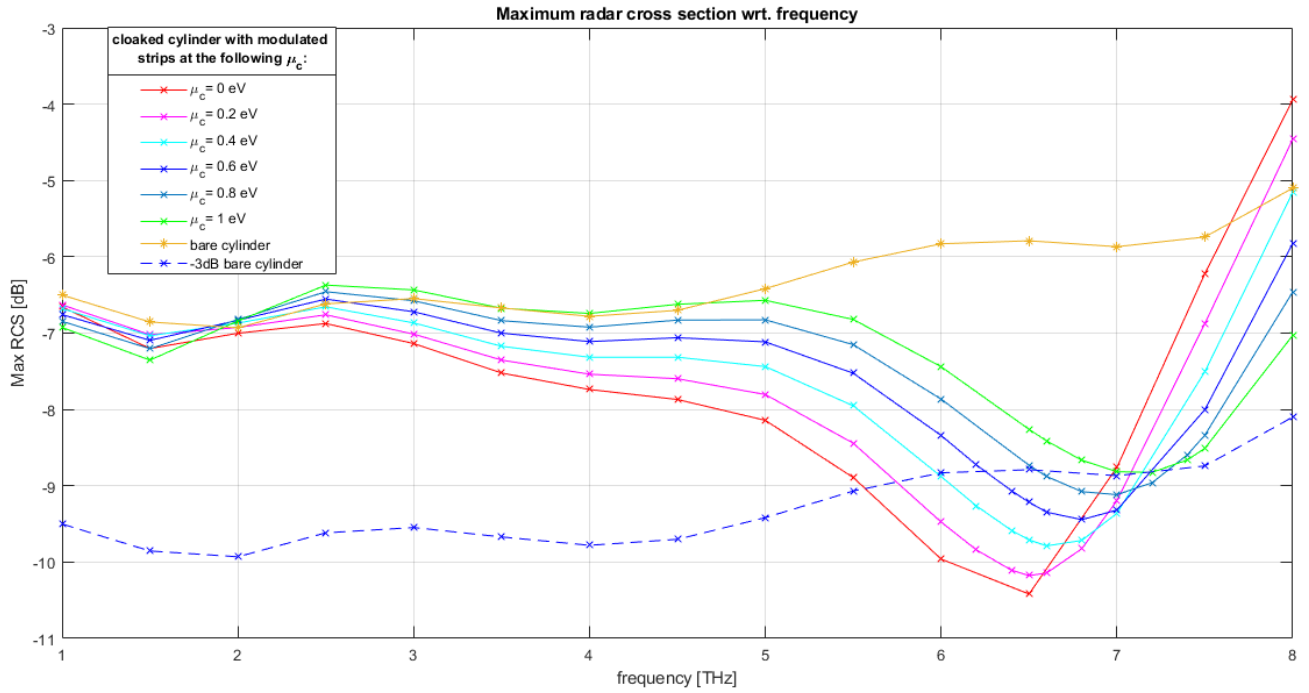


Figure 4.37: Maximum RCS for the cloaking structure with $h = 5.56 \mu\text{m}$ and modulated strips with mean amplitude $w = 1.5 \mu\text{m}$, varying the chemical potential μ_c .

Table 4.3: Minimum frequencies and the bandwidths of the Maximum RCS curves of Fig. 4.37 changing the chemical potential μ_c .

μ_c [eV]	f_0 [THz]	BW [THz]
0	6.5	1.399
0.2	6.5	1.325
0.4	6.6	1.157
0.6	6.8	0.936
0.8	7	0.743
1	7.2	0.038

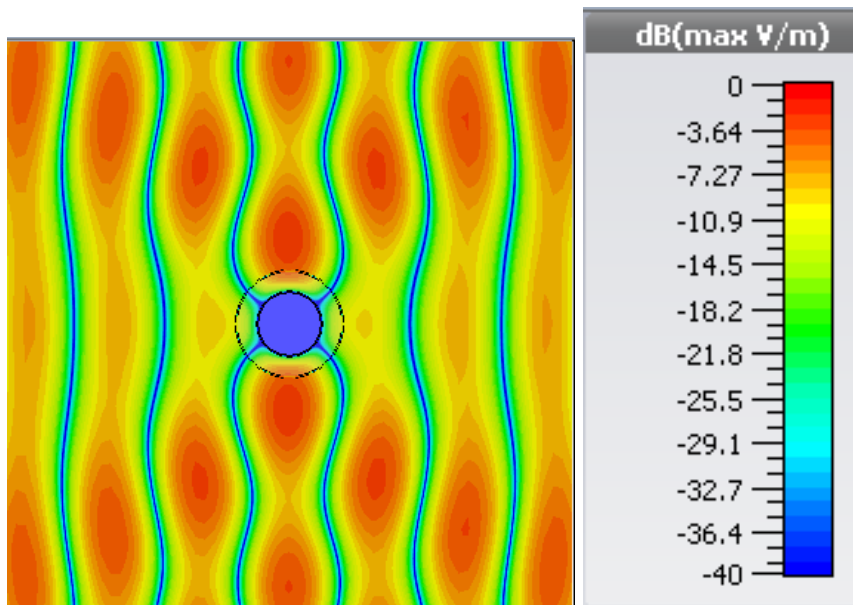


Figure 4.38: Electric field in the plane normal to the cloaked cylinder of Fig. 4.35 with $\mu_c = 0$ eV, at 6.5 THz.

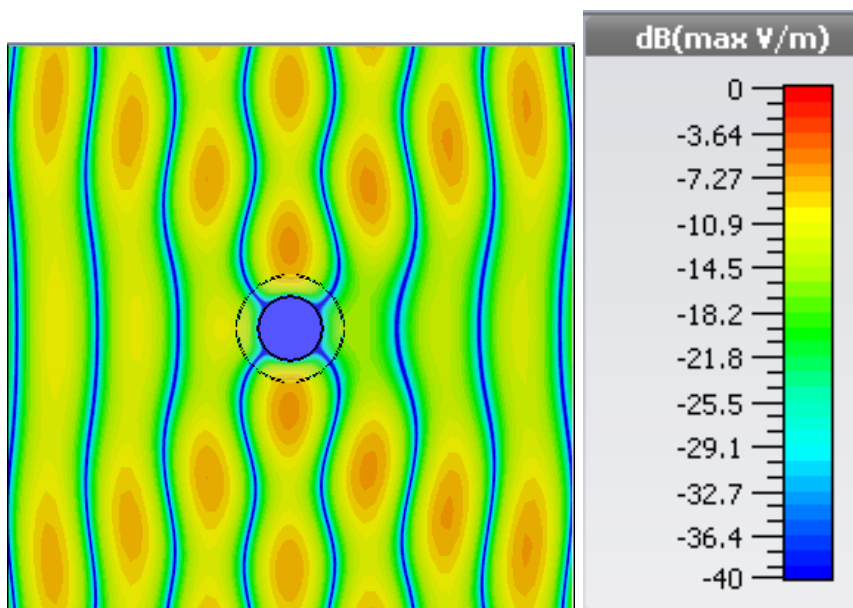


Figure 4.39: Electric field in the plane normal to the cloaked cylinder of Fig. 4.35 with $\mu_c = 1$ eV, at 7.2 THz

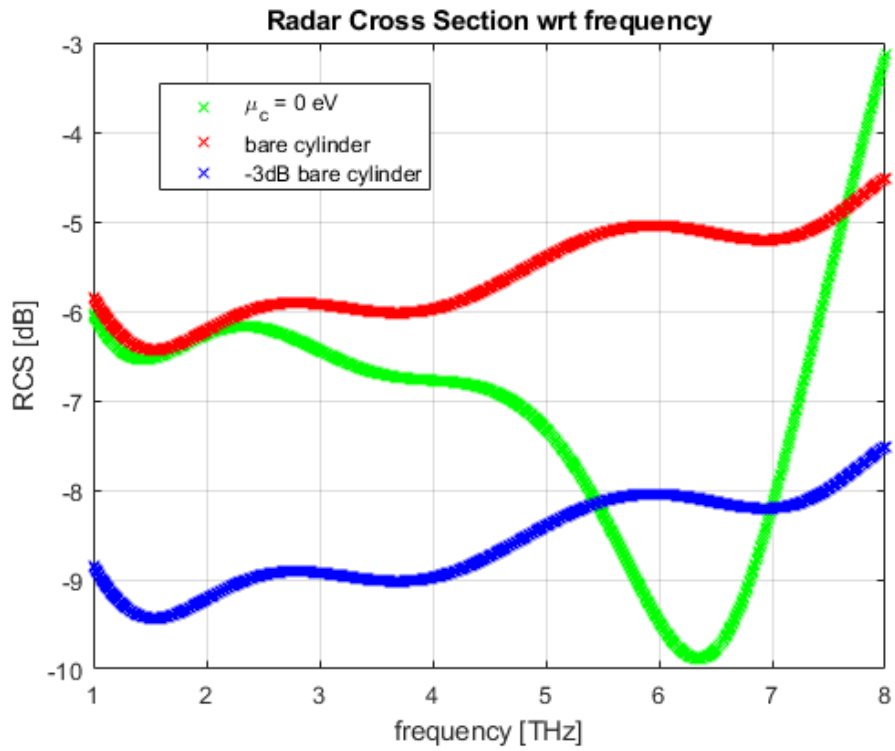


Figure 4.40: RCS in case of the cloaked structure of Fig. 4.35 where the strips have $\mu_c = 0$ eV, compared to the RCS of the bare cylinder.

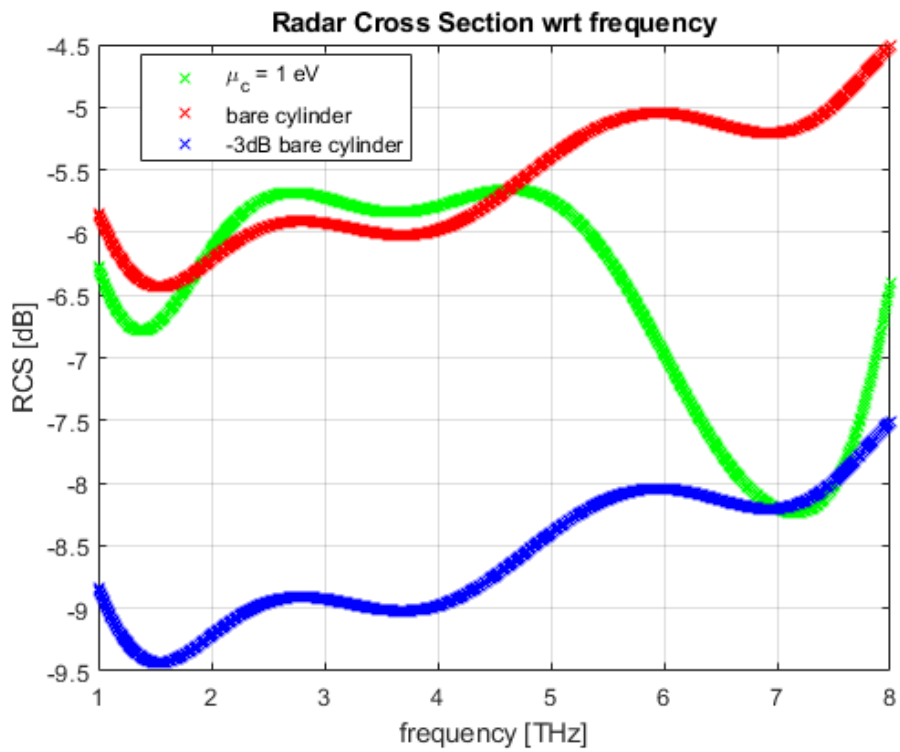


Figure 4.41: RCS in case of the cloaked structure of Fig. 4.35 where the strips have $\mu_c = 1$ eV, compared to the RCS of the bare cylinder.

4.6 Study of the behaviour of cloaked cylinder with modulated strips of mean amplitude $1.5 \mu\text{m}$ and dielectric thickness $10.5 \mu\text{m}$

Starting from the structure of the previous Section, only the dielectric thickness h is modified. Now, h becomes $10.5 \mu\text{m}$ (that corresponds to $\lambda_0/9.5238$) (Fig. 4.42). This solution allows to reach the cloaking at the wanted frequency, 3 THz.

4.6.1 Computation of the Maximum Radar Cross Section

The simulation of the considered structure takes quite different times according to the adopted chemical potential for the strips. The number of mesh cells is shown in Fig. 4.43. Fig. 4.44 shows that the Maximum RCSs are quite near to the wanted cloaking frequency 3 THz. The increase of h , in fact, shifts towards left the minimum of the Maximum RCS. But, also in this case, increasing the chemical potential μ_c increases the actual cloaking frequency. According to the table 4.4, the minimum of the Maximum RCS that happens at 3 THz is in case of $\mu_c = 0$ eV. Varying the chemical potential starting from 0 eV, f_0 increases until $\mu_c = 0.8$ eV. At 1 eV the minimum of the Maximum RCS doesn't reach the -3dB curve, so it is not possible to obtain the cloaking of the object in this particular case. The cloaking bandwidths, like for the previous case, reduce when the chemical potential is increased. But, differently from the previous Section, the bandwidths are smaller.

4.6.2 Electric field distribution in the normal plane to the cylinder

The electric field distribution at the cloaking frequency in case of $\mu_c = 0$ eV (Fig. 4.45) is similar to the previous case (only the wavelength is increased, since the cloaking frequency f_0 is reduced). Then, the distribution obtained for $\mu_c = 0.8$ eV is treated (Fig. 4.46), since at 1 eV it is not possible to reach the cloaking effect. Here the electric field is much less intense with respect to the case with $\mu_c = 0$ eV. However, in both cases the field behind the object is reconstructed completely equal to the one in front of it.

4.6.3 Study of the RCS computed using a probe behind the cylinder

In this last case, the RCSs computed considering the electric field only in a point, the one where the probes positioned, result shifted with respect to the correspondent RCSs: in case of $\mu_c = 0$ eV (Fig. 4.47), the RCS is downshifted of about 2 dB; instead, in case of $\mu_c = 1$ eV (Fig. 4.48), the RCS is up-shifted of about 1 dB. Besides, the minima frequencies are a bit right-shifted than the respective total RCSs: here the $f_0 = 3.2$ THz for $\mu_c = 0$ eV (instead of 3 THz in case of the total RCS). As regards the cloaking bandwidth B , it is a bit enlarged: 1.03 THz in case of $\mu_c = 0$ eV; while, for the correspondent total RCS $B = 0.949$ THz.

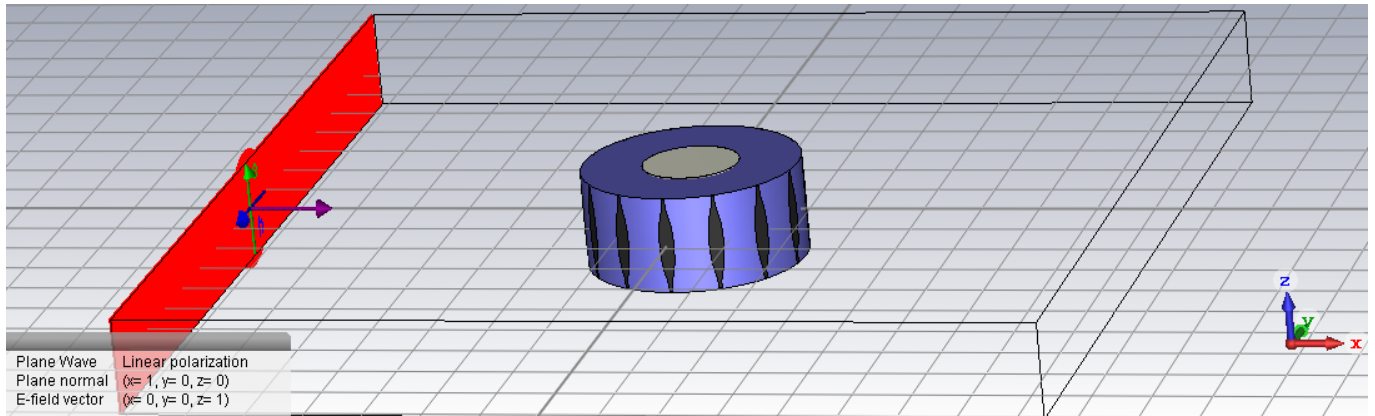


Figure 4.42: Cloaked cylinder with a dielectric of $h= 10.5 \mu\text{m}$ and 14 modulated strips with mean amplitude $1.5 \mu\text{m}$.

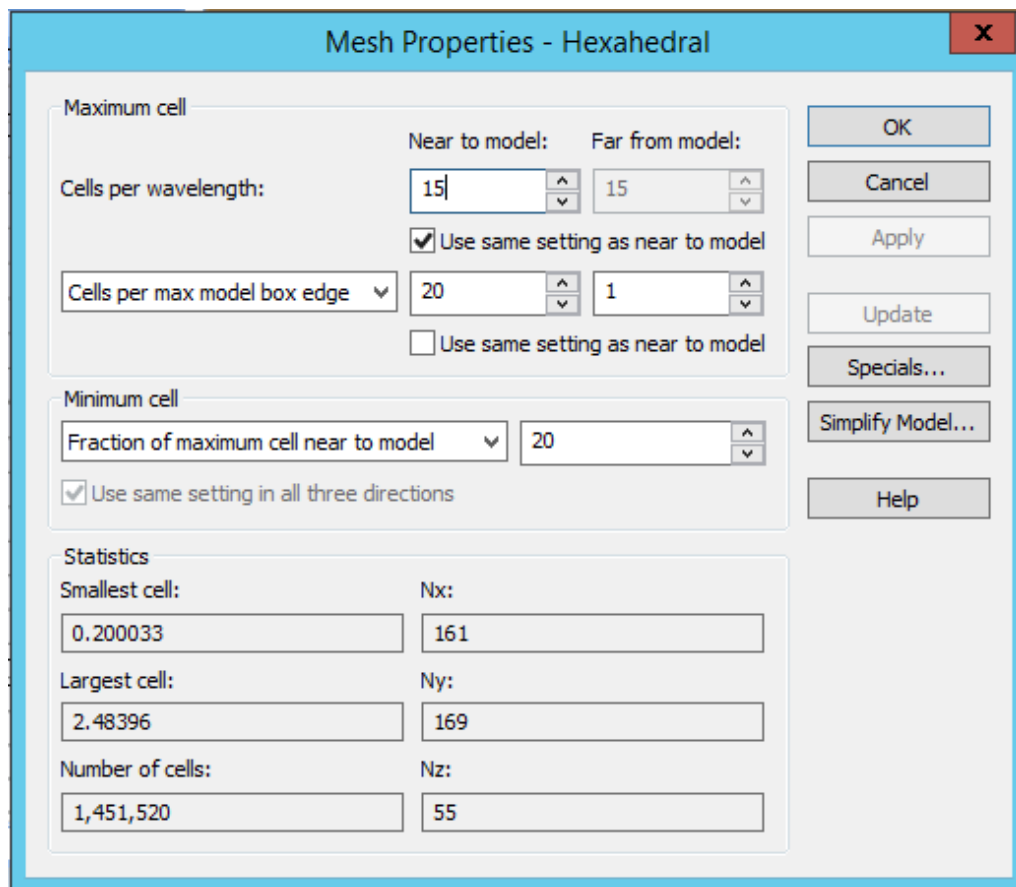


Figure 4.43: Mesh properties and cells statistics set for the simulation of the cloaking structure of Fig. 4.42 with any μ_c in CST.

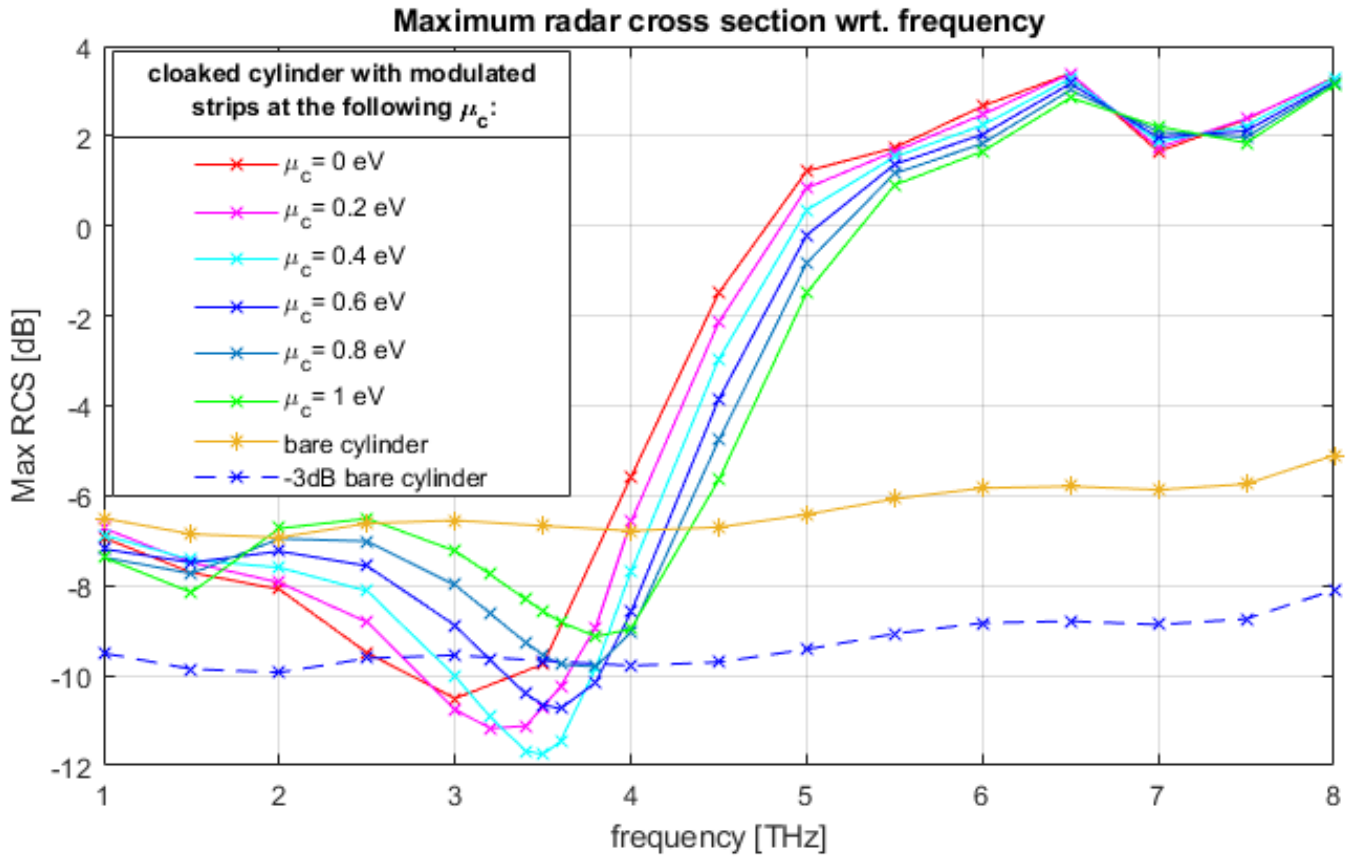


Figure 4.44: Maximum RCS for the cloaking structure with $h = 10.5 \mu\text{m}$ and modulated strips with mean amplitude $w = 1.5 \mu\text{m}$, varying the chemical potential μ_c .

Table 4.4: Table containing the minimum frequencies and the bandwidths of the Maximum RCS curves of Fig. 4.44 changing the chemical potential μ_c .

μ_c [eV]	f_0 [THz]	B [THz]
0	3	0.949
0.2	3.2	0.981
0.4	3.5	0.926
0.6	3.6	0.665
0.8	3.8	0.246
1	N.A.	0

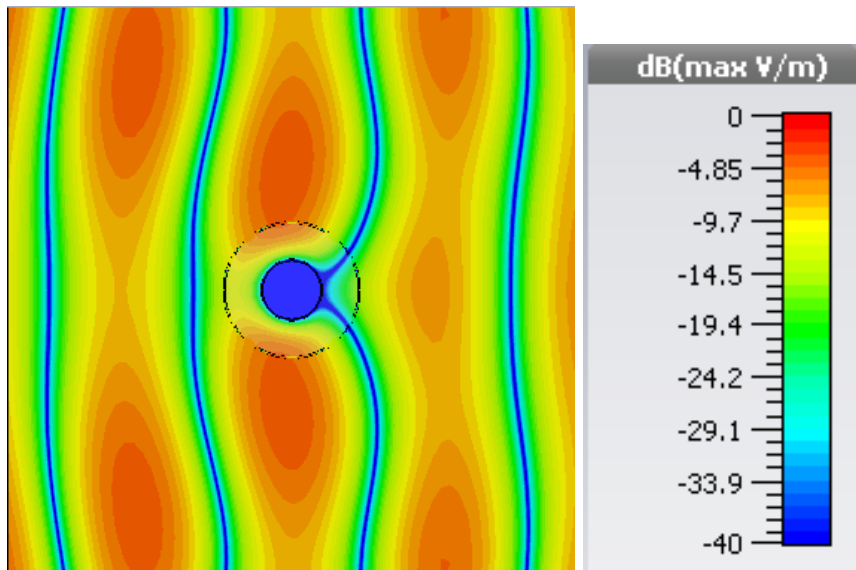


Figure 4.45: Electric field in the plane normal to the cloaked cylinder of Fig. 4.42 with $\mu_c = 0$ eV, at 3 THz.

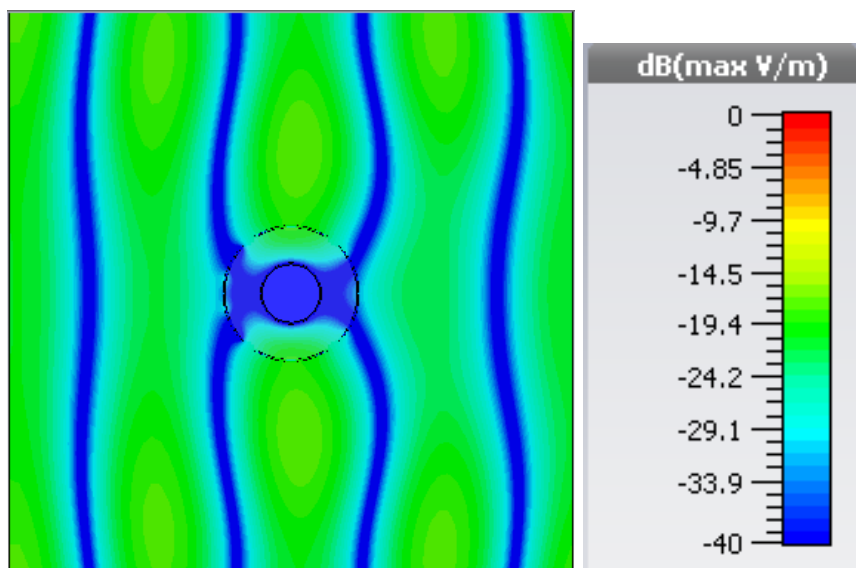


Figure 4.46: Electric field in the plane normal to the cloaked cylinder of Fig. 4.42 with $\mu_c = 0.8$ eV, at 3.8 THz

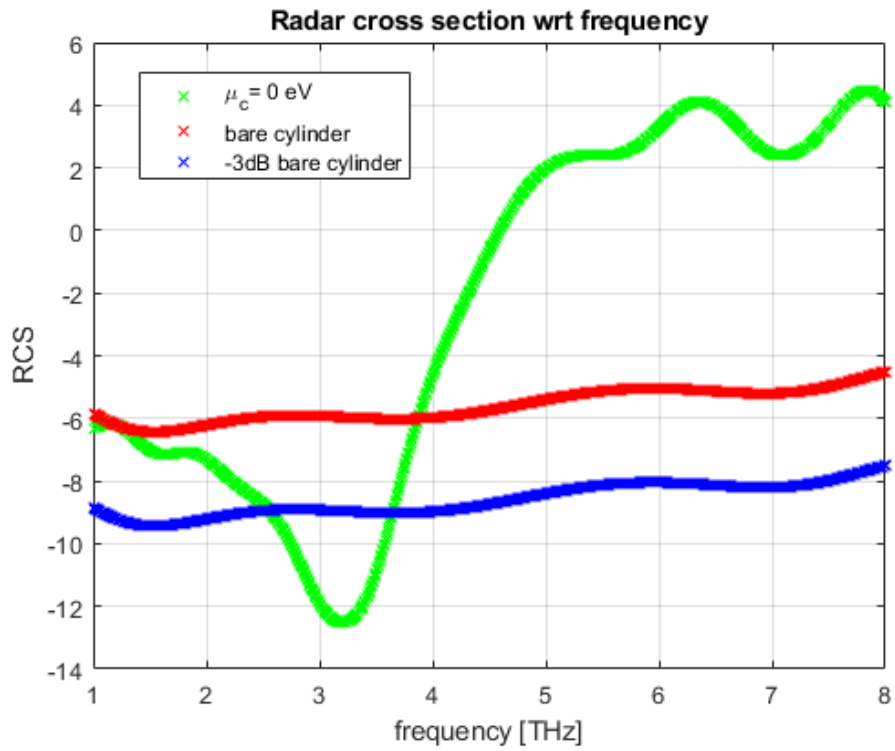


Figure 4.47: RCS in case of the cloaked structure of Fig. 4.42 where the strips have $\mu_c = 0$ eV, compared to the RCS of the bare cylinder.

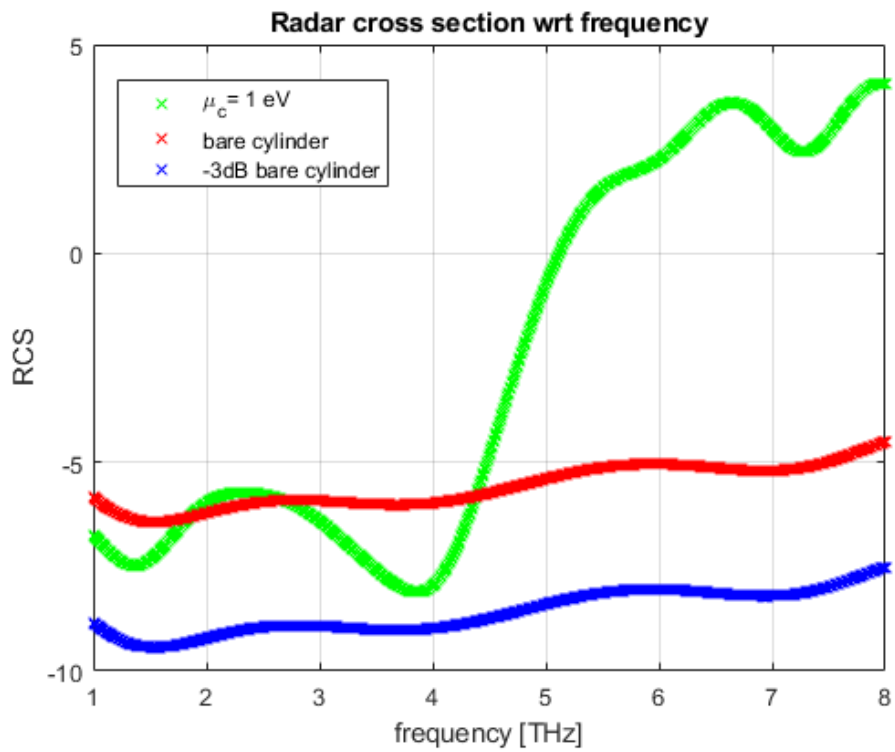


Figure 4.48: RCS in case of the cloaked structure of Fig. 4.42 where the strips have $\mu_c = 1$ eV, compared to the RCS of the bare cylinder.

Chapter 5

Variations on the structure and settings of Section 4.6

5.1 Study of the behaviour of the structure of Section 4.6 varying the number of modulated strips

The structure of the previous Section is taken into account and only the number of strips is varied. The simulation settings are the same as the previous Section. The total simulation time and the required number of mesh cells change according to the number of strips.

5.1.1 Case $\mu_c = 0$ eV

Now, the chemical potential of the strips is fixed to 0 eV, while the number n of the strips is changed. The Maximum RCS is computed for different numbers of strips. Fig. 5.1 shows that the behaviour of the RCS changes a few when the number of strips is changed. More precisely, looking at Fig. 5.2, the total variation (from the minimum n to the maximum one) of the Maximum RCS at f_0 is of 0.12 dB and its behaviour is decreasing, not in a monotonic way but in a sawtoothed way. Moreover, the minimum of the curves happens always at 3 THz.

5.1.2 Case $\mu_c = 1$ eV

In case of $\mu_c = 1$ eV, instead, the minimum of the Maximum RCS is right-shifted increasing the number of the strips n (Fig. 5.3). At the same time, the value of the minimum of the curve increases quite linearly with the n (Fig. 5.4): from -11.53 dB when $n = 5$, it arrives to about -7.442 dB when $n = 23$. However, from $n = 12$ on, the minimum of the curves stays over the -3dB curve (with respect to the Maximum RCS of the bare cylinder), so in these cases cloaking effect is not reachable in the considered frequency range.

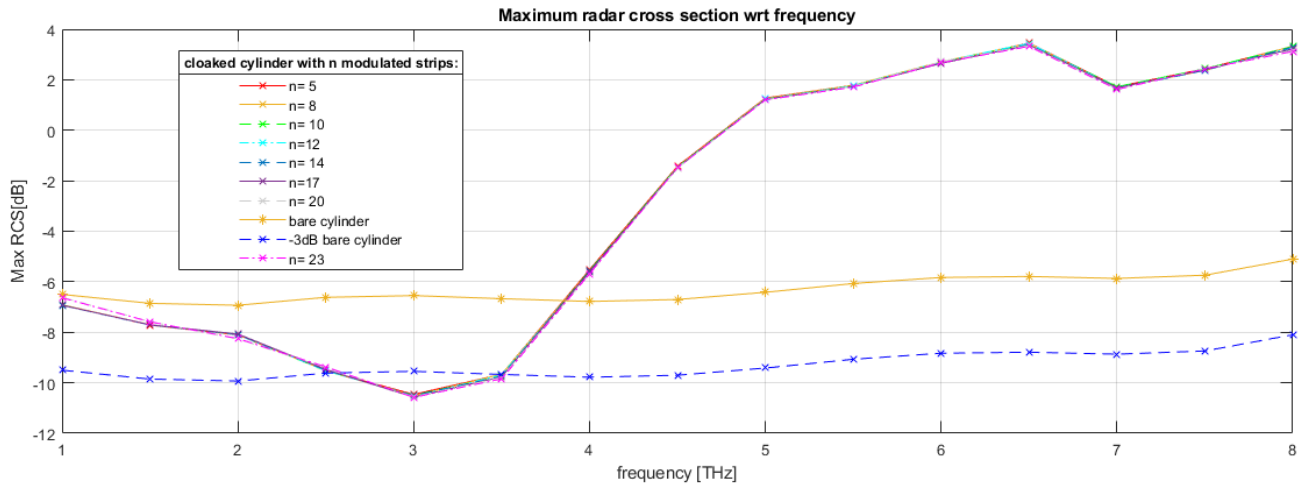


Figure 5.1: Maximum RCS for the cloaking structure with $h= 10.5 \mu\text{m}$ and modulated strips with mean amplitude $w= 1.5 \mu\text{m}$ and $\mu_c= 0 \text{ eV}$, varying the number of strips n .

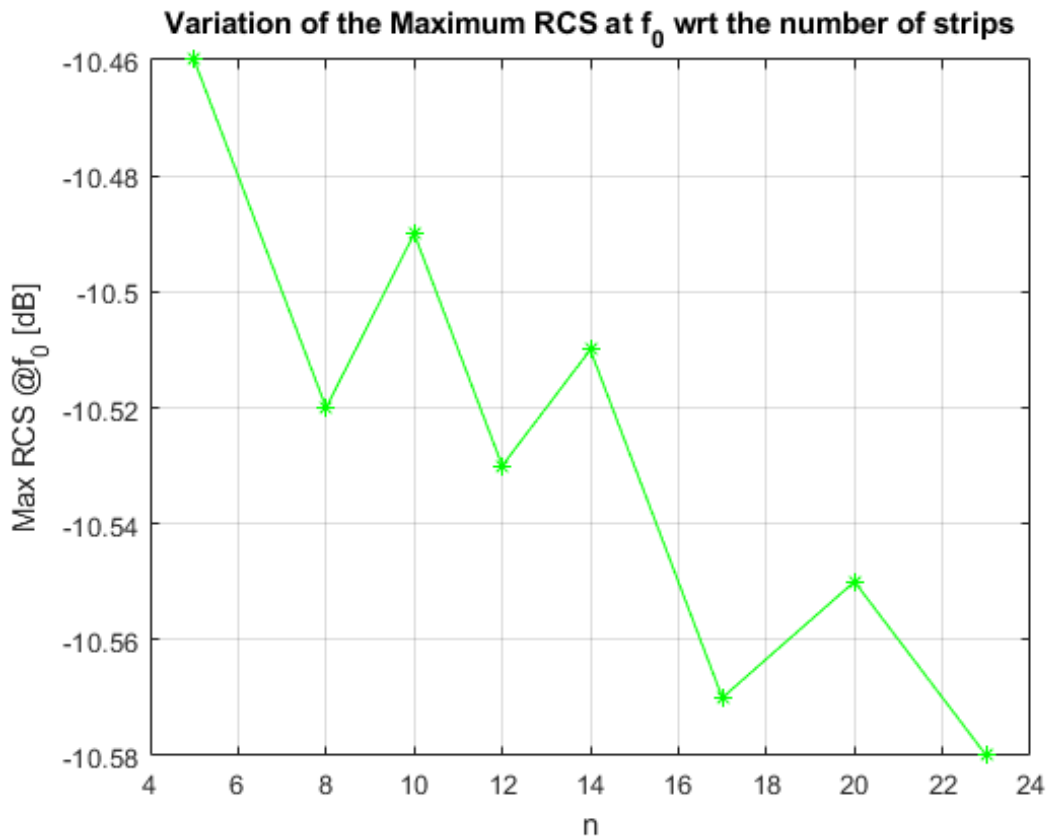


Figure 5.2: Variation of the Maximum RCS increasing the number of strips n , in case of $\mu_c= 0 \text{ eV}$.

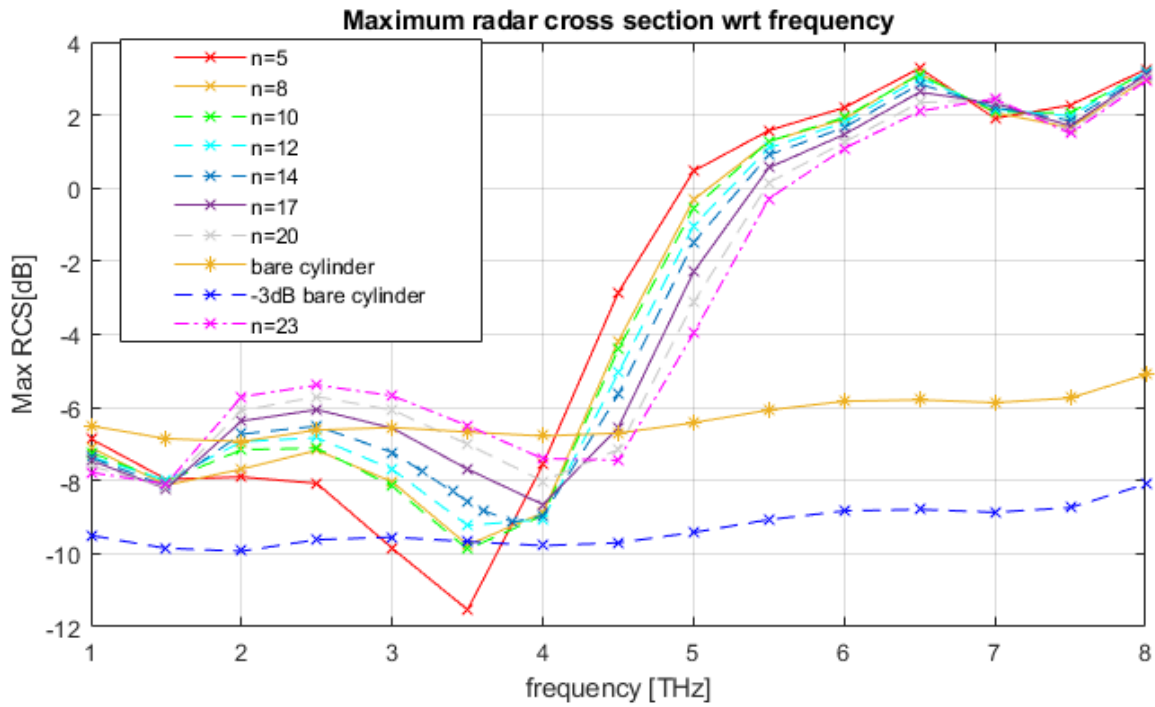


Figure 5.3: Maximum RCS for the cloaking structure with $h= 10.5 \mu\text{m}$ and modulated strips with mean amplitude $w= 1.5 \mu\text{m}$ and $\mu_c= 1 \text{ eV}$, varying the number of strips n .

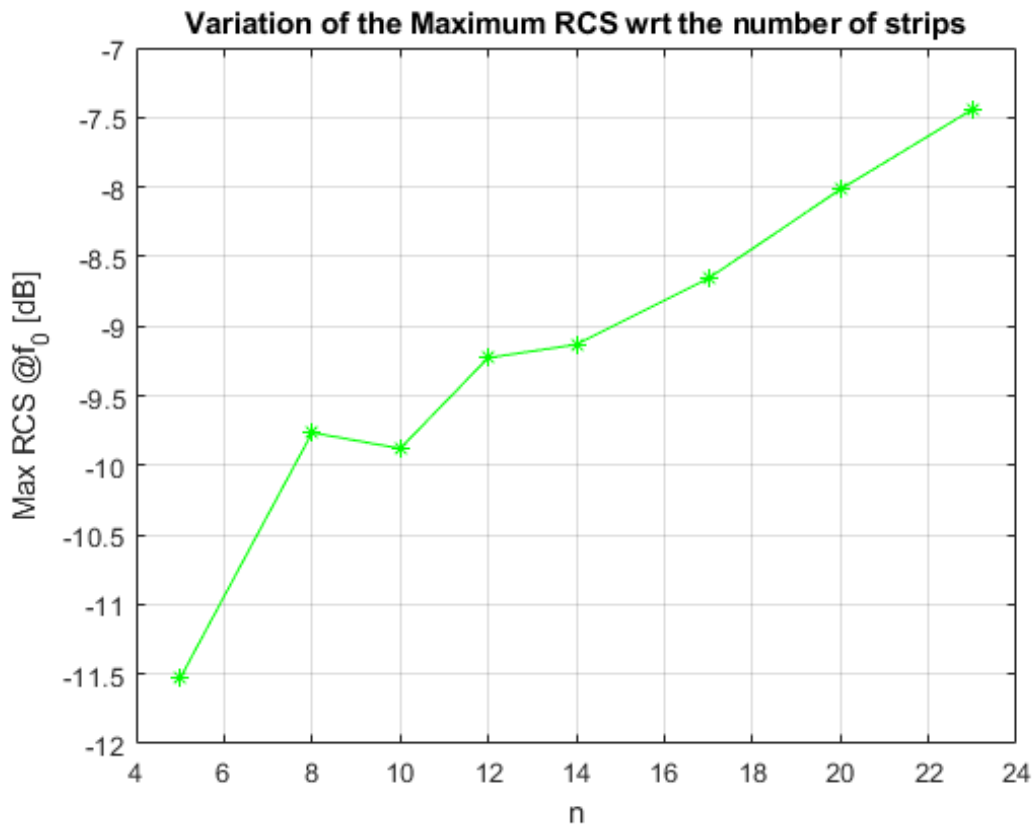


Figure 5.4: Variation of the Maximum RCS increasing the number of strips n , in case of $\mu_c= 1 \text{ eV}$.

5.2 Study of the behaviour of the structure of Section 4.6 with different polarizations

The structure adopted in the last Sections is now irradiated by a plane wave with a different direction of the electric field or with a different incidence angle. In this Section, the chemical potential μ_c of the *graphene* strips is fixed to 0 eV.

5.2.1 Polarization with electric field orthogonal to the cylinder

Here, the polarization of the plane wave is rotated of 90 degrees with respect to the Section 13: the magnetic field is parallel to the cylinder while the electric one is orthogonal to it (Fig. 5.5). Using this kind of polarization it is not possible to reach the cloaking of the considered object. In fact, Fig. 5.6 shows that the Maximum RCS of the cloaked object is always higher than the one of the bare cylinder (so also of its -3dB-shifted curve). Even if this increase of the Maximum RCS of the cloaked cylinder with respect to the case of the bare object doesn't allow to reach the invisibility of the object, it can be adopted in different applications, where you want to make the object more visible to a radar.

5.2.2 Polarization with oblique incidence

The direction of the plane wave is sloped of a certain angle, as Fig. 5.7 shows.

Figs. 5.8, 5.9 and 5.10 shows respectively the x,y and z components of the Maximum RCS in case of polarization with oblique direction of the plane wave. Since in each component the Maximum RCS of the cloaked cylinder is higher than the one of the bare cylinder, there is no cloaking effect in the considered range using the same coat adopted in case of polarization with the plane wave orthogonal to the cylinder.

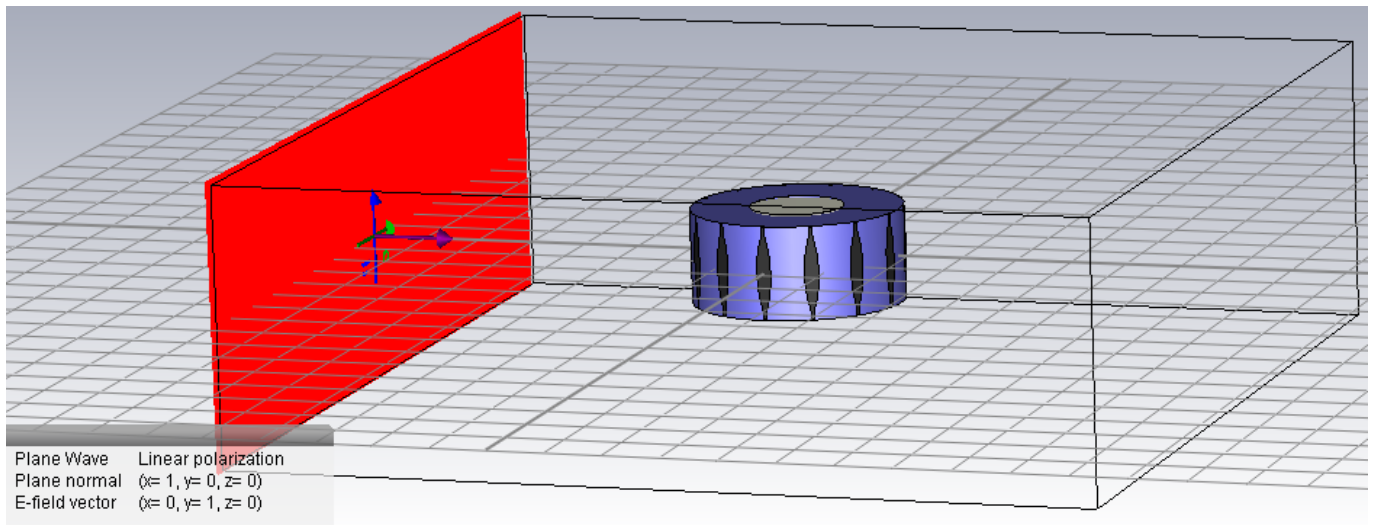


Figure 5.5: Cloaked cylinder with a dielectric of $h=10.5\ \mu\text{m}$ and 14 modulated strips with mean amplitude $1.5\ \mu\text{m}$. The plane wave has the magnetic field parallel to the object and the electric one orthogonal to it.

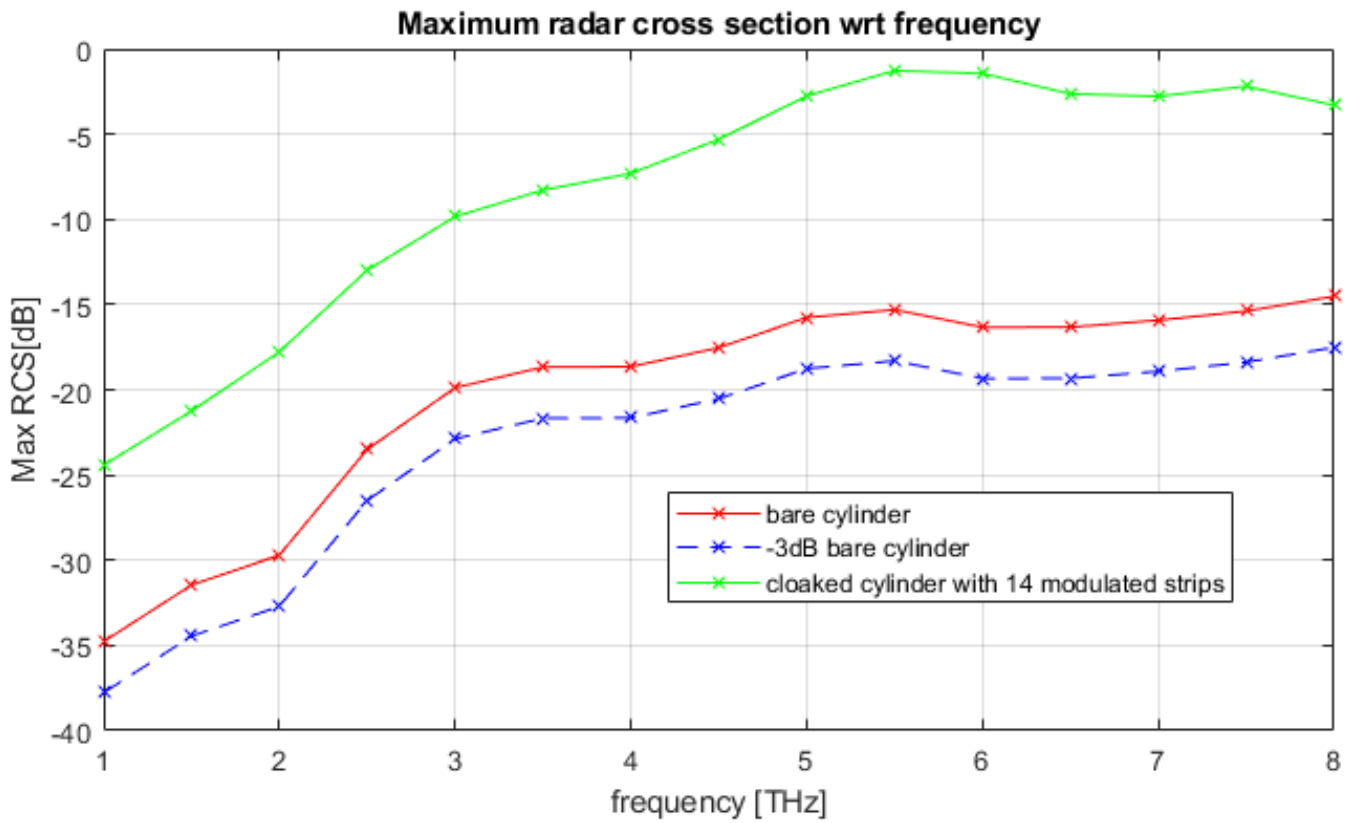


Figure 5.6: Maximum RCS for the structure and polarization of Fig. 5.5.

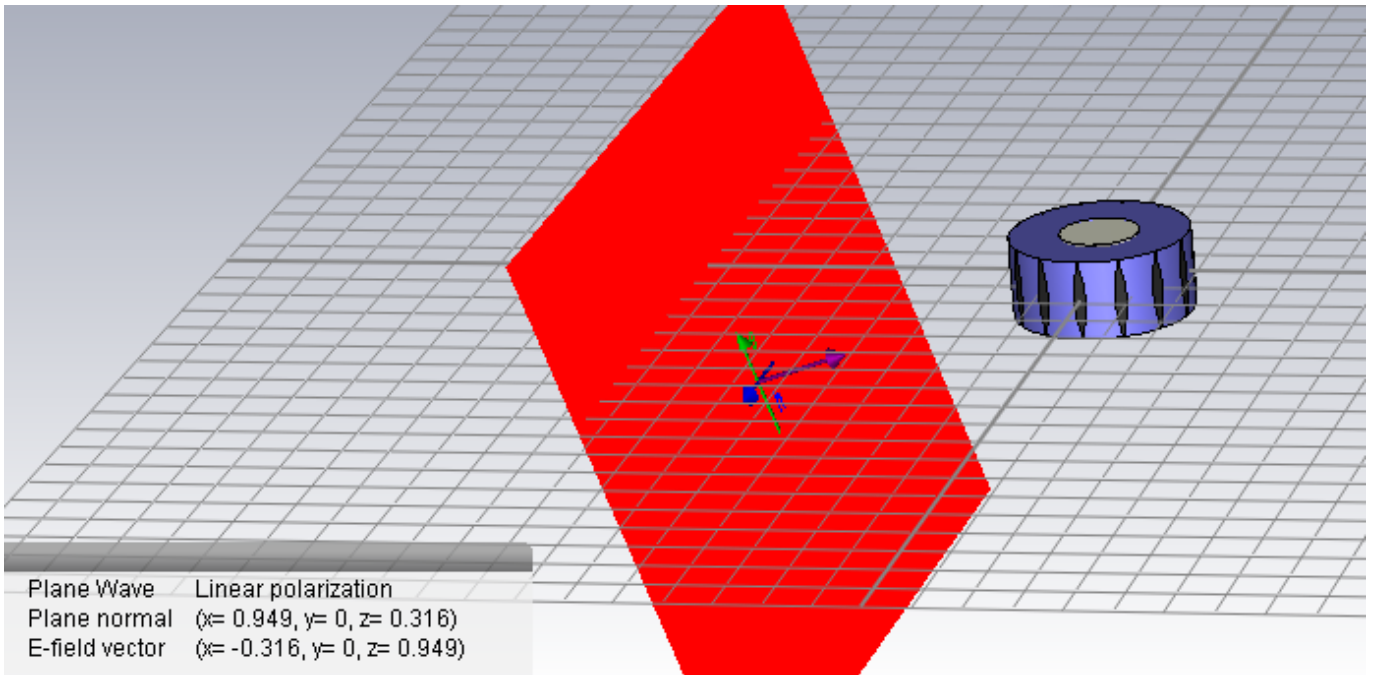


Figure 5.7: Cloaked cylinder with a dielectric of $h=10.5 \mu\text{m}$ and 14 modulated strips with mean amplitude $1.5 \mu\text{m}$. The plane wave has a sloped direction with respect to the object.

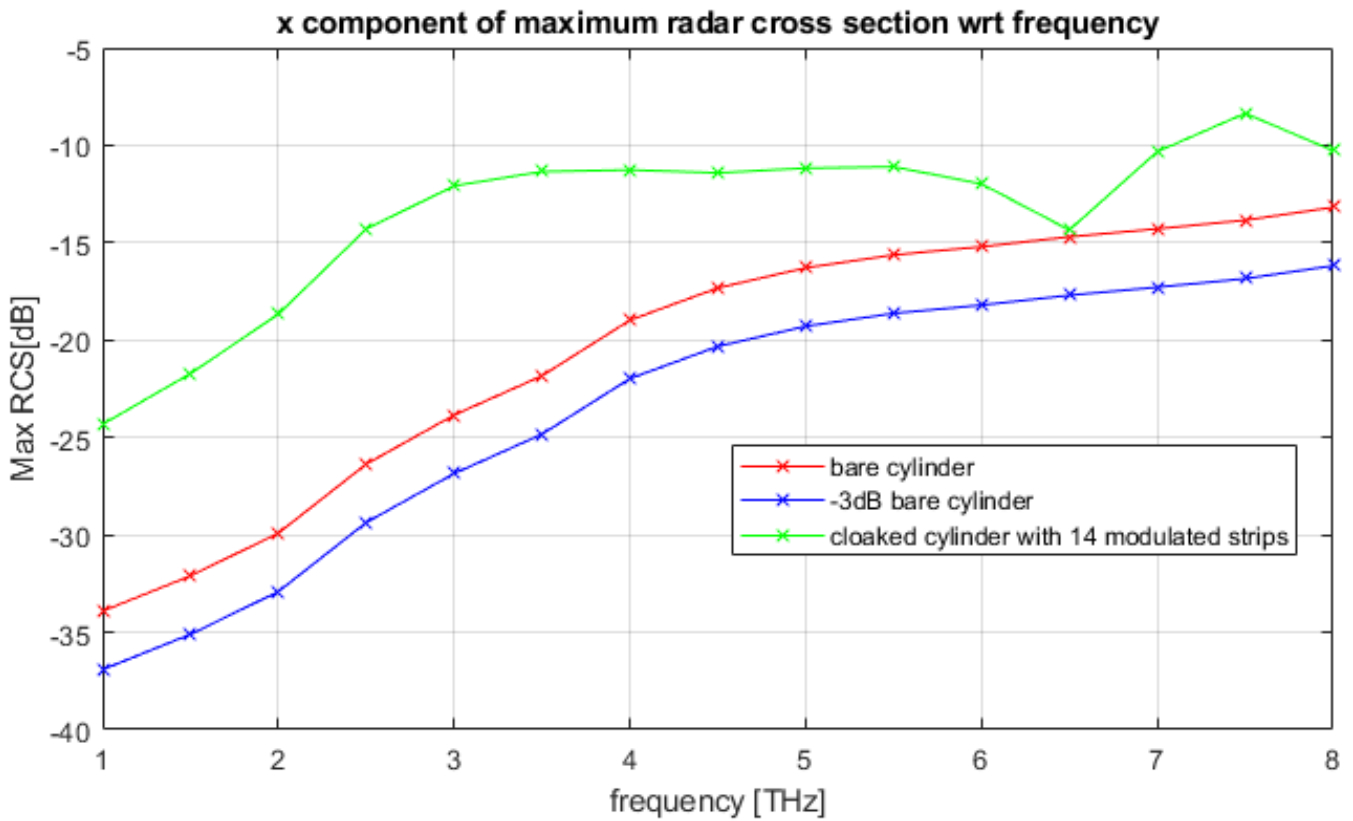


Figure 5.8: X-component of the Maximum RCS for the structure and polarization of Fig. 5.7.

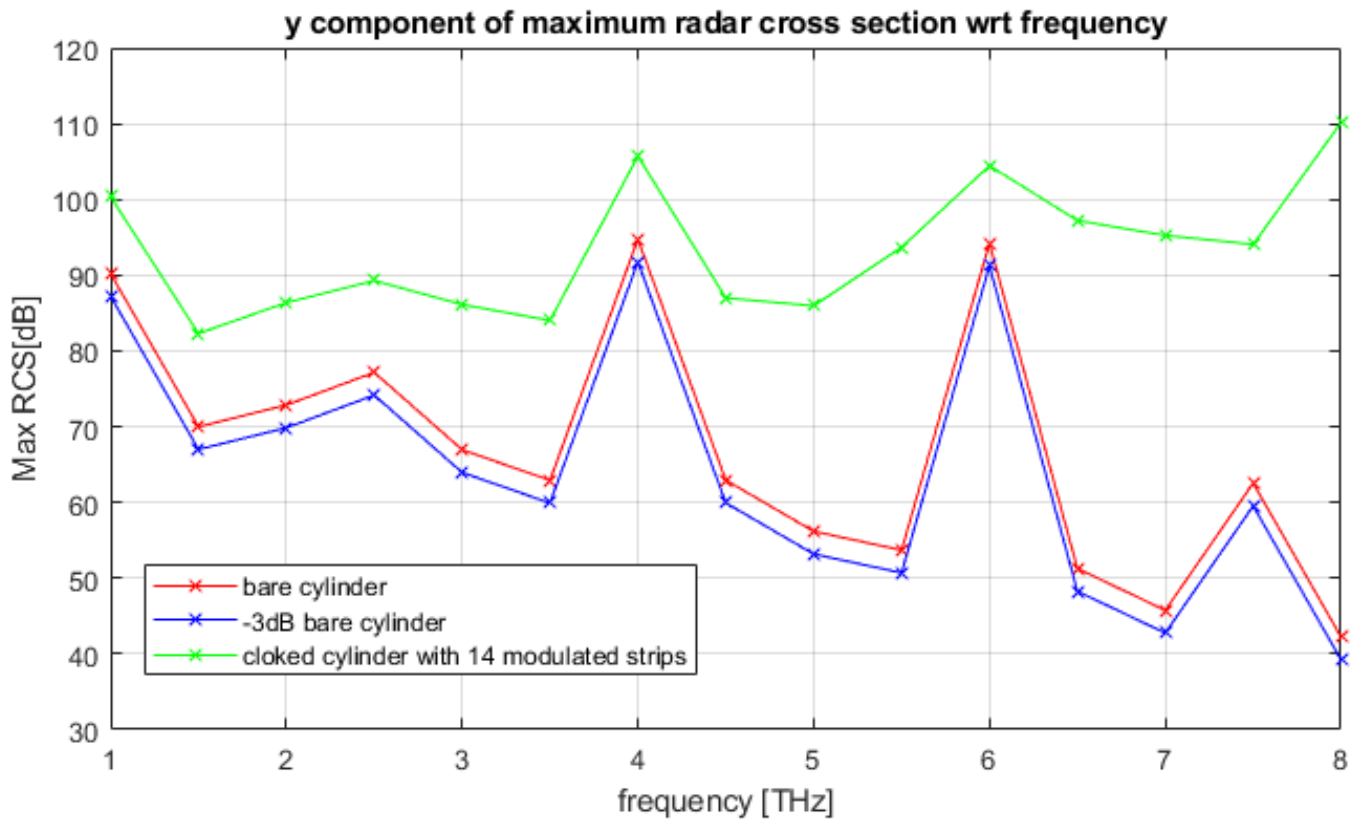


Figure 5.9: Y-component of the Maximum RCS for the structure and polarization of Fig. 5.7.

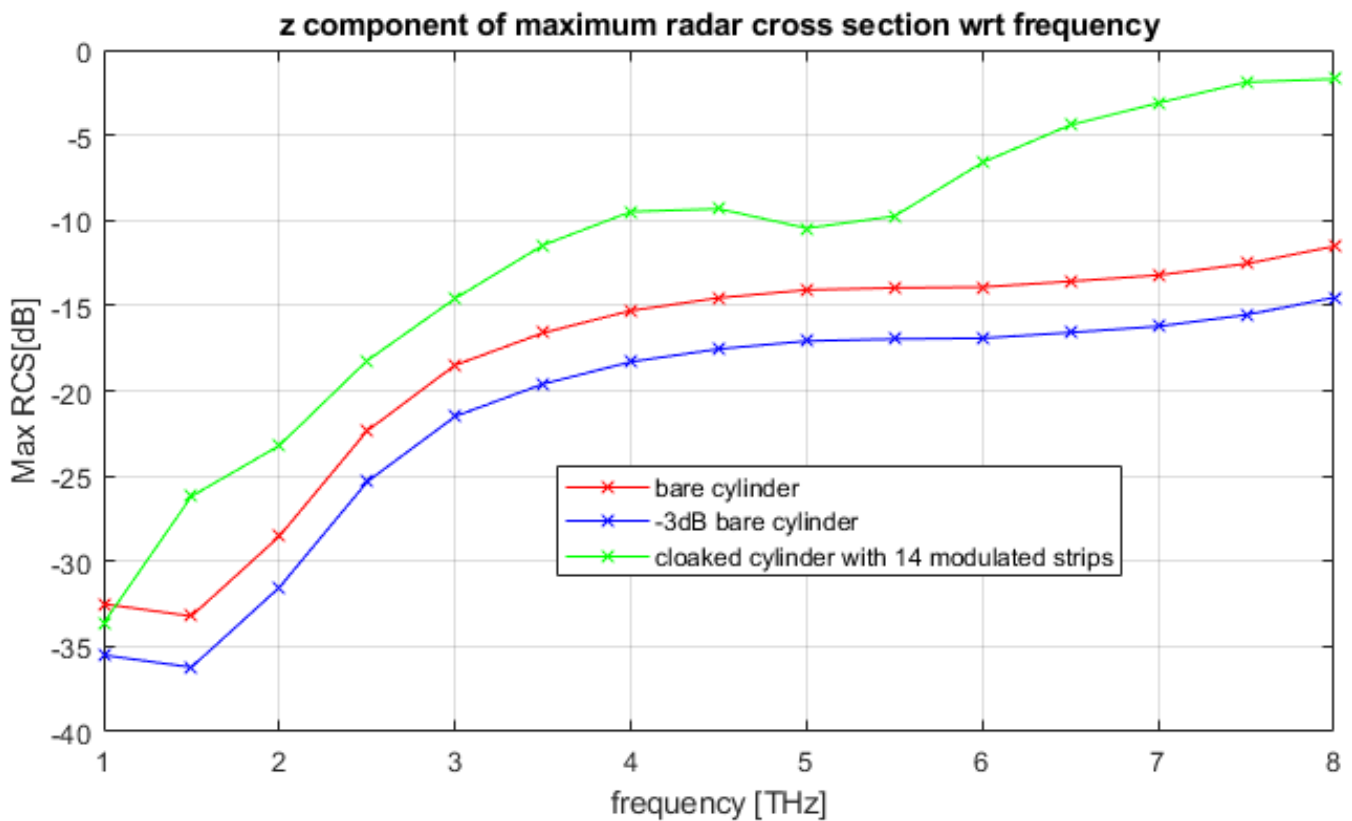


Figure 5.10: Z-component of the Maximum RCS for the structure and polarization of Fig. 5.7.

5.3 Study of the behaviour of the structure of Section 4.6 changing the material of the inner cylinder

The material of the considered object is changed from PEC. More specifically, two cases are analyzed:

1. cylinder made of silver;
2. cylinder made by a cylindrical layer of *graphene* at $\mu_c = 0$ eV and, inside, vacuum.

The simulation settings, including the number of mesh cells, are the same of Section 13.

5.3.1 Case of inner cylinder made of silver

The possibility of cloaking a cylinder made of silver using the coat adopted in the previous Sections is analyzed (Fig. 5.11).

The total simulation time is 11240 s.

From Fig. 5.12, it is possible to notice that, also in case of a silver cylinder, the cloaking is reachable at 3 THz.

The electric field at 3 THz is shown at Fig. 5.13. The field behind the cylinder is reconstructed equal to the one in front of it, since the object is cloaked.

5.3.2 Case of inner cylinder made by an external layer of graphene and, inside, vacuum

Now, the object to be cloaked is changed to a cylinder of vacuum covered by an external layer of *graphene* with $\mu_c = 0$ eV (Fig. 5.14).

The total simulation time is 11452 s.

In this case cloaking is not reached in the considered frequency range, as Fig. 5.15. In fact, there are more than 15 dB as spacing between the curve of the coated cylinder and the one of the bare cylinder.

The uncloaked behaviour is demonstrated also by the electric field graph (Fig. 5.16). The scattered field increases near the object and even more behind it. Besides, the field behind the cylinder has not the same distribution in terms of amplitude as in front of the cylinder.

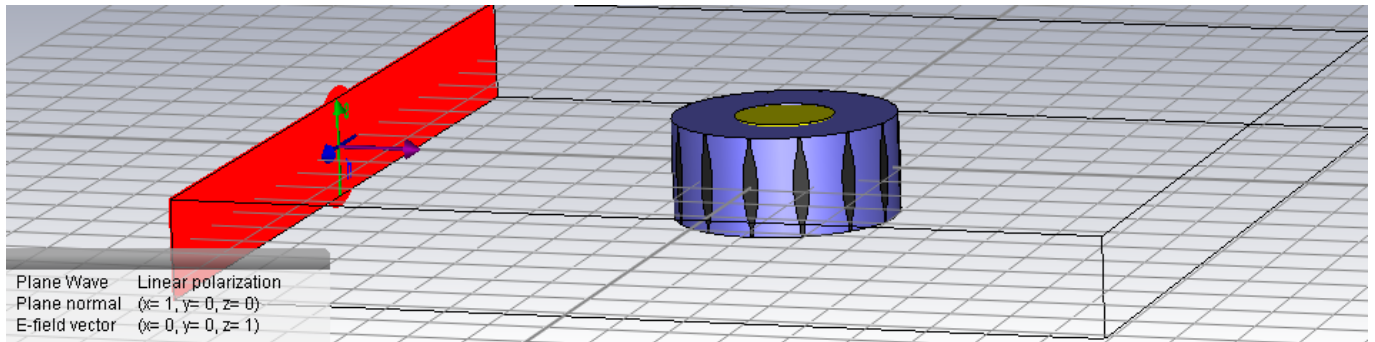


Figure 5.11: Cylinder made of silver, covered by the coat of Section 13.

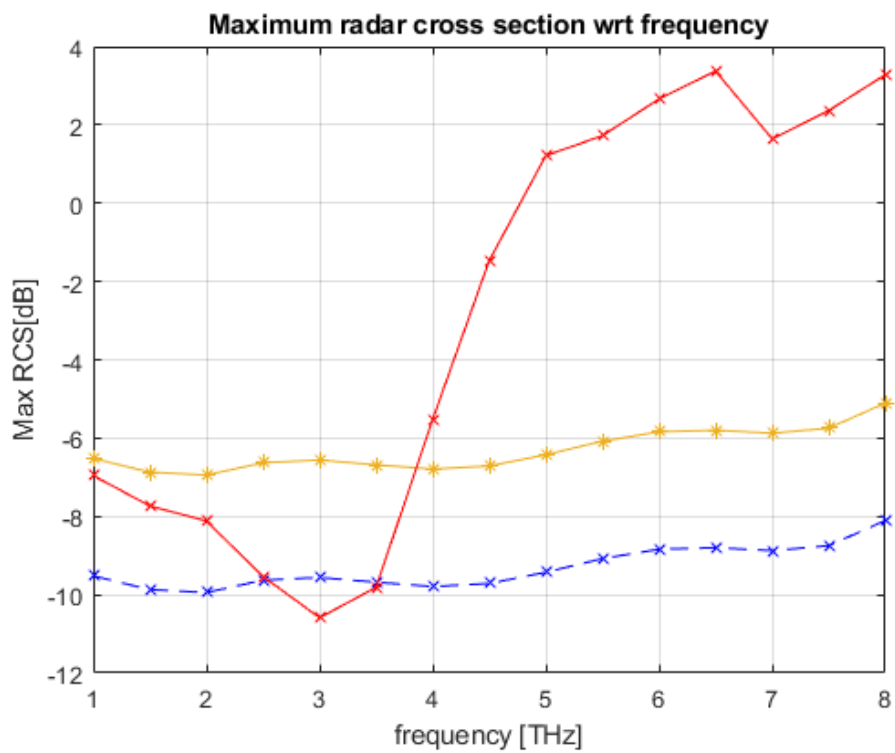


Figure 5.12: Maximum RCS for the cloaking structure with $h=10.5 \mu\text{m}$ and modulated strips with mean amplitude $w=1.5 \mu\text{m}$ and $\mu_c=0 \text{ eV}$.

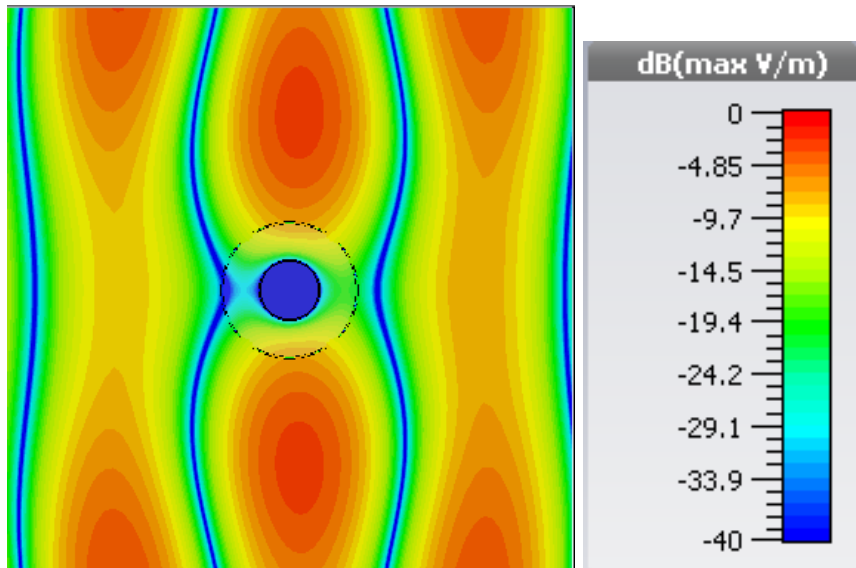


Figure 5.13: Electric field in the plane normal to the cloaked cylinder of Fig. 5.11 with $\mu_c = 0$ eV, at 3 THz

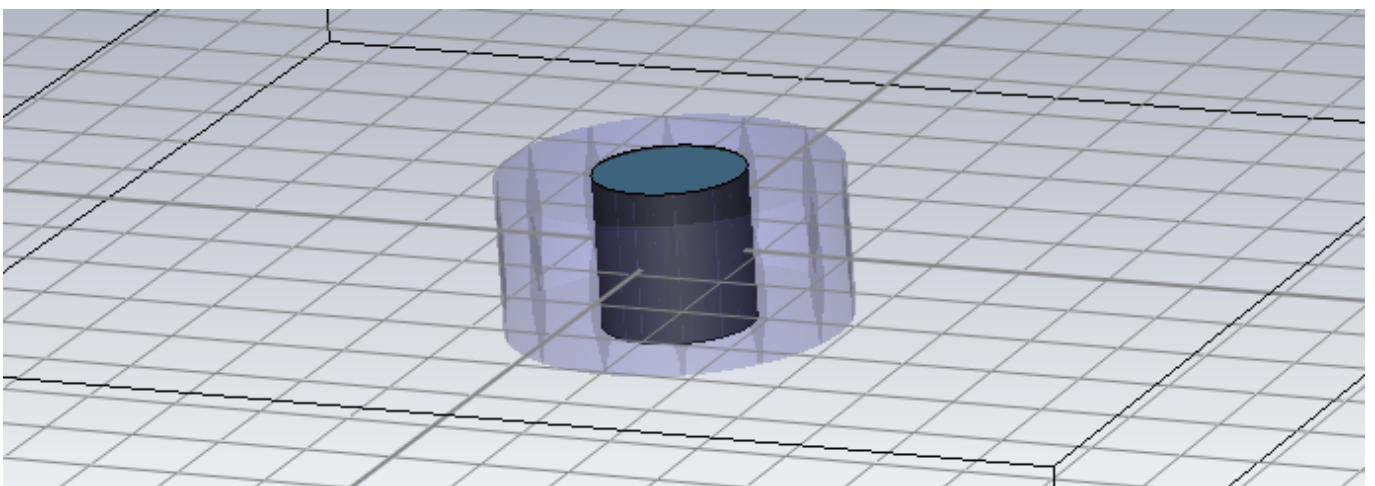


Figure 5.14: Cylinder made of vacuum and by an external layer of graphene with $\mu_c = 0$ eV, covered by the coat of Section 13.

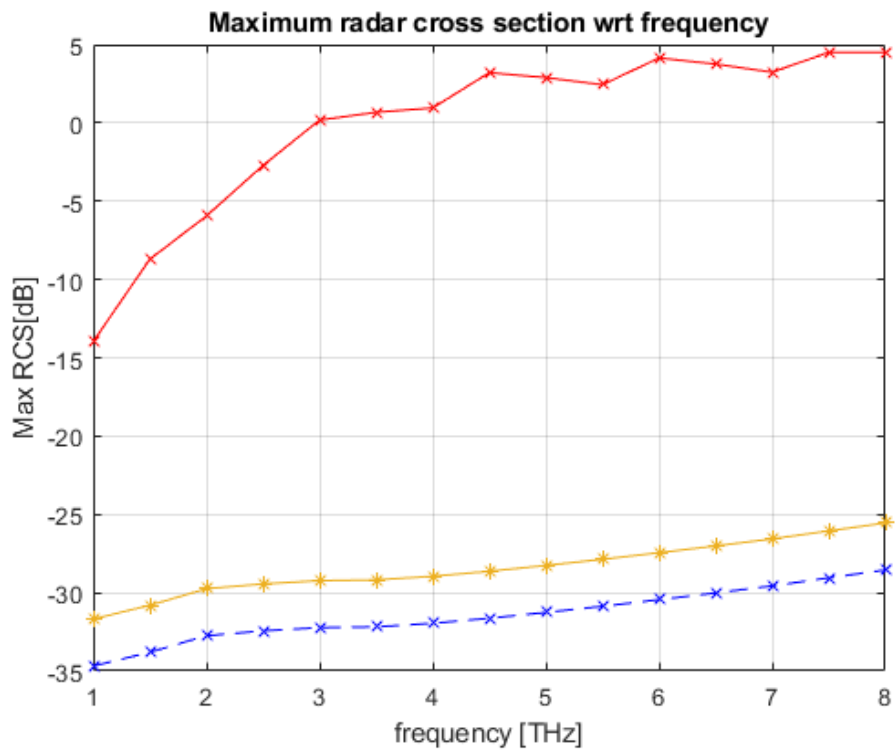


Figure 5.15: Maximum RCS for the cloaking structure with $h = 10.5 \mu\text{m}$ and modulated strips with mean amplitude $w = 1.5 \mu\text{m}$ and $\mu_c = 0 \text{ eV}$.

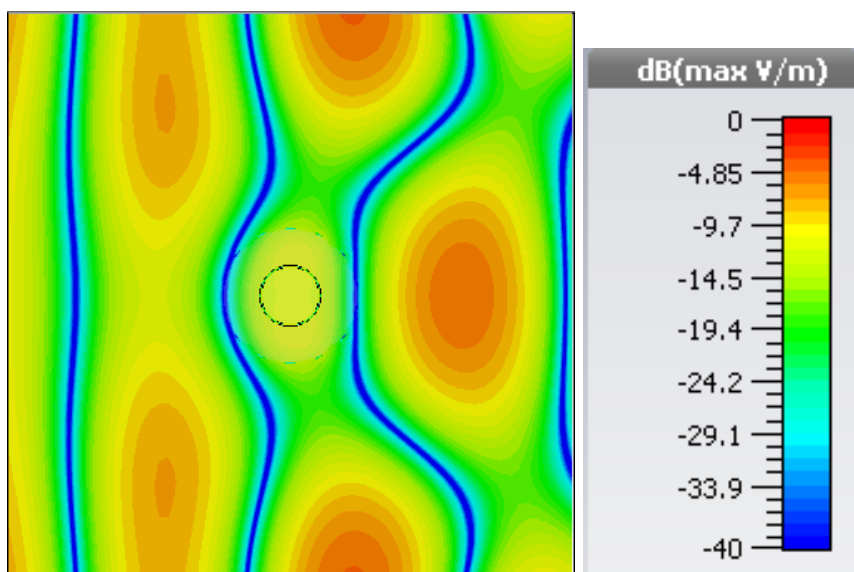


Figure 5.16: Electric field in the plane normal to the cloaked cylinder of Fig. 5.14 with $\mu_c = 0 \text{ eV}$, at 3 THz

5.4 Study of the behaviour of the structure of Section 4.6 varying gradually the chemical potential in different strips

In order to find a better cloaking configuration, the chemical potential μ_c is varied progressively in nearby strips, starting from the structure of Section 4.6. The progressive variation of the chemical potential of different strips is chosen in order to try to reduce the effects of the deviation due to the presence of the object on the impinging wave.

Two cases are presented:

- μ_c starts from 0 eV in the strip straightly illuminated by the plane wave, then it increases until 1 eV is reached in the following strips, after that it decreases until 0 eV, and so on;
- μ_c starts from 1 eV in the strip straightly illuminated by the plane wave, then it reduces in the successive strips; when 0 eV is reached, μ_c starts increasing and so on.

5.4.1 Case of starting $\mu_c = 0$ eV

In this case, the chemical potential starts from 0 eV in the first strip, it increases until 1 eV in the following strips (moving in clockwise direction), then it reduces and so on. More specifically, the values of the chemical potential, following the previously cited order: [0 0.3 0.7 1 0.7 0.3 0 0 0.3 0.7 1 0.7 0.3 0].

Computation of the Maximum Radar Cross Section The Maximum RCS, in this case, is increased from the case with $\mu_c = 0$ eV, mostly in the frequency range around the wanted cloaking frequency (Fig. 5.17). Looking at the table 5.1, it is possible to notice that, while the cloaking frequency remains the same of the case with fixed $\mu_c = 0$ eV, the cloaking bandwidth is reduced a lot, since it became almost zero.

Electric field distribution in the normal plane to the cylinder The electric field distribution at 3 THz, now, is equal before and after the cylinder, since at this frequency there is cloaking (Fig. 5.18). But, differently from the electric field of the case with fixed $\mu_c = 0$ eV, here the electric field is much less intense (-20 dB of intensity with respect to the other case).

5.4.2 Case of starting $\mu_c = 1$ eV

The complementary case of the previous Section is treated here. The starting chemical potential is, now, 1 eV, so at the beginning it is reduced in the next strips (moving clockwise as in the previous Section). Then, when 0 eV is reached, it is increased. The adopted values of the chemical potential, in the order as before, are: [1 0.7 0.3 0 0.3 0.7 1 1 0.7 0.3 0 0.3 0.7 1].

Computation of the Maximum Radar Cross Section Differently from the complementary case, now, the Maximum RCS is reduced a lot with respect to the case with fixed $\mu_c = 1$ eV (Fig. 5.19). While in case of fixed $\mu_c = 1$ eV there is never cloaking in the considered frequency range, in this case cloaking is reached around 3.5 THz (table 5.2).

Electric field distribution in the normal plane to the cylinder The electric field distribution at 3.5 THz shows how much is reported in the previous paragraph (Fig. 5.20): the field behind the object is, indeed, almost the same as in front of it. The field is more intense than the one of the previous paragraph.

This distribution cannot be compared to the one obtained for fixed $\mu_c = 1$ eV, since in that case there is no cloaking. But it is possible to notice that it is almost identical to the one obtained for the same structure but with fixed $\mu_c = 0.8$ eV at 3.8 THz.

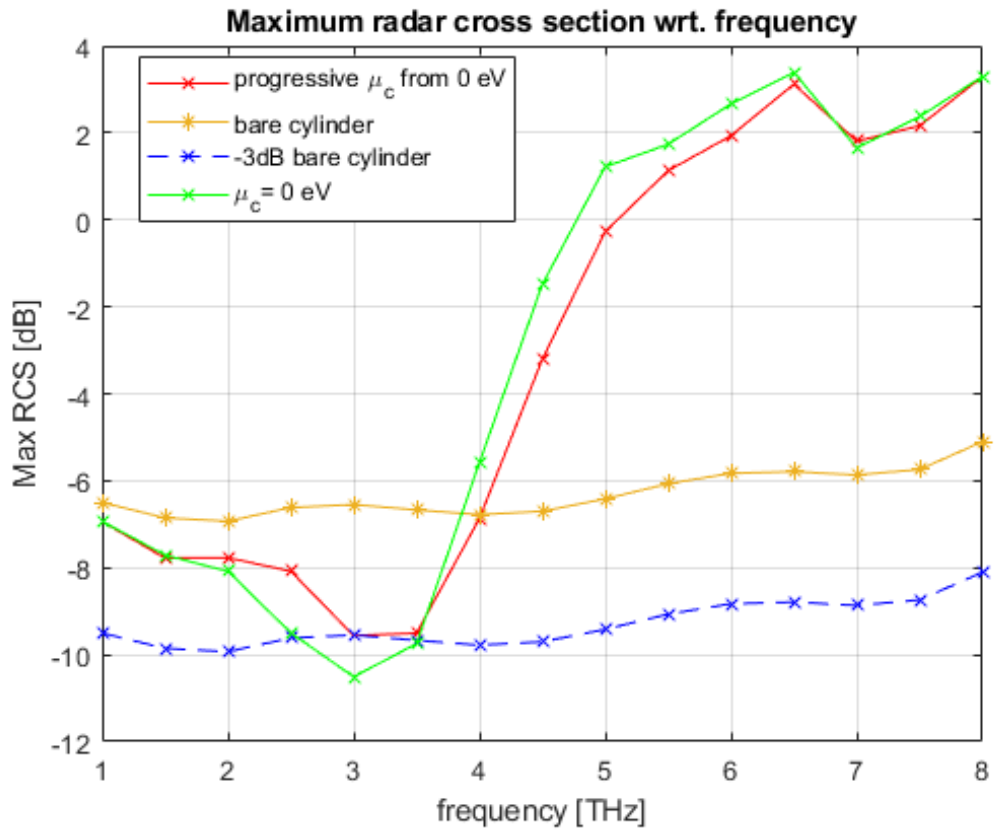


Figure 5.17: Maximum RCS for the structure of Section 4.6 where μ_c is varied progressively from 0 eV.

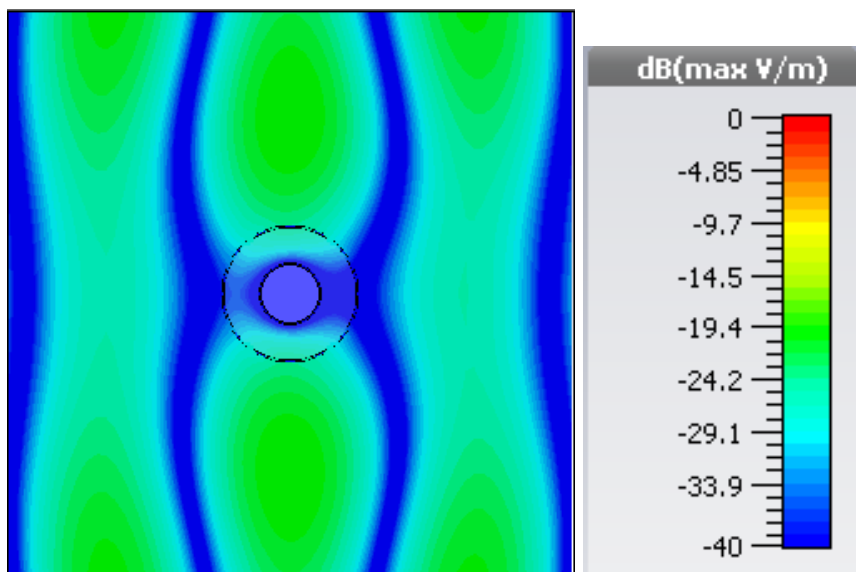


Figure 5.18: Electric field in the plane normal to the cloaked cylinder of Section 4.6 with progressively varying μ_c from 0 eV, at 3 THz.

Table 5.1: Minimum frequencies and the bandwidths of the Maximum RCS curves of Fig. 5.17 according to the chemical potential μ_c .

μ_c [eV]	f_0 [THz]	BW [THz]
0	3	0.949
progressive from 0	3	0.039

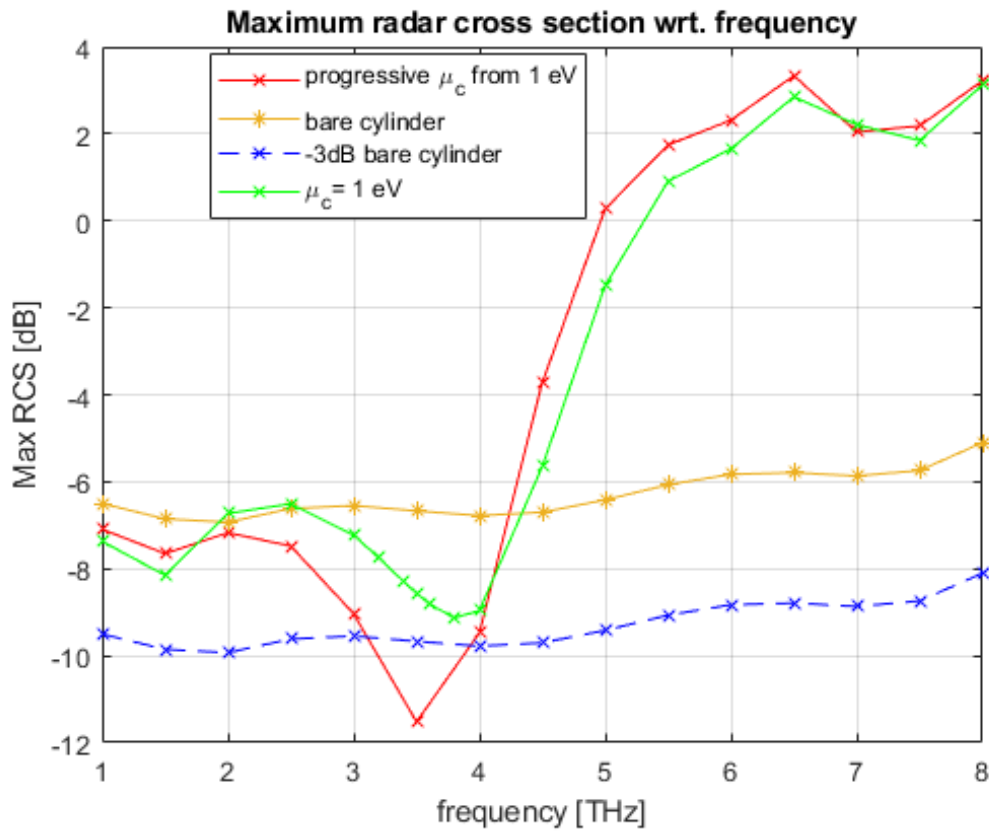

 Figure 5.19: Maximum RCS for the structure of Section 4.6 where μ_c is varied progressively from 1 eV.

 Table 5.2: Minimum frequencies and the bandwidths of the Maximum RCS curves of Fig. 5.19 according to the chemical potential μ_c .

μ_c [eV]	f_0 [THz]	BW [THz]
1	N.A.	0
progressive from 1	3.5	0.824

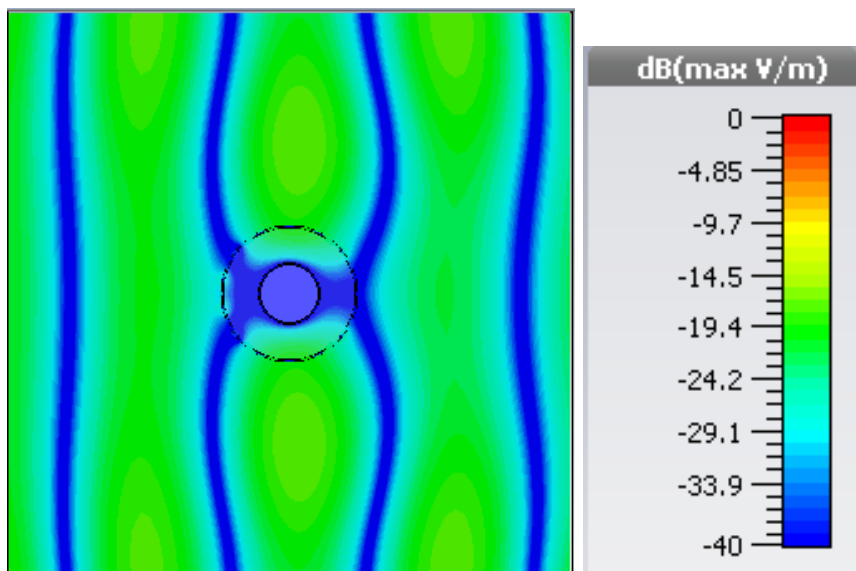


Figure 5.20: Electric field in the plane normal to the cloaked cylinder of Section 4.6 with progressing varying μ_c from 1 eV, at 3.5 THz.

Conclusions

In this thesis, the cloaking of a metallic cylinder is investigated in the THz band.

Firstly, cloaking and some of the most used techniques are presented, focusing on *mantle cloaking*. *Graphene* is the material adopted in this discussion in order to reach the cloaking of the object, so its properties are discussed, concentrating on the surface conductivity and surface impedance. The possibility to obtain the cloaking of the object, indeed, depends on the value of the surface impedance of the material that covers the cylinder, so it is worth computing that impedance for the *graphene*. It is found that the surface impedance of the *graphene* depends mostly on the value of the chemical potential and on frequency. This result is taken into account in the simulation part.

A planar version of the coated cylinder is simulated in order to see the amount of coupling among near cells and the amount of power that is lost from an extremity of a strip to the other one.

Then, the Radar Cross Section is defined as mean to measure cloaking effect. It is measured for all the simulated structures in order to understand whether the cloaking is reached and at which frequency this happens.

In the second part of the thesis, the simulated structures with the respective results are discussed.

Firstly, the bare cylinder is simulated and its RCS is adopted successively to compare the results of the coated cylinders to it. The cylinder is, then, covered by a substrate and by a certain number of vertical *graphene* strips (firstly with rectangular shape, then modulated with a sinusoidal profile). The parameters related to the strips shape, material and number and to the dielectric thickness are varied in order to reach the best cloaking performances in the considered frequency range.

For each simulated structure, the RCS and the electric field distribution in the plane normal to the cylinder are shown and discussed.

Finally, once the structure that allows to reach the best performances is found, new simulations are run just modifying the material of the inner cylinder, the plane wave settings or varying gradually the chemical potential among nearby strips.

Bibliography

- [1] A. Monti, J. Soric, R. Fleury, A. Alù, A. Toscano and F. Bilotti, “Mantle cloaking and related applications in antennas”, *Proc. IEEE Int. Conf. Electromagn. Adv. Appl. (ICEAA 2014)*, pp. 878-881, 2014.
- [2] A. Monti, J. Soric, M. Barbuto, D. Ramaccia, S. Vellucci, F. Trotta, A. Alù, A. Toscano, and F. Bilotti, “Mantle cloaking for co-siteradio-frequency antennas”, *Applied Physics Letters*, volume 108, issue 11, 2016.
- [3] W. Harris and R. Lamb, “How invisibility cloaks works”, <https://science.howstuffworks.com/invisibility-cloak8.htm>.
- [4] S. Chen, “China tests stealth "invisibility cloaks" on regular fighter jets”, *South China Mornign Post*, 2018.
- [5] K. Jahner, “Pentagon intrigued by breakthrough in cloaking technology”, *Army Times*, 2015.
- [6] P. Hanumantha Rao, I. Balakrishna and B. J. Sherlin, “Radiation Blockage Reduction in Antennas Using Radio-Frequency Cloaks”, *IEEE Antennas and Propagation Magazine*, pp. 91-100, 2018.
- [7] A. Forouzmand and A. B. Yakovlev, “Electromagnetic cloaking of a finite conducting wedge with a nanostructured graphene metasurface”, *IEEE Transactions on Antennas and Propagation*, vol.63, no.5, pp. 2191 - 2202, 2015.
- [8] P.-Y. Chen, C. Argyropoulos and A. Alù, “Broadening the Bandwidth of Metamaterial Cloaks with Non-Foster Metasurfaces”, *Phys. Rev. Lett.*,111, 233001, 2013 .
- [9] P. Alitalo and S. Tretyakov, “Electromagnetic cloaking with metamaterials”, *Materials today*, vol. 12, issue 3, pp.22-29, 2009.
- [10] D. R. Smith, “A cloaking coating for murky media”, *Science*, vol. 345, issue 6195, pp. 384-385, 2014.
- [11] M. Farhat, P.Y. Chen, H. Bagci, C. Amra, S. Guenneau, and A. Alù, “Thermal invisibility based on scattering cancellation and mantle cloaking”, *Nature*, Scientific Reports vol. 5, Article number 9876, 2015.
- [12] P.-Y. Chen, J. Soric, and A. Alù, “Invisibility and Cloaking Based on Scattering Cancellation”, *Advanced materials*, vol. 24, issue 44, pp. OP281-OP304, 2012.
- [13] J. M. Dawlaty, P. George, J. Strait, S. Shivaraman, M. Chandrashekhara, F. Rana, and M. G. Spencer, “Measurement of the Optical Properties of Graphene from THz to Near-IR”, *2008 Conference on Lasers and Electro-Optics and 2008 Conference on Quantum Electronics and Laser Science*, 2008.
- [14] A. Hassan and I. Khan, “Surface Plasmonic Properties in Graphene for the Variation of Chemical Potential”, *3rd International Conference on Informatics, Electronics and Vision 2014*, 2014.
- [15] P.-Y. Chen, J. Soric, Y. R. Padooru, H. M. Bernety, A. B. Yakovlev, and A. Alù, “Nanostructured graphene metasurface for tunable terahertz cloaking”, *New Journal of Physics*, vol. 15, 2013.

- [16] “Graphene synthesis, properties and applications”, <https://www.cheaptubes.com/graphene-synthesis-properties-and-applications>.
- [17] G. W. Hanson, “Dyadic Green’s Functions and Guided Surface Waves for a Surface Conductivity Model of Graphene”, *Journal of Applied Physics*, vol. 103, issue 6, 2008.
- [18] A. Vakil and N. Engheta, “Transformation Optics Using Graphene”, *Science*, Vol. 332, Issue 6035, pp. 1291-1294, 2011.
- [19] A. Tiberj, M. Rubio-Roy, M. Paillet, J. -R. Huntzinger, P. Landois, M. Mikolasek, S. Contreras, J. -L. Sauvajol, E. Dujardin and A. -A. Zahab ,“Reversible optical doping of Graphene”, *Scientific Reports*,2355 , 2013.
- [20] Microwave Studio, Computer simulation Technology, v.2018.
- [21] M. Wojtaszek, “Graphene: a two type charge carrier system”, *Rijksuniversiteit*, 2009.
- [22] F. Monticone, L. Matekovits, M. Orefice, K. P. Esselle, G. Vecchi, “Avoiding conductor width discontinuities at the cell borders in width-modulated microstrip line periodic structures”, *Proceedings of the International Conference on Electromagnetics in Advanced Applications (ICEAA10)*, (**Invited contribution to Special Session**), pp. 67-70, 20-24 Sept. 2010, Sydney, Australia.